

UNIVERSITY OF COPENHAGEN  
FACULTY OF SCIENCE

"



# PhD thesis

Michael. J. Larson

# A Search for Tau Neutrino Appearance with IceCube-De

Advisor: Dr. D. Jason Koskinen

Handed in: March 7, 2018

# Contents

## List of Figures

## List of Tables

# Introduction

Measurements of atmospheric neutrino oscillations, such as those performed in this thesis, require a background of understanding of both atmospheric neutrinos as well as neutrino oscillations. A history of neutrinos (Section ??) is used to explain the discovery of the three known flavors of neutrinos as well as the difficulties inherent in the study of these elusive particles. A discussion of the history of cosmic rays (Section ??) explains the source of both the neutrinos (Section ??) used as signal in this thesis as well as the muons, which form one of the primary backgrounds in the search for atmospheric oscillations. The detection of neutrinos is described in two parts. A discussion of the neutrino interactions (Section ??), explains the interactions of neutrinos with matter. The detection of these interactions through electromagnetic emission is then covered (Section ??).

## 1.1 The History of the Neutrino

In 1896, Henri Becquerel discovered radioactivity in uranium [1]. Measurements over the following decades showed various types of nuclear decays based on the penetration depth of the ionizing emissions. Measurements of one type of radioactivity, the beta decays, over the following 30 years showed that the production of two observed particles from one parent nucleus: a daughter nucleus and an outgoing electron. A single body decay of this type produces a known spectrum due to conservation of energy and momentum. The energy of the daughter nucleus and the electron are completely determined by these two conditions, leading to a narrow line emission spectrum.

Contrary to expectations, however, the measurement of energies of the two resulting particles showed wide, continuous spectra [2]. The spectrum provided a major puzzle for physicists due to the contradiction with the simple theoretical expectations. A conundrum for many years, one possible solution was suggested in 1930 by Wolfgang Pauli. In his letter, Pauli suggested that the conservation of energy and momentum could be saved if "... there could exist in the nuclei electrically neutral particles... which have spin 1/2 and obey the exclusion principle, and additionally different from light quanta in that they do not travel with the velocity of light" [3]. The solution to the beta decay puzzle was, then, that this additional "neutron" particle was emitted simultaneously with the observed daughter particles. This newly proposed particle would be electrically neutral and, therefore, unable to be seen through traditional methods. The resulting spectrum of the observed particles could then be continuous, as verified experimentally.

Pauli's suggestion provided a way to save the beloved conservation laws in physics, but at the expense of the assumption of a new particle. The particle, called the "neutron" in Pauli's letter and later renamed the "neutrino" by Fermi, was proposed to be electrically neutral and, therefore, completely undetectable at the time. Later work proposed that the neutrinos interact only via the weak nuclear force, with an interaction strength many orders of magnitude smaller than electromagnetic and strong nuclear forces. Experimental measurements, sensitive only to electromagnetic forces, therefore cannot be used to study neutrinos directly in the same way that other particles may be measured.

It was not until nearly 20 years later, in 1956, that this mystery particle was first detected [4]. In a groundbreaking work, Cowen and Reines presented an experiment at the Savannah River Plant, a nuclear power plant, demonstrating detection of the neutrino. The experiment, made up of layers of scintillation detectors around polyethelene boxes,

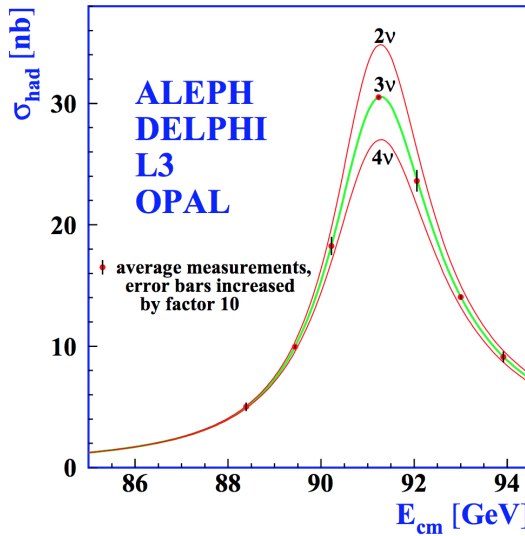


**Figure 1.1** – The number of active neutrinos as measured by ALEPH, DELPHI, L3, and OPAL. The data from the four experiments strongly favors only three neutrinos coupling to the Z boson. Image taken from [9].

yielded a signal-to-background rate of about 3 to 1 with a rate of  $2.88 \pm 0.22$  counts/hour with a total livetime of 1371 hours, including time during which the nearby nuclear reactor was offline. For the discovery of the first neutrinos, Frederick Reines was granted a shared Nobel Prize in Physics for the year 1995 [5].

Since the neutrino was first observed, additional measurements have discovered two new flavors of neutrinos: the muon neutrino [6] and the tau neutrino [7, 8].

Searches for additional neutrinos beyond the discovered three have been performed by investigating the decays of the Z boson. The Z boson, a particle of 91 GeV [pdg], couples both to the neutrinos and to more easily observed hadrons and charged leptons making it a useful probe of neutrino interactions. The width of the Z decay to hadrons, for instance, is affected by the number of active, light neutrino species [9]. Additional flavors of neutrinos coupling to the Z boson would lead to a smaller decay rate to hadrons observed in accelerator searches for hadrons as shown in Figure ???. The number of neutrinos may be calculated by comparing the best-fit ratio of "invisible" decays of the Z boson (ie, those involving two neutrinos) to the measured width expected from charged leptons in the standard model.

$$R_{inv} \equiv \frac{\Gamma_{inv}}{\Gamma_{ll}} = N_\nu \left( \frac{\Gamma_{\nu\nu}}{\Gamma_{ll}} \right)_{SM} \quad (1.1)$$

Here the number of neutrinos is extracted by assuming that all active neutrinos have the same coupling to the Z boson, result which has been verified experimentally. A precision measurement of the Z resonance completed at the LEP collider found the best fit value of  $N_\nu = 2.9840 \pm 0.0082$ , in good agreement with only three active neutrinos.

## 1.2 History of Cosmic Rays

In the early years of the 20th century, scientists began investigating previously-unknown ionizing radiation in the atmosphere. Scientists using electroscopes, early instruments designed to measure electric charge and radiation, discovered low levels of radiation

in the air. This new radiation was observed to be reduced when the electroscope was shielded by metal free of radioactivity, indicating that the signal was not an artifact of the detector itself and was, instead, coming from an external source.

Following just a few decades after the discovery of radioactivity by Becquerel, many scientists believed that the electroscope was picking up radiation from the Earth itself. The rate would be expected to decrease with increasing altitude above sea level and, to increase with increasing depth in the sea. Early measurements by Domenico Pacini in 1910 showed that the radiation rate decreased by 20% at a depth of 3 meters underwater compared to the rate at the surface [10], implying an origin independent of the Earth's crust. Measurements were performed with electroscopes by Victor Franz Hess in 1912 of the rate of ionizing radiation up to an altitude of 5 km [11].

Hess showed that the observed rate decreased until an altitude of around 1 km, but at a slower rate than expected from theory. Above 1400 meters, however, the rate of ionizing radiation increased again, rising substantially up to the maximum altitude reached at 5300 meters [12]. Hess's work, later confirmed by Henri Millikan, showed definitively that there exists a source of radiation of extraterrestrial origin, earning him the Nobel Prize in Physics for 1936 [13]. This radiation was later dubbed "cosmic rays" by Millikan in reference to their extraterrestrial origin.

Work on cosmic rays has lead to numerous discoveries. In 1937, the first *hadronic showers* were observed [14]. Hadronic showers of particles created by interactions of cosmic rays were shown to produce large numbers of particles [15, 11], with many producing from  $5 \times 10^6$  to over  $10^9$  particles [16]. These showers begin with a cosmic ray primary particle, often a single proton accelerated to high energies, which interacts with particles of the Earth's atmosphere. The interaction leads to the creation of various daughters, including neutrinos, muons, pions, kaons, and other hadrons.

Modern measurements have shown that the cosmic ray spectrum primarily consists of protons with a small contribution from helium and heavier elements [17]. These ions are accelerated in unknown astrophysical sources up to extremely high energies. The cosmic ray spectrum extends over many orders of magnitude, with the highest energy observations reaching  $10^{20}$  electronvolts - far higher than any Earth-based accelerator. The spectrum, shown in Figure ??, has multiple features that are believed to arise from different accelerator sources at different scales, each of which has been verified by multiple experiments.

## 1.3 Atmospheric Neutrinos

Air showers from cosmic rays provide a useful natural source of neutrinos in the GeV energy range and above that may be used for fundamental physics research. The hadronic shower produces pions and kaons which, in turn, decay to produce neutrinos

$$\pi^+ \rightarrow \mu^+ \nu_\mu \rightarrow e^+ \nu_e \bar{\nu}_\mu \nu_\mu \quad (1.2)$$

from the pions and from the kaons

$$K^+ \rightarrow \pi^+ \nu_\mu \rightarrow e^+ \nu_e \bar{\nu}_\mu \nu_\mu \nu_\mu \quad (1.3)$$

The neutrino flux depends on a number of parameters, including the Earth's magnetic field and temperature profile, the cosmic ray flux, and the details of hadronic interactions in air showers [18]. The calculation of the neutrino flux predictions requires significant, dedicated simulation work, producing fluxes as both a function of energy (Figure ??) and direction (Figure ??).

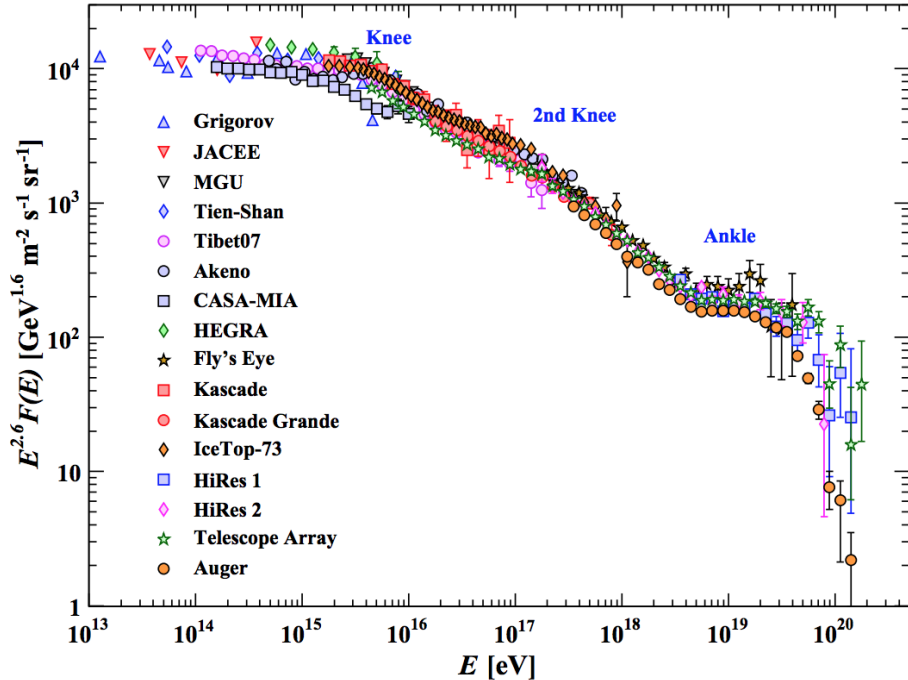


**Figure 1.2** – The cosmic ray spectrum covers many orders of magnitude and has been verified by many experiments to high precision. The various features are thought to be caused by multiple sources at different scales. Image taken from [17]

## 1.4 The Standard Model

Muons and neutrinos form just a small part of the Standard Model of particle physics. The Standard Model, with fundamental particle types and properties shown in Figure ??, consists of six quarks (up, down, strange, charm bottom, and top), three charged leptons (electron, muon, tau), three uncharged leptons (electron neutrino, muon neutrino, and tau neutrino), and the five bosons related to interactions (photon, Z, W, gluon, and Higgs). Combinations of the quarks lead to various hadrons, particles which interact with and are formed via the strong force, with different combinations of quarks and anti-quarks producing a wide variety of particles. The Standard Model, developed over the last half century, elegantly encapsulates the range of phenomena known to occur in particle physics and has been verified repeatedly over decades by many experiments. Predictions of the Standard Model have been carefully verified by accelerator experiments, yielding precise checks on a wide range of parameters.

The three charged leptons and neutrinos form three "families" or "flavors". Each charged lepton possesses a coupled neutrino which shares a lepton number conserved in interactions. The electron, the lightest of the charged leptons at 511 keV [17], is a key ingredient of the atoms that make up the world, forming the basis for all of chemistry and is the only stable charged lepton. The muon, with a mass of 105.7 MeV, is the middle of the three charged leptons, often appearing in particle interactions accompanied by the muon neutrino. The muon has a relatively long lifetime of 2.197 microseconds, far longer than many unstable hadrons. The tau lepton is the heaviest of the leptons, and with a mass of 1.777 GeV, it is heavier than the proton and appears only in relatively high energy interactions. The tau has an extremely short lifetime, at 290.6 femtoseconds, and a rich

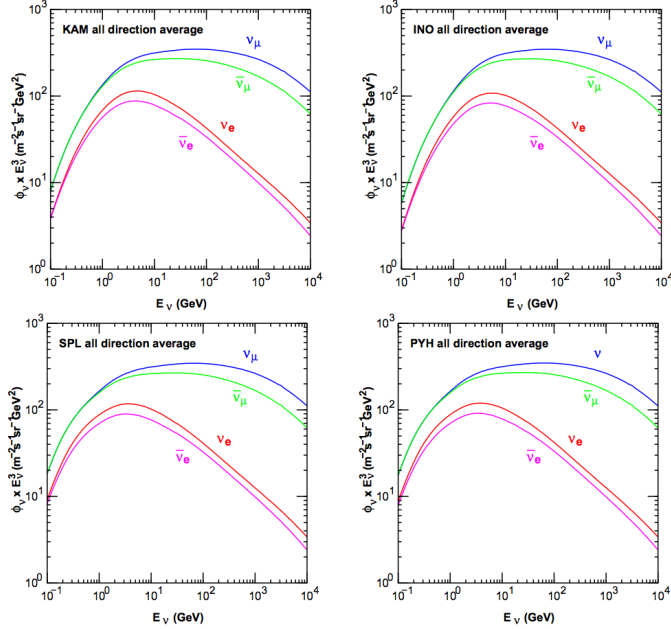


**Figure 1.3** – The expected neutrino flux at Kamioka mine, Japan (Super-Kamiokande, top left), Ino Peak, India (India-based Neutrino Observatory, top right), the South Pole (IceCube, bottom left), and Pyhasalmi mine, Finland (EMMA experiment, bottom right) as a function of energy. Note that the neutrino and anti-neutrino fluxes are characterized separately. The differences in the flux at each site is due to differences in the Earth’s magnetic field and temperature profile. Figure taken from [18].

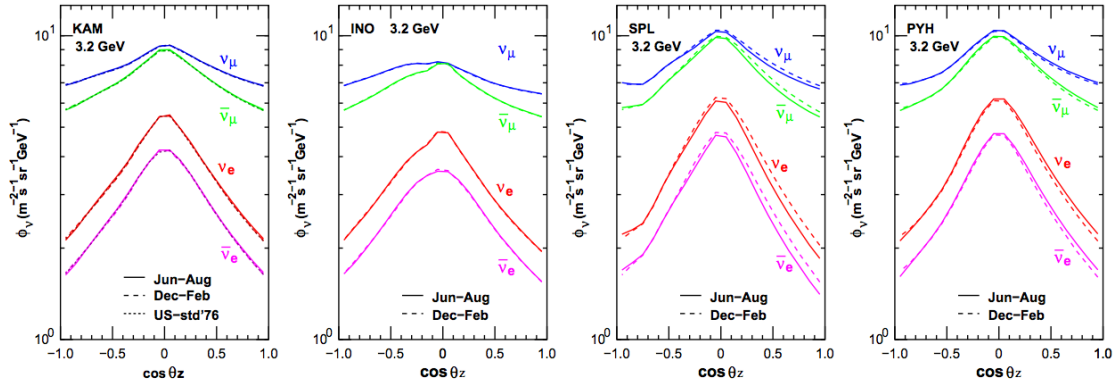


**Figure 1.4** – The expected flux of 3.2 GeV neutrinos at Kamioka mine, Japan; Ino Peak, India; the South Pole; and Pyhasalmi mine, Finland as a function of zenith angle. A value of  $\cos \theta_Z = -1$  indicates neutrinos passing through the entire Earth and entering the detector from below while a value of  $\cos \theta_Z = +1$  indicates neutrinos interacting in the atmosphere directly above the detector. The differences in the flux at each site is due to differences in the Earth’s magnetic field and temperature profile. Figure taken from [18].

variety of decay products. This extremely short lifetime and high mass make the tau difficult to produce and study.

For the purposes of this work, the most significant parts of the Standard model are the neutrinos, which will be defined to be signal events; the up and down quarks, which will make up the protons and neutrons upon which the neutrinos will interact; the W and Z

## Standard Model of Elementary Particles

three generations of matter (fermions)					
	I	II	III		
mass	$\approx 2.4 \text{ MeV}/c^2$	$\approx 1.275 \text{ GeV}/c^2$	$\approx 172.44 \text{ GeV}/c^2$	0	$\approx 125.09 \text{ GeV}/c^2$
charge	2/3	2/3	2/3	0	0
spin	1/2	1/2	1/2	1	0
QUARKS	u up	c charm	t top	g gluon	Higgs
	$\approx 4.8 \text{ MeV}/c^2$	$\approx 95 \text{ MeV}/c^2$	$\approx 4.18 \text{ GeV}/c^2$	0	$\approx 125.09 \text{ GeV}/c^2$
	-1/3	-1/3	-1/3	0	0
	1/2	1/2	1/2	1	0
	d down	s strange	b bottom	$\gamma$ photon	
LEPTONS	e electron	$\mu$ muon	$\tau$ tau	Z Z boson	
	$\approx 0.511 \text{ MeV}/c^2$	$\approx 105.67 \text{ MeV}/c^2$	$\approx 1.7768 \text{ GeV}/c^2$	0	
	-1	-1	-1	1	
	1/2	1/2	1/2	1	
	$\nu_e$ electron neutrino	$\nu_\mu$ muon neutrino	$\nu_\tau$ tau neutrino	W W boson	
	<2.2 eV/c <sup>2</sup>	<1.7 MeV/c <sup>2</sup>	<15.5 MeV/c <sup>2</sup>	$\pm 1$	$\approx 80.39 \text{ GeV}/c^2$
	0	0	0	1	
	1/2	1/2	1/2	1	
GAUGE BOSONS					

**Figure 1.5** – The Standard Model of particle physics is made up of charged and uncharged leptons, quarks, and the various bosons. Image taken from [19]

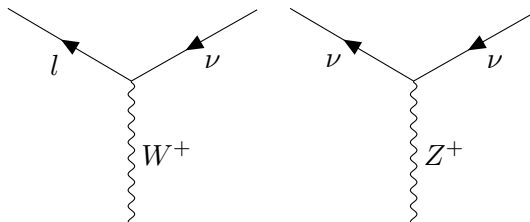


**Figure 1.6** – Feynman diagrams showing the interaction vertex of the neutrino with the W and Z boson.

bosons, which mediate the weak interactions via which the neutrinos may be observed; and the photon, which gives a method of observation of the interactions.

### 1.4.1 Neutrino Interactions

In the Standard Model, neutrinos are assumed to be massless, left-handed spin-1/2 leptons which interact solely via the weak force. Neutrinos, therefore, are only visible via indirect effects, such as scattering or production of charged particles that may, in turn, give off their own visible signature. An understanding of the methods by which neutrinos are detected therefore forms an important basis for the study of these elusive particles. Two basic Feynman diagrams, shown in Figure ??, may be used to represent the interaction vertices available for neutrinos.

These two vertices describe the interactions relevant for the work presented in this thesis. During so-called *charged-current (CC)* interactions, a  $W^\pm$  boson is exchanged between a neutrino and target particle, in the process converting the uncharged neutrino to the corresponding charged lepton. The *neutral-current (NC)* interactions are those in which

the uncharged Z boson is exchanged with the target and the neutrino, although losing a fraction of the initial energy, does not get converted to a charged lepton.

Detectors used to study particle properties rely on electromagnetic interactions and photons in order to detect particles. Because the neutrino itself does not interact via the electromagnetic force, charged leptons and hadrons must be used to indirectly study the properties of the incident neutrinos. Outgoing charged leptons in charged-current interactions may be detected, although the direction will not necessarily correspond to that of the incident neutrino. The average angle between the incident neutrino and outgoing lepton may be approximated following Equation ??.

$$\bar{\theta}_{\nu l} \approx \frac{1.5^\circ}{\sqrt{E_\nu [\text{TeV}]}} \quad (1.4)$$

There exist three further classifications of neutral-current and charged-current neutrino interactions in the energy range used in this work: the quasi-elastic, resonant, and deep inelastic interactions [20]. A fourth type, coherent neutrino scattering, may also occur, although the energies involved are too low to impact this work. The three types of interactions contribute to the total cross-section with peaks at different energies, as shown in Figure ??.

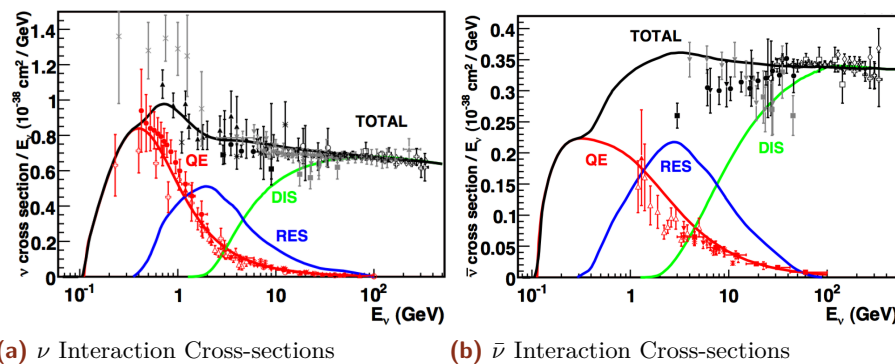


**Figure 1.7** – The relative contributions to the cross section for  $\nu$  (left) and  $\bar{\nu}$  (right). The QE events dominate below 1 GeV while the DIS events dominate above 10 GeV. Note the different scales for the neutrino and antineutrinos. Images taken from [20]

## Quasi-Elastic and Resonant Interactions

At low energies of approximately 100 MeV to around 2 GeV, the neutrinos interact via *quasi-elastic scattering (QE)* interactions. In the QE interaction, the neutrino scatters off an entire nucleon instead of the individual quarks. In a charged current QE neutrino (anti-neutrino) interaction, the target neutron (proton) is converted to a proton (neutron) while the neutrino is converted to a charged lepton.

The cross section for QE interactions depends on various nuclear form factors that must be fit to experimental data. Many of these form factors may be fit to electron scattering data, leaving only the axial vector nuclear form factors to be measured in the neutrino sector [20]. This form factor is normally assumed to have the dipole form

$$F_A(Q^2) = \frac{g_A}{\left(1 + \frac{Q^2}{M_A^2}\right)^2} \quad (1.5)$$

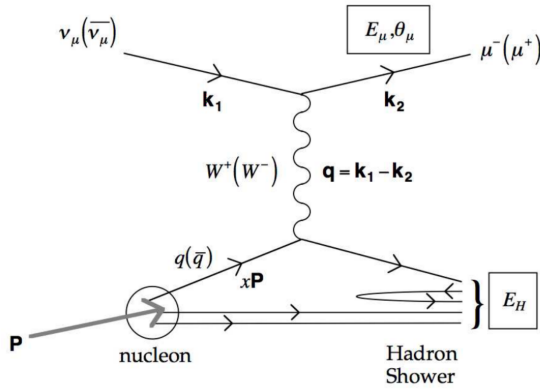


**Figure 1.8** – A Feynman diagram showing an example of a CC neutrino DIS interaction. An incident muon neutrino interacts with a quark inside of a proton. The result is a hadronic shower as well as a charged muon. Diagram taken from [formaggio-xsec]

where  $g_A$  is a constant fit to experimental data,  $Q^2$  is the 4-momentum transferred in the interaction, and  $M_A$  is the "axial mass". This last term is fit to experimental data with a value of  $M_A = 0.999 \pm 0.011$  GeV [20].

*Resonant scattering* interactions (*RES*), which result in the excitation of a nucleon followed by decay via emission of (typically) pions, occur for neutrinos of slightly higher energies of around 500 MeV to 10 GeV. Resonant interactions are modeled in a similar way as the quasi-elastic interactions, with an associated axial mass term used to describe nuclear uncertainties.

### Deep Inelastic Interactions

Above a few GeV, the neutrino cross section rises approximatley linearly with energy and is dominated by *deep inelastic scattering (DIS)* interactions. An example of a DIS interaction is shown in Figure ???. In DIS events, the exchange of the Z or W boson probes the internal structure of the nucleons, leading to a scattering off of the individual quarks of the nucleus. This results in disruption of the nucleon and the larger nucleus and a collection of daughter particles forming a *hadronic shower*.

As seen in Figure ???, the DIS events dominate the neutrino cross section above 10 GeV and form the only significant interaction above 100 GeV [formaggion-xsec]. Experiments with high statistics samples of DIS events have been used to measure the charged current cross section to the few-percent level.

## 1.5 Methods of Detection

Neutrinos may be detected through the QE, RES, and DIS interaction channels, with each possessing a distinct signature. The interaction of neutrinos at the GeV energy ranges relevant for this thesis lead to the emission of hadrons in a hadronic shower. The lower energy QE and RES interactions typically yield only one pion which may decay into a pair of photons ( $\pi^0$ ) or into further charged hadrons and leptons ( $\pi^\pm$ ). DIS interactions produce larger hadronic showers containing many charged particles that may be detected. In addition to the hadronic shower, charged-current interactions result in an outgoing charged lepton, the result of which depends on the flavor of the incident neutrino. Outgoing electrons quickly scatter in interactions with the surrounding media, ionizing atoms and producing a secondary *electromagnetic shower* of particles. Muons, on the

Decay	Branching Ratio	Background
$\tau \rightarrow e^- \nu_e \nu_\tau$	$17.83 \pm 0.04 \%$	$\nu_e$ CC
$\tau \rightarrow \mu^- \nu_\mu \nu_\tau$	$17.41 \pm 0.04 \%$	$\nu_\mu$ CC
$\tau \rightarrow \text{hadrons}$	Otherwise	$\nu$ NC

**Table 1.1** – The branching ratios for the decay of tau leptons. Two-thirds of the time, the tau lepton decays hadronically.

other hand, travel longer distances before scattering or decaying in the medium, leading to an extended track.

The signature of a tau neutrino charged current interaction varies depending on the specific decay channel of those presented in ???. Because the tau lepton has a very short lifetime, outgoing taus tend to decay immediately, producing daughter particles. Each of the three decay modes mimic interactions of the electron and muon neutrinos. The secondary electromagnetic or hadronic cascade is theoretically distinguishable from the primary hadronic cascade produced by a tau neutrino charged current interaction, although the distance traveled by the tau lepton at the energies relevant for this work is on the order of millimeters, far below the reconstruction precision possible with the IceCube detector.

In each case, the charged particles deposit energy into the interaction medium during travel through a series of stochastic and continuous emissions. It is through the detection of these stochastic and continuous losses that daughter particles may be identified in the study of neutrinos.

### 1.5.1 Stochastic Emission Mechanisms

A total of five major stochastic emission mechanisms are important for the energy losses in neutrino experiments [21]. One such mechanism is the decay of the particle, a process which splits the energy of the parent into multiple, lower energy daughters. Decays of daughter leptons can often be important in the identification of the neutrino flavor, particularly for tau neutrino candidates occurring above 10 TeV when the primary and secondary hadronic interactions become well-separated.

Ionization losses occur when the charged lepton interacts with electrons in the medium, transferring enough energy to liberate the electrons from bound states. At energies below 1 TeV, these losses are the most significant form of energy loss for charged particles, producing a significant source of additional electrons. Ionization losses occur roughly independently of the energy of the charged lepton.

Above energies of a few hundred GeV, radiative processes dominate the energy losses for muons in matter [17]. Bremsstrahlung, photon emission from charged particles accelerating in a magnetic field, pair production, in which a particle and antiparticle (typically electron and positron) are created, and hadronic interactions of photons all dominate the energy losses of muons above 1 TeV.

There exists a minimum in the energy loss rates. Particles emitting near this minimum rate are known as *minimum-ionizing* particles [17].

Stochastic emissions result in additional particles in the detector, leading to improved light yield. In addition, some detectors use photosensitive emulsions [22, 7], scintillators [23, 24, 25, 26], or time projection chambers [27] in order to track ionization losses. These emulsions yield precise characterization of particle decays, allowing experimentalists to uniquely determine the flavor state of the interacting neutrino.

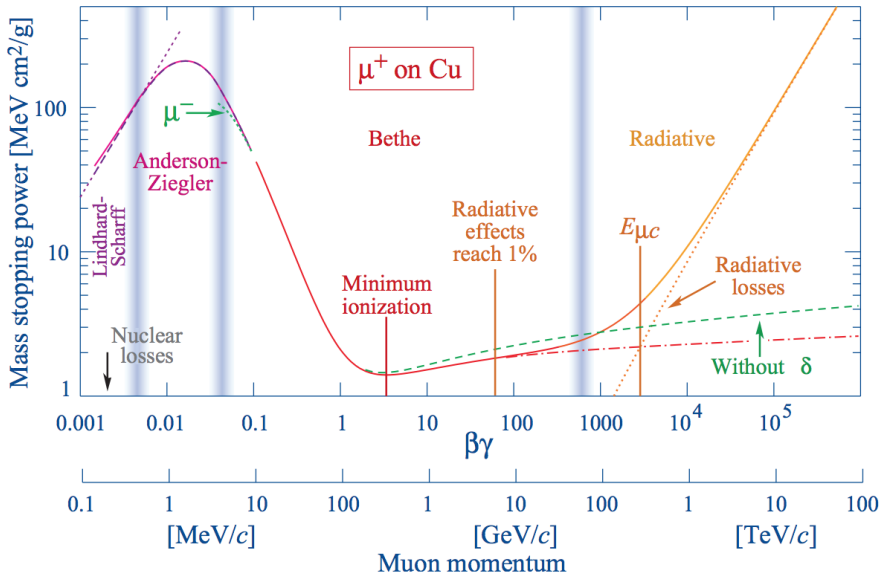


**Figure 1.9** – An example of the energy loss ( $-\frac{dE}{dx}$ ) calculated for muons incident on copper. Note the radiative losses due to bremsstrahlung, pair production, and photonuclear interactions above 1 TeV. Note also the labeled minimum demonstrating the energy of a minimum ionizing particle. Image taken from [17].

### 1.5.2 Cherenkov Emission

When a charged particle passes through a dielectric medium with a speed larger than the local phase velocity of light, it will emit *Cherenkov radiation*[28]. The effect, first reported by Pavel Cherenkov in 1934 [29] remained unexplained theoretically until work done by Ilya Frank and Igor Tamm in 1937 [30].

For a dielectric medium, the electric field of the charged particle will polarize atoms by inducing a small dipole moment due to electromagnetic effects in nuclei of atoms in the medium [31]. The resulting disturbance of the medium propagates with the phase velocity of light, given by the speed of light,  $c$ , and the index of refraction as a function of the frequency of light,  $n(\omega)$ . If the charged particle is traveling faster than the local phase velocity, the electromagnetic disturbance propagates with constructive interference, resulting in a planar wavefront of emission known as *Cherenkov emission*. The angle of the wavefront relative to the propagation direction is given by the ratio of the distance traveled by the particle and photons in a given time.

$$\cos(\theta_C) = \frac{\frac{c}{n(\omega)}t}{vt} = \frac{c}{n(\omega)v}, \quad (1.6)$$

The energy threshold for Cherenkov emission is set by a combination of the particle mass and the local phase velocity for light,  $\frac{c}{n}$ . Using the relativistic kinetic energy [32],

$$E_C \geq \frac{mc^2}{\sqrt{1 - \left(\frac{c/n}{c}\right)^2}} \quad (1.7)$$

$$E_C \geq mc^2 \sqrt{\frac{n^2}{n^2 - 1}} \quad (1.8)$$

For ice with a index of fraction of 1.32 at 400 nanometers [33], this works out to a minimum energy of 270 keV for electrons and 56.2 MeV for muons. The number of photons emitted increases with energy, with approximately 50% more photos produced in blue visible light than in red[32] The full emission spectrum, first worked out by Ilya Frank and Igor Tamm in 1937 [30], depends on a number of parameters, including the energy and charge of the emitting particle as well as the properties of the medium. In the case of a particle traveling a distance  $L$  much larger than the photon frequency of interest,  $\lambda$ , the number of emitted photons may be approximated by

$$\frac{dN}{d\lambda} = \frac{2\pi\alpha}{\lambda^2} L \sin^2 \theta_C \quad L \gg \lambda \quad (1.9)$$

Cherenkov emission is not limited to a single charged lepton. All charged particles emit Cherenkov radiation, including any hadrons and charged daughter particles, resulting in measurable signals. While the total amount of energy lost via Cherenkov emission is small relative to losses due to stochastic processes, this emission type is both continuous and results directly in photons which may be observed by photodetectors. This technique is used by multiple experiments, including SNO [34], Super-Kamiokande [35], ANTARES [36], and IceCube [37].

# Neutrino Oscillations

The search for oscillation events requires an explanation of neutrino oscillations. The theory of neutrino oscillations is included here with broad descriptions of oscillations in vacuum (Section ??) and in matter (Section ??). Experimental evidence for the neutrino oscillations and current constraints on the oscillation parameters is presented in Section ?? . Finally, a description of unitarity in the PMNS mixing matrix is given in Section ?? with particular emphasis placed on the search for additional neutrino flavors (Section ??). The motivation for this thesis as well as the purpose behind joint fits between appearance and disappearance data is discussed in Section ??.

## 2.1 Oscillation Theory and the PMNS Matrix

In 1968, Bruno Pontecorvo suggested a process, known as *neutrino oscillation*, by which neutrinos could change flavors [38]. The theory of neutrino oscillations was further developed for the neutrino sector by Ziro Maki, Masami Nakagawa and Shoichi Sakata in 1962 [39].

### 2.1.1 The PMNS Mixing Matrix

We now understand there to be three distinct flavors of neutrinos. Neutrinos are created via the weak force as pure flavor eigenstates. These states are coherent superpositions of mass eigenstates. Specifically, there exist three weak eigenstates of the left-handed neutrino fields that are related to three known neutrino mass eigenstates via the Pontecorvo-Maki-Nakagawa-Sakata (*PMNS*) lepton mixing matrix.

$$\begin{pmatrix} \nu_e \\ \nu_\mu \\ \nu_\tau \end{pmatrix} = U_{PMNS} \begin{pmatrix} \nu_e \\ \nu_\mu \\ \nu_\tau \end{pmatrix} = \begin{pmatrix} U_{e1} & U_{e2} & U_{e3} \\ U_{\mu 1} & U_{\mu 2} & U_{\mu 3} \\ U_{\tau 1} & U_{\tau 2} & U_{\tau 3} \end{pmatrix} \begin{pmatrix} \nu_1 \\ \nu_2 \\ \nu_3 \end{pmatrix} \quad (2.1)$$

The flavor eigenstates  $(\nu_e, \nu_\mu, \nu_\tau)$  describe the fields of the left-handed neutrinos coupling via the weak charge to the electron, muon, and tau respectively. The three mass states  $(\nu_1, \nu_2, \nu_3)$  represent the mass eigenstates. The mixing between the two types of states is given by the unitary matrix,  $U_{PMNS}$ . The mixing may be written in a shortened form

$$\nu_\alpha(x) = \sum_i U_{\alpha i} \nu_i(x) \quad (2.2)$$

where  $\alpha = e, \mu, \tau$  and  $i = 1, 2, 3$ .

Neutrinos interact via the weak force and are created in flavor states  $e, \mu, \tau$ . The neutrino produced in flavor state  $\nu_\alpha$  exists in a superposition of the three mass eigenstates.

where  $\delta_{ij}$  and  $\delta_{\alpha\beta}$  are Kronecker delta functions. As a  $3 \times 3$  unitary matrix, the PMNS matrix may be parametrized in terms of three mixing angles and six phases. Of these phases, five may be removed by rephasing the lepton fields with no change to the underlying physics, leaving one physical phase related to CP violation.

The PMNS may be written in terms of the product of three smaller unitary matrices using these mixing angles.

$$U_{PMNS} = \begin{pmatrix} 1 & 0 & 0 \\ 0 & c_{23} & s_{23} \\ 0 & -s_{23} & c_{23} \end{pmatrix} \begin{pmatrix} c_{13} & 0 & s_{13}e^{-i\delta_{CP}} \\ 0 & 1 & 0 \\ -s_{13}e^{i\delta_{CP}} & 0 & c_{13} \end{pmatrix} \begin{pmatrix} c_{12} & s_{12} & 0 \\ -s_{12} & c_{12} & 0 \\ 0 & 0 & 1 \end{pmatrix} \quad (2.3)$$

where the notation  $c_{ij}$  idenotes  $\cos(\theta_{ij})$  and  $s_{ij}$  denotes for  $\sin(\theta_{ij})$ .

Note that if neutrinos are Majorana fermions, the additional phases may not be removed without making the masses complex. The Majorana terms form additional diagonal terms in Equation ???. While Majorana mass terms are beyond the scope of this work, further information may be found in [40, 41].

The three submatrices of Equation ?? have historically been studied by different types of experiments. This history has lead to the proliferation of alternative names for the matrices and of the mixing angles.

$$U_{PMNS} = U_{Atmospheric} U_{Reactor} U_{Solar} \quad (2.4)$$

This leads to the alternative names of the mixing angles, with  $\theta_{23}$ ,  $\theta_{13}$ , and  $\theta_{12}$  being referred to as the atmospheric mixing angle, the reactor mixing angle, and the solar mixing angle respectively.

## 2.1.2 Neutrino Mixing in Vacuum

Propagation of neutrinos requires the use of the Hamiltonian. However, the flavor states are not eigenstates of the Hamiltonian. For propagation of the neutrino, the mass eigenstates must instead be used.

$$|\nu(t=0)\rangle = |\nu_\alpha\rangle = \sum_i U_{\alpha i}^* |\nu_i\rangle \quad (2.5)$$

The propagation leads to a neutrino state at time  $t \neq 0$  which is no longer a pure flavor state.

$$|\nu(t)\rangle = \sum_i U_{\alpha i}^* e^{-iE_i t} |\nu_i\rangle \quad (2.6)$$

where  $E_i = \sqrt{p^2 + m_i^2}$  is the total energy of the  $i$ th mass eigenstate. If the neutrino state interacts, the flavor eigenstate must again be used to calculate the probabilities of interacting as each of the three known flavors.

$$P(\nu_\alpha \rightarrow \nu_\beta) = |\langle \nu_\beta | \nu(t) \rangle|^2 = \left| \sum_i U_{\beta i} U_{\alpha i}^* e^{-iE_i t} \right|^2 \quad (2.7)$$

Proper calculations from this point can be performed by treating each neutrino as a quantum mechanical wave packet [42]. This allows for the full description of neutrino oscillation in the context of decoherence of the mass states during propagation, allowing each mass state to possess separate momenta.

In practice, the description of neutrino oscillations necessary for this work is adequately described by making a few simplifying assumptions. In particular, this work assumes that all mass eigenstates propagate as plane waves possessing identical, well-defined momenta [40]. Neutrinos are further assumed to be extremely relativistic at the energies of interest, an assumption well-justified by cosmological fits to the sum of the three

neutrino masses, which give an upper limit of around 0.2 eV [17]. The total neutrino energy is also assumed to be unchanged during propagation. The resulting calculation of the oscillation probabilities is identical in both the simplified version and the full derivation.

To begin, equation ?? is expanded by explicitly including the complex conjugate,

$$P(\nu_\alpha \rightarrow \nu_\beta) = \sum_i^3 U_{\beta i}^* U_{\alpha i} \sum_j U_{\beta j} U_{\alpha j}^* e^{i(E_i - E_j)t} \quad \alpha, \beta = e, \mu, \tau. \quad (2.8)$$

In the highly relativistic limit,  $E \gg m_i$ , and  $t \approx L$  where  $L$  is the distance traveled during propagation. Using these two approximations, the exponential term in Equation ?? may be rewritten using Euler's formula

$$e^{i(E_i - E_j)t} = 1 - 2 \sin^2 \left( \frac{m_{ij}^2 L}{4E} \right) + i \sin \left( \frac{m_{ji}^2 L}{2E} \right) \quad (2.9)$$

Note that a new shorthand has been defined,  $\Delta m_{ji}^2 = m_j^2 - m_i^2$ , giving a fundamental parameter of neutrino oscillations. The PMNS terms of equation ?? may be expanded further, yielding

$$\left| \sum_j U_{\beta j} U_{\alpha j}^* \right|^2 = \delta_{\alpha\beta} + 2 \sum_{i < j} \sum_i U_{\beta i}^* U_{\alpha i} U_{\beta j} U_{\alpha j}^* \quad (2.10)$$

where the factor of two arises due to the symmetry  $i \leftrightarrow j$ . Putting the terms together, the final oscillation probability formula is

$$P(\nu_\alpha \rightarrow \nu_\beta) = \delta_{\alpha\beta} - 4 \sum_{i < j} \operatorname{Re} \left[ \sum_i U_{\beta i}^* U_{\alpha i} U_{\beta j} U_{\alpha j}^* \right] \sin^2 \left( \frac{m_{ij}^2 L}{4E} \right) \\ + 2 \sum_{i < j} \operatorname{Im} \left[ \sum_i U_{\beta i}^* U_{\alpha i} U_{\beta j} U_{\alpha j}^* \right] \sin \left( \frac{m_{ji}^2 L}{2E} \right). \quad (2.11)$$

This calculation has been derived for neutrinos. To calculate the probabilities for anti-neutrinos, the calculation changes by replacing  $U \rightarrow U^*$ , resulting in a change in sign of the last term of Equation ??.

From Equation ??, the general form of the oscillation probabilities becomes clear. The PMNS matrix elements yield the amplitude of oscillations, while the phase of the oscillations is related to three quantities: the squared difference in the masses,  $\Delta m_{ji}^2$ ; the baseline, or distance traveled,  $L$ ; and the energy of the neutrinos. Only one of these three is a fundamental physics parameter. The choices of energy sensitivity and baseline are used to define characteristics of detectors used for measurements of the various mass splitting parameters and oscillation mixing angles.

Note that the oscillation probability is insensitive to the sign of the mass splitting parameter.

### 2.1.3 Matter Effects in Oscillation

Calculations up to this point have assumed neutrinos oscillating in vacuum. Modifications required for a description of matter effects begin with a modification of the Hamiltonian

with a potential,  $V$ , due to coherent forward scattering of neutrino on electrons and nucleons in the medium [43].

$$H = H_0 + V \quad (2.12)$$

The value of  $H_0$  is the value of vacuum Hamiltonian. In the two-flavor case, the Hamiltonian can be shown [40, 44] to be

$$H_0 = \frac{\Delta m^2}{4E} \begin{pmatrix} -2\cos 2\theta & \sin 2\theta \\ \sin 2\theta & 0 \end{pmatrix}. \quad (2.13)$$

where  $\theta$  is the mixing angle associated with the 2x2 PMNS matrix. If this effect leaves the neutrino momentum unchanged, the resulting additional terms in the Hamiltonian may interfere with the propagation of the unscattered neutrinos. The potential includes contributions from both charged current and neutral current interactions, although the charged current interactions arise solely from the electron neutrinos. The potential, expressed in the flavor basis, is then

$$V_{CC,\alpha} = \begin{cases} \sqrt{2} \pm G_F n_e(x) & \alpha = e \\ 0 & \alpha = \mu, \tau \end{cases} \quad V_{NC,\alpha} = -\frac{G_F}{\sqrt{2}} n_e(x) \quad \alpha = e, \mu, \tau \quad (2.14)$$

where a + is used for neutrinos and a - is used for antineutrinos,  $n_e$  is the density of electrons in the medium, and  $G_F$  is the Fermi coupling constant. Note that the angle included here is that of the PMNS matrix in two dimensions. A full description of three flavor neutrino oscillation in the presence of a matter potential is beyond the scope of this work. Further information and explicit forms may be found in [40, 44]. The full three-flavor oscillation calculation is used for this thesis using the Prob3++ code [45, 46], which includes an implementation of matter effects. The electron densities are calculated from the Preliminary Reference Earth Model (PREM) [47].

## 2.2 Experimental Constraints on Neutrino Oscillations

### 2.3 Solar Neutrinos: A Hint of Multiple Flavors

Early searches for neutrinos focused primarily on the Sun. The first major experiment, proposed by Ray Davis and John Bahcall, was designed to verify that fusion was the primary energy source of the Sun [48, 49]. While the core of the sun is not directly visible to telescopes, neutrinos produced via nuclear fusion could escape the sun relatively unchanged and be observed at Earth.

The Homestake experiment, named for Homestake mine in South Dakota, used 615 tons of perchloroethylene to measure neutrinos via the inverse beta decay reaction



The production rate was well-measured, with a rate of 0.48 counts per day and a background of 0.09 counts per day due to interactions from cosmic ray induced muons [50]. In the typical units of the solar neutrino experiments, this worked out to

$$(\sigma\phi) = 2.56 \pm 0.16 \pm 0.16 \text{ SNU} \quad (2.16)$$

where  $1 \text{ SNU} = 10^{-36}$  captures/nucleus/second. The expected rate of neutrino interactions from the sun, however, was predicted to be  $8.00 \pm 0.97$  SNU given the solar models at the time. The Homestake experiment, therefore, was only observing approximately 30% of the predicted interaction rate. New measurements from other experiments, such as SAGE [51], GALLEX [52], and GNO [53] confirmed the results, although with a reduction of around 50% instead of 70% compared to theoretical expectations.

The disagreement between the number of neutrinos expected and the number predicted was not definitively solved until the Sudbury Neutrino Observatory (SNO) experiment. SNO was a detector located 2 km underground in Sudbury mine in Canada [34]. The detector consisted of a large tank filled with heavy water surrounded by photo-multiplier tubes for the detection of Cherenkov emission. By introducing heavy water, SNO was sensitive to not only the charged current interactions of previous experiments, but also to neutral current interactions invisible to the inverse beta decay experiments.

SNO detected the neutral current and charged current interactions via two distinct channels. The charged-current interactions caused a deuterium atom to break down into two separate protons while also transforming the neutrino into an electron. The electron would be produced with an energy high enough to emit Cherenkov radiation and could, therefore, be observed directly, with the energy of the electron used to constrain the incident neutrino spectrum. The primary charged current interaction at SNO was only sensitive to electron flavor neutrino interactions.

The neutral current interactions, with a threshold energy of 2.22 MeV, were able to separate the deuterium in the heavy water, leading to a free neutron in the detector. The detection of the free neutron posed initial challenges for the same fundamental reason that neutrino detection is difficult: neutrons are not charged and therefore do not emit electromagnetic radiation. Instead, early detections of these neutrons relied on the emission of a high energy gamma ray when the neutron was captured on a deuterium atom. The gamma ray could then, in turn, be absorbed on an electron, accelerating the charged particle and producing Cherenkov radiation.

Measurements at SNO were divided between these two measurement channels in order to investigate one possible solution to the missing solar neutrinos: neutrino oscillations [54]. Because the three known neutrino states all have the same neutral current interaction cross section, the neutral current rate is expected to be constant in the presence of oscillations. The charged current rate is, however, expected to change due to the different couplings of each neutrino flavor to the  $W^\pm$  boson. Measuring both the neutral current and charged current rates therefore provided a direct test of neutrino oscillations, allowing researchers to identify the effect independent of the solar model.

SNO expected a rate of neutral current interactions from solar neutrinos of  $5.05 \times 10^6 \text{ cm}^{-2} \text{ s}^{-1}$  and observed

$$\phi_{NC}(\nu \text{ active}) = 5.25 \pm 0.16(\text{stat})^{+0.11}_{-0.13} \times 10^6 \text{ cm}^{-2} \text{ s}^{-1} \quad (2.17)$$

a result consistent with expectations. The charged current interaction was measured to be

$$\phi_{CC}(\nu_e) = (0.301 \pm 0.033) \phi_{NC}(\nu \text{ active}) \quad (2.18)$$

clearly indicating that the number of electron neutrinos was well below expectations. The combination of these two results gave the first clear indication of neutrino oscillations, a result which earned the SNO collaboration a Nobel Prize in 2015 [55].

## 2.4 Super-Kamiokande and Atmospheric Neutrinos

While the SNO experiment was working to identify the source of the solar neutrino deficit, the Kamioka Nucleon Decay Experiment (KamiokaNDE) and its successor, Super-Kamiokande (Super-K), were using a similar water Cherenkov detector to search for proton decay. The primary background for this rare process is neutrino interactions. Unlike SNO, however, Super-Kamiokande was sensitive to both MeV solar neutrinos and higher energy GeV neutrinos produced in the atmospheric showers from cosmic ray interactions.

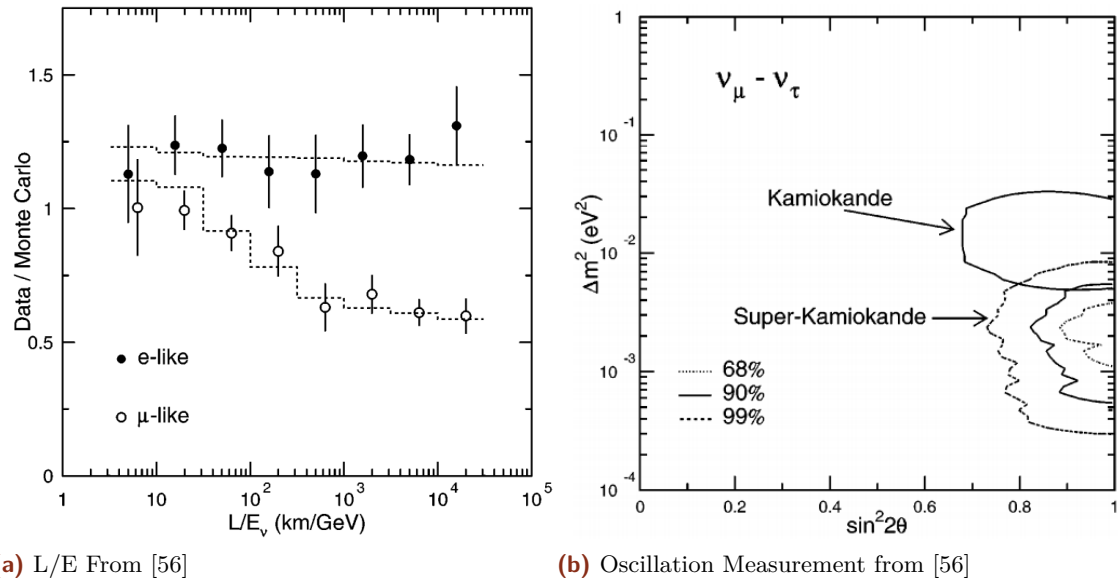


**Figure 2.1** – The first atmospheric neutrino oscillation measurements from the Super-K experiment. (a) The  $\nu_e$ -like events show no shape in L/E, as expected from a lack of neutrino oscillations. The  $\nu_\mu$ -like interactions, however, show a clear drop, indicating the presence of oscillation effects. (b) Using the two neutrino approximation, Super-K produced contours of the best-fit oscillation parameters for  $\nu_\mu \rightarrow \nu_\tau$  oscillations. Both figures from [56]

While investigating backgrounds, Super-Kamiokande observed an interesting deficit in the atmospheric neutrino signal. Unlike the case in the solar neutrinos, the deficit observed by Super-K was observed solely in the muon neutrino events with no effect seen in the electron neutrinos [56]. Using the reconstructed energy and direction of events, Super-K was able to show that the number of fully contained events of  $\nu_\mu$ -like interactions changed as a function of L/E - a clear signature of neutrino oscillations in the atmospheric neutrinos. The figure, reproduced in Figure ??, was used, in part, with a 2x2 approximation to the PMNS matrix to produce the first measurements, shown in Figure ??, of the atmospheric oscillation parameters. For the discovery of atmospheric neutrino oscillations at the same time as SNO's discovery of solar neutrino oscillations, the Super-K collaboration was jointly awarded the 2015 Nobel Prize [55].

### 2.4.1 Global Fits to Oscillations

Since the initial discoveries of SNO and Super-K, many experiments have measured neutrino oscillations. Global fits are performed and updated regularly [57, 58].

The most recent results are shown in Figure ?? and include information from solar, reactor, and atmospheric oscillation experiments. The results explicitly assume unitarity and three neutrino species.

	NuFIT 3.2 (2018)			
	Normal Ordering (best fit)		Inverted Ordering ( $\Delta\chi^2 = 4.14$ )	Any Ordering
	bfp $\pm 1\sigma$	$3\sigma$ range	bfp $\pm 1\sigma$	$3\sigma$ range
$\sin^2 \theta_{12}$	$0.307^{+0.013}_{-0.012}$	$0.272 \rightarrow 0.346$	$0.307^{+0.013}_{-0.012}$	$0.272 \rightarrow 0.346$
$\theta_{12}/^\circ$	$33.62^{+0.78}_{-0.76}$	$31.42 \rightarrow 36.05$	$33.62^{+0.78}_{-0.76}$	$31.43 \rightarrow 36.06$
$\sin^2 \theta_{23}$	$0.538^{+0.033}_{-0.069}$	$0.418 \rightarrow 0.613$	$0.554^{+0.023}_{-0.033}$	$0.435 \rightarrow 0.616$
$\theta_{23}/^\circ$	$47.2^{+1.9}_{-3.9}$	$40.3 \rightarrow 51.5$	$48.1^{+1.4}_{-1.9}$	$41.3 \rightarrow 51.7$
$\sin^2 \theta_{13}$	$0.02206^{+0.00075}_{-0.00075}$	$0.01981 \rightarrow 0.02436$	$0.02227^{+0.00074}_{-0.00074}$	$0.02006 \rightarrow 0.02452$
$\theta_{13}/^\circ$	$8.54^{+0.15}_{-0.15}$	$8.09 \rightarrow 8.98$	$8.58^{+0.14}_{-0.14}$	$8.14 \rightarrow 9.01$
$\delta_{CP}/^\circ$	$234^{+43}_{-31}$	$144 \rightarrow 374$	$278^{+26}_{-29}$	$192 \rightarrow 354$
$\frac{\Delta m_{21}^2}{10^{-5} \text{ eV}^2}$	$7.40^{+0.21}_{-0.20}$	$6.80 \rightarrow 8.02$	$7.40^{+0.21}_{-0.20}$	$6.80 \rightarrow 8.02$
$\frac{\Delta m_{3\ell}^2}{10^{-3} \text{ eV}^2}$	$+2.494^{+0.033}_{-0.031}$	$+2.399 \rightarrow +2.593$	$-2.465^{+0.032}_{-0.031}$	$-2.562 \rightarrow -2.369$
				$\begin{bmatrix} +2.399 \rightarrow +2.593 \\ -2.536 \rightarrow -2.395 \end{bmatrix}$

**Figure 2.2** – The global best-fit values for the three flavor neutrino oscillation fits as of November 2017. The first column shows results assuming the normal ordering while the second column shows the results for the inverted ordering. Image taken from [58]

## 2.5 Unitarity and Sterile Neutrinos

While global fits assume three flavors of neutrinos, additional neutrino flavors are theoretically possible. The number of active neutrino flavors is limited to the three known flavors from the measurements of ALEPH (see the discussion of Section ??), although such measurements implicitly only measure the number of species with a coupling to the Z boson [9]. Additional flavors with no or very small couplings to the Z boson may be allowed [59]. New neutrino flavors introduced with these properties are known as *sterile neutrinos*.

### 2.5.1 Sterile Neutrinos

Models of sterile neutrinos assume that no weak interactions are available to the new species, leaving only interactions with the world via oscillations. In this model, neutrinos oscillate using a 4x4 (or larger NxN) PMNS matrix [40, 60, 61, 59].

$$\begin{pmatrix} \nu_e(x) \\ \nu_\mu(x) \\ \nu_\tau(x) \\ \nu_s(x) \end{pmatrix} = U_{4 \times 4} \begin{pmatrix} \nu_e(x) \\ \nu_\mu(x) \\ \nu_\tau(x) \\ \nu_s(x) \end{pmatrix} = \begin{pmatrix} U_{e1} & U_{e2} & U_{e3} & U_{e4} \\ U_{\mu 1} & U_{\mu 2} & U_{\mu 3} & U_{\tau 4} \\ U_{\tau 1} & U_{\tau 2} & U_{\tau 3} & U_{\tau 4} \\ U_{s1} & U_{s2} & U_{s3} & U_{s4} \end{pmatrix} \begin{pmatrix} \nu_1(x) \\ \nu_2(x) \\ \nu_3(x) \\ \nu_4(x) \end{pmatrix} \quad (2.19)$$

The additional terms in  $U_{4 \times 4}$  lead to new mixing angles,  $\theta_{14}$ ,  $\theta_{24}$ , and  $\theta_{34}$ . The new terms may be used in the standard oscillation framework introduced in Section ?? extended with a fourth flavor state,  $\nu_s$ , and mass state,  $\nu_4$ .

$$P(\nu_\alpha \rightarrow \nu_\beta) = \sum_i^4 U_{\beta i}^* U_{\alpha i} \sum_j U_{\beta j} U_{\alpha j}^* e^{i(E_i - E_j)t} \quad \alpha, \beta = e, \mu, \tau, s \quad (2.20)$$

Unlike the three active neutrinos, sterile neutrinos cannot interact with matter, leading to a deficit in the neutrino rates from oscillations of the form  $P(\nu_\alpha \rightarrow \nu_s)$ . The location and size of the deficit is determined by the oscillation parameters associated with the  $\nu_s$  and  $\nu_4$  states. Sterile neutrinos may be indirectly observed through this deficit by studying the active neutrinos with either charged current or neutral current interactions.

## 2.5.2 Direct Searches for Steriles

While oscillation of the three active neutrinos preserves the total neutral current rate, sterile neutrinos do not. This provides a unique experimental signature for sterile neutrinos. Dedicated searches for this disappearance have been performed by MINOS [62, 63] and NO $\nu$ A [64] with assumptions on the new terms of the mixing matrix. The effect of three sterile hypotheses on the MINOS data is shown in Figure ???. Around 15% of the neutral current events disappear in the three hypotheses tested by MINOS. The results of the NO $\nu$ A search are shown in Figure ??.

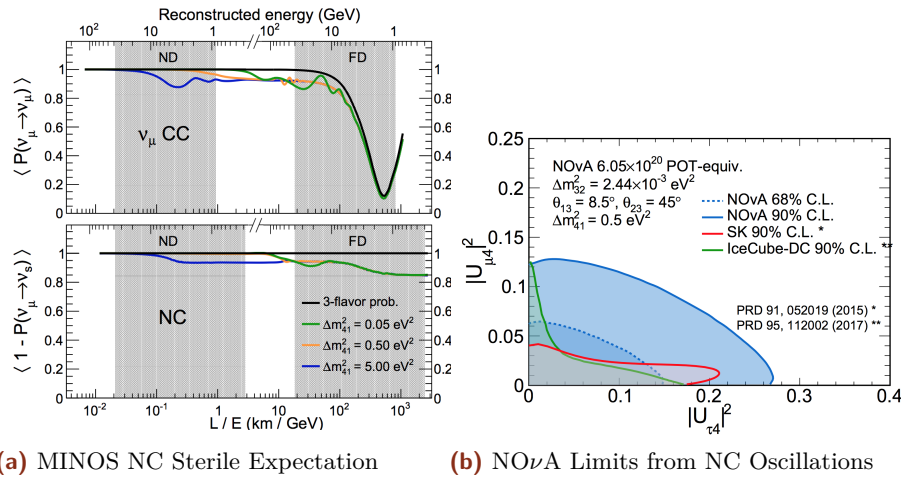


**Figure 2.3** – Expectations (a) and results (b) of searches for sterile neutrinos in the neutral current interactions. (a) Effect of three hypothetical sterile neutrinos on the measurements of the MINOS detector [63]. "ND" and "FD" refer to the near and far detector of MINOS respectively. The sterile neutrinos have a small effect on the main oscillation minimum in the charged current channel, but up to 15% of the neutral current events are lost. (b) The results of the NO $\nu$ A search for sterile neutrinos using neutral current events. The limits are interpreted in terms of the 4x4 PMNS mixing elements in order to compare to searches with charged current interactions in Super-Kamiokande [65] and IceCube [66].

Most experiments attempt to investigate one of the additional terms only, assuming the remainder to be negligible [65, 66, 67]. The results rule out large mixing between a hypothetical sterile neutrino and the three active flavors, although small mixing angles are still allowed by experiments [61, 59].

## 2.5.3 Indirect Searches for Steriles Using Unitarity

Experiments need not search for direct evidence of new mixing terms, however. The addition of a fourth generation of neutrino would have consequences for neutrino oscillation measurements performed in the 3x3 PMNS framework. Standard 3-flavor oscillation measurements may therefore be used to place limits on sterile neutrinos.

The PMNS matrix gives the change in basis and is assumed to be unitary. The unitary condition imposes summation rules for both the rows and columns of the matrix.

$$\sum_i U_{\alpha i} U_{\beta i}^* = \delta_{\alpha\beta} \quad \alpha, \beta = e, \mu, \tau \quad (2.21)$$

$$\sum_i U_{\alpha i} U_{\alpha j}^* = \delta_{ij} \quad i, j = 1, 2, 3 \quad (2.22)$$

If the neutrino mixing matrix consists of more than the three known active neutrinos, however, these unitary relations would only hold in higher dimensions. When projected down to the observed 3x3 PMNS matrix, non-unitarity would be observed.

Neutrino oscillation measurements are performed with the assumption of 3x3 unitarity imposed, allowing the PMNS matrix to be rewritten in terms of three mixing angles and a single phase. The appearance and disappearance probabilities in oscillation measurements are typically written in terms of these mixing angles. Using these mixing angles, the disappearance probability for atmospheric oscillations of  $\nu_\mu \rightarrow \nu_\tau$  is given by

$$\begin{aligned} P(\nu_\mu \rightarrow \nu_\mu) &= 1 - \left| \sum_i U_{\mu i}^* U_{\mu i} e^{-im_i^2 L/2E} \right|^2 \\ &= 1 - \left( \cos^2 \theta_{13} \sin^2 2\theta_{23} + \sin^4 \theta_{23} \sin^2 2\theta_{13} \right) \sin^2 \left( \frac{\Delta m_{31}^2 L}{4E} \right) \\ &\approx 1 - \sin^2 2\theta_{23} \sin^2 \left( \frac{\Delta m_{31}^2 L}{4E} \right). \end{aligned} \quad (2.23)$$

where the final approximation has been made due to the small value of  $\theta_{13}$ . The atmospheric appearance probability,  $\nu_\mu \rightarrow \nu_\mu$ , is given by

$$\begin{aligned} P(\nu_\mu \rightarrow \nu_\tau) &= \left| \sum_i U_{\mu i}^* U_{\tau i} e^{-im_i^2 L/2E} \right|^2 \\ &= \left( \cos^2 \theta_{13} \sin^2 2\theta_{23} \right) \sin^2 \left( \frac{\Delta m_{31}^2 L}{4E} \right) \\ &\approx \sin^2 2\theta_{23} \sin^2 \left( \frac{\Delta m_{31}^2 L}{4E} \right). \end{aligned} \quad (2.24)$$

The form of the oscillation probabilities for appearance and disappearance are very similar when written in terms of the mixing angles. However, the appearance and appearance probabilities in neutrino oscillation measurements depend on different elements of PMNS mixing matrix. Because of the difference in the elements probed, appearance and disappearance measurements may be interpreted to give limits on the fundamental elements of the mixing matrix without imposing unitary.

This method of searching for sterile neutrinos may be applied to global fits, reinterpreting standard oscillation measurements to place limits on the size of any non-unitarity. Using the unitarity conditions of Equation ?? and ??, limits on the size of non-unitarity have been calculated[68]. Experimental constraints from a number of experiments (see reference 26 of [68]) were used to evaluate the best-fit mixing matrix. The unitarity constraints were tested by looking at the potential deviation of each row or column

$$\Delta U_\alpha = 1 - \left( |U_{\alpha 1}|^2 + |U_{\alpha 2}|^2 + |U_{\alpha 3}|^2 \right) \quad \alpha = e, \mu, \tau \quad (2.25)$$

or

$$\Delta U_i = 1 - \left( |U_{\alpha i}|^2 + |U_{\beta i}|^2 + |U_{\delta i}|^2 \right) \quad i = 1, 2, 3 \quad (2.26)$$

The results are shown in ???. The constraints on unitarity of the 3x3 mixing matrix are strongest in the muon and electron sector, with constraints nearly an order of magnitude stronger than that observed in the tau sector. This is a result of limited measurements directly involving  $\nu_\tau$  oscillations.

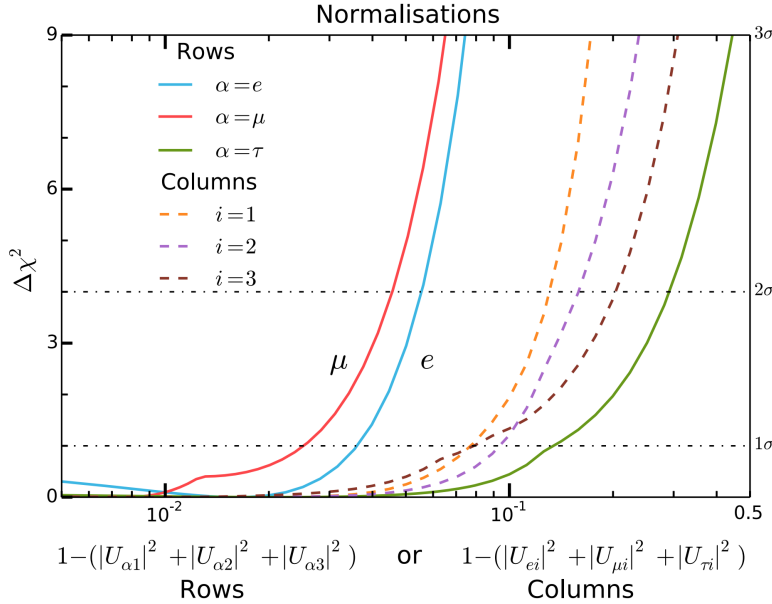


**Figure 2.4** – The results of the tests using ?? (solid) and ?? (dotted). A smaller value on the x-axis indicates a tighter constraint on observed unitarity of the 3x3 mixing matrix. Tests involving only muon or electron flavors show significantly tighter constraints than those including the tau flavor. Image taken from [68]

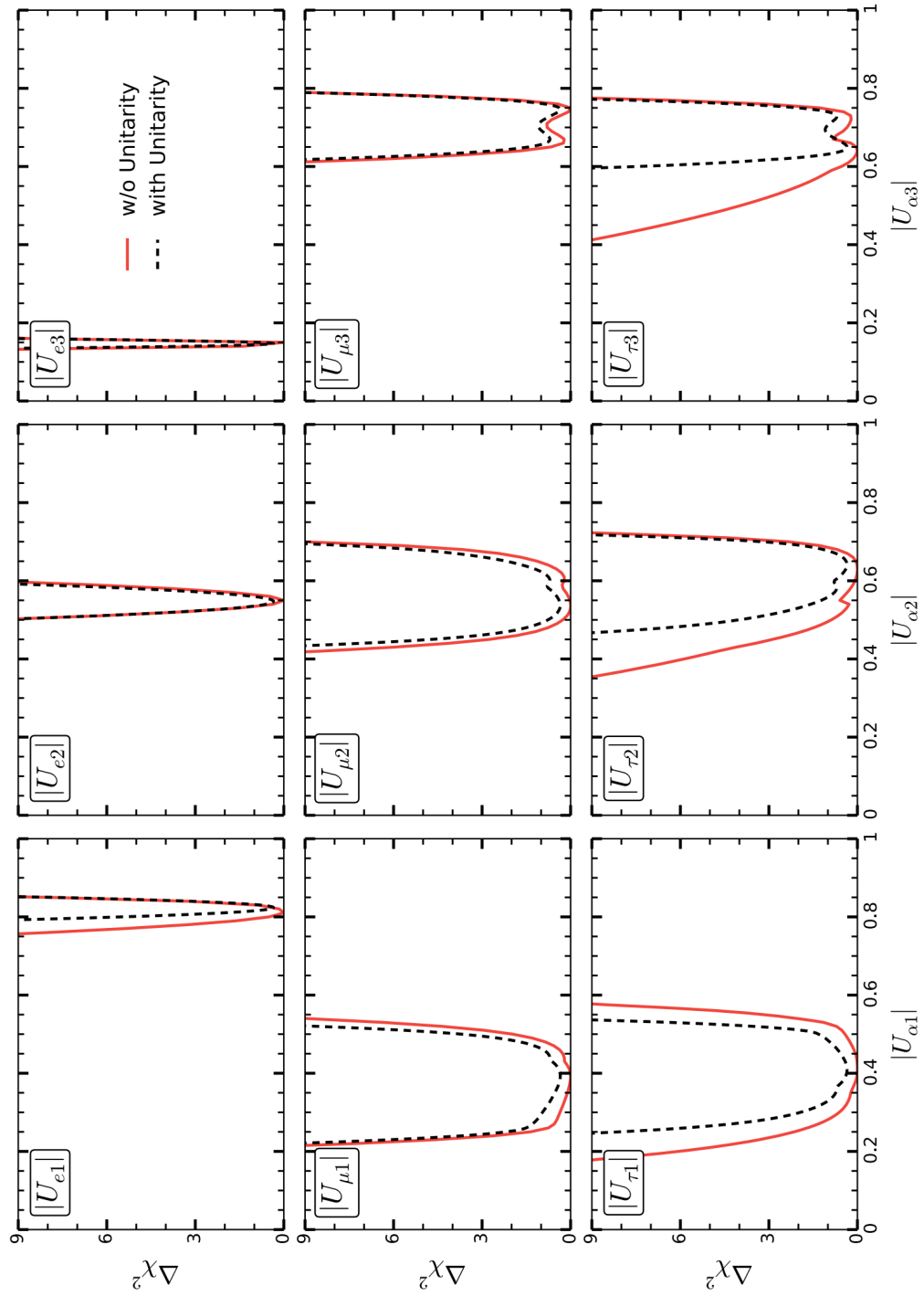


**Figure 2.5** – The constraints from a global fit to neutrino oscillation data[68] with an assumption of unitarity (black dotted) or no assumption of unitarity (red solid). The first two rows show little change from the unitarity assumption, indicating strong constraints from direct measurements. The elements of the third row, related to the  $\nu_\tau$ , show much larger changes, indicating that constraints are obtained from indirect oscillation measurements.

When the individual limits for each element of the 3x3 PMNS matrix are checked, it is the tau sector that shows the largest uncertainties. Measurements of  $\nu_\tau$  oscillations therefore can provide valuable information on unitarity in the neutrino sector, leading to indirect constraints on sterile neutrino hypotheses.

# The IceCube Detector

The low cross section of neutrinos is a challenge for experimentalists. There exist two avenues for the measurement of neutrinos. The precise measurements of individual events, used most notably in the OPERA [22] and DONUT [[Description-DONUT](#)] to identify individual events, gives unique constraining power with low backgrounds. More common, however, is the use of large experimental volumes to collect high-statistics neutrino samples. For the study of atmospheric neutrinos, volumes on the order of a kiloton are required.

The IceCube Neutrino Observatory is currently the largest neutrino detector in the world, encompassing a volume of  $1 \text{ km}^3$  of glacial ice at the geographic south pole. The design of the IceCube detector is also presented in this chapter, beginning with a description of the DOMs that make up the primary detectors within the IceCube observatory (Section ??). The overall geometry of the detector is discussed in Section ?? with a focus on the differences between the larger IceCube detector and the DeepCore subarray used for oscillation searches.

## 3.1 The DOM: The Basic Unit of IceCube

### 3.1.1 The Photomultiplier Tube

The basic unit of the IceCube detector is the *digital optical module*, often referred to simply as the *DOM* [37]. The DOM is designed around a downward-facing 10 inch R7081-02 photomultiplier tube (*PMT*) from Hamamatsu Photonics [69, 70] and includes onboard electronics for standard operation as shown in Figure ???. Circuit boards are included for data acquisition, control, calibration, communications and power conversion as well as for high voltage input from the surface. The electronics of the DOM are encased in a spherical glass housing designed to withstand the high pressures associated with operation in the glacier of Antarctica. The PMT is optically coupled to the glass housing in order to minimize distortion of incoming light.

A discriminator onboard the DOM is used to identify signals from the PMT with a voltage threshold corresponding to 0.25 photoelectrons. Each discriminator crossing begins a *DOM launch*, the lowest level signal available in the IceCube detector containing

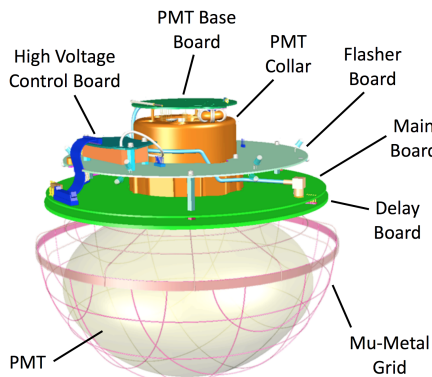


**Figure 3.1** – The IceCube DOM contains multiple components, including the PMT itself as well as various electronics necessary for semi-autonomous operation.

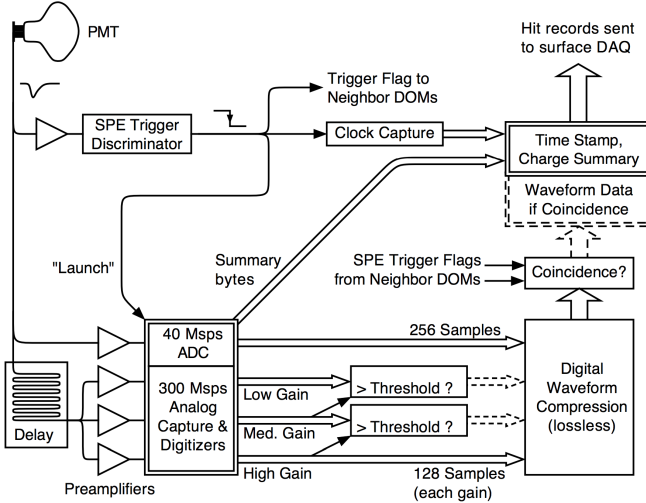


**Figure 3.2** – A schematic diagram of the onboard launch system for the IceCube DOMs. Taken from [37]

a digitization of a raw PMT output in the form of a *waveform*. Information from the PMT is digitized using the fast analog-to-digital converter (*fADC*), which provides binned information at 40 megasamples/second for the 6.4 microseconds following the initial DOM launch. Simultaneously, the analog signal is recorded by the onboard custom integrated circuits known as *Analog Transient Waveform Digitizers* (*ATWDs*) for possible high quality digitization. Launches are recorded in DOM memory while awaiting a decision from the triggering system.

### 3.1.2 Local Coincidence

If any of the notified DOMs also record a launch within a configurable 1 microsecond window, both launches are said to form a *hard local coincidence* (*HLC*) pair. Nearby DOMs, here defined to be either of the two DOMs above or below the current DOM, are notified of the launch via a signal sent using the *local coincidence* wiring. In this situation, all DOMs participating in the HLC begin producing higher quality digitizations from the recorded analog signals using the ATWDs. Launches which fail to satisfy the local coincidence conditions are referred to as *soft local coincidence* (*SLC*) hits. Launches digitized as part of an HLC pair receive a flag. This flag may be used to later identify only those launches which satisfy the local coincident conditions, providing a simple, default method of identifying hits likely to be caused by particle interactions in the detector.

### 3.1.3 Digitization

Signals from the PMT are digitized using a variety of digitizers, shown in Figure ???. Each DOM contains two ATWD chips, each of which has access to three amplifier gain levels in order to cover the dynamic range of the PMT. The highest gain channel is used for most pulses, although lower gains are used in cases of particularly large pulses in order to avoid loss of information due to saturation of the channel. The ATWD chips sample the waveform at a rate of 300 megasamples/second with 128 samples per launch, recording a total of 427 nanoseconds. A 10 meter long delay line embedded in the circuitry of the DOM allows the ATWD to record signals from approximately 75 nanoseconds before the discriminator crossing.

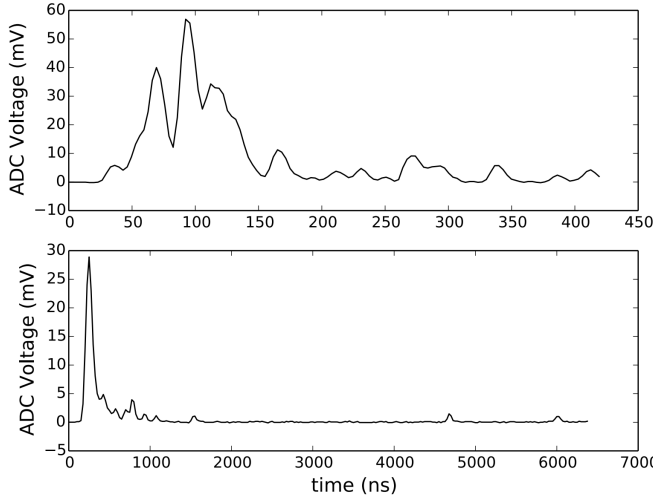


**Figure 3.3** – Examples of the ATWD (top) and FADC (bottom) waveforms output from an IceCube PMT. Taken from [37]

When digitizing a signal, the ATWD chip experiences 29 microseconds of deadtime [37]. During this time, the secondary ATWD is available to record further pulses, resulting in a total average fractional deadtime per DOM of  $2.2 \times 10^{-5}$  seconds/second.

Examples of digitized waveforms from the ATWD and fADC are shown in Figure ??.

### 3.1.4 Triggering in IceCube

Digitized versions of the waveforms are transmitted from the DOM to the IceCube physics data acquisition system (*pDAQ*) for use in trigger and event building. The most common type of trigger used in IceCube analyses is the *Simple Majority Trigger* or *SMT*. This trigger is designed to look for coincidences between DOMs using HLC launches. Each of the SMTs is defined by three fundamental configurations: a DOMSet, which lists the DOMs available for use in the trigger conditions; a threshold number of HLC launches before the trigger fires; and a time window length in which the HLC are required to coexist.

Once all triggers are identified, a *global trigger* is defined. This consists of the superset of all triggers occurring within 10 microseconds of one another. All detector readout enclosed within the global trigger as well as additional information within an additional 10 microseconds both before and after the trigger is combined into a single *event*.

## 3.2 The Geometry of the Detector

The IceCube detector is located at the geographic south pole in Antarctica. The Antarctic glacier forms a 3 km deep surface of clear ice over the bedrock. IceCube uses the Antarctic glacier as both a support structure and as a detection medium for Cherenkov radiation. The IceCube observatory consists of three distinct subarrays, shown in Figure ??, each optimized for separate physics measurements. A total of 5160 DOMs make up the IceCube in-ice array with an additional 324 DOMs used at the surface in the IceTop air shower array [37]. IceCube DOMs are deployed at depths between 1450 m and 2450 m below the surface to shield the detector from atmospheric background muons. The DOMs are deployed in a hexagonal grid in a series of 86 *strings*, each of which provides connections and support for 60 DOMs. Strings are spaced approximately 125 m apart

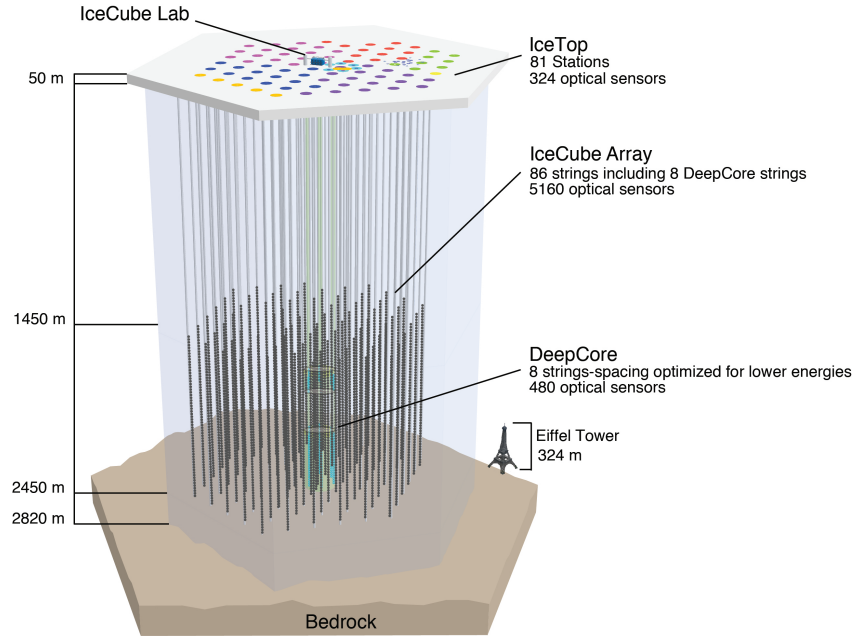


**Figure 3.4** – The IceCube Neutrino Observatory. Three separate subdetectors are shown: IceTop, a cosmic ray air shower detector; IceCube, an array designed to search for astrophysical neutrinos; and DeepCore, a dense subarray optimized for atmospheric oscillation physics measurements. The detector was deployed over multiple years. Strings deployed in the same year are shown with identical colors at the surface.

with DOMs space 17 m apart on each string. Each DOM in the IceCube detector is assigned a unique string number (1-86) and DOM number (1-60).

Additional strings were installed in the glacier annually from 2004 until 2010 with partial detector data collected during construction. During the final years of construction, a denser section of the detector was built, known as DeepCore [71]. The DeepCore subarray consists of 8 strings equipped with high quantum efficiency PMTs 35% more sensitive than the standard IceCube DOM [69]. The DeepCore strings are split between a *fiducial* volume, in which 50 DOMs are spaced 7 m apart on a string, and a *veto plug* of 10 DOMs 10 m apart as shown in Figure ???. The DOMs in the DeepCore fiducial volume are located in the clearest ice of the detector at depths between 2100 m and 2450 m below the surface [72]. The veto cap, installed between 1750 and 1850 m below the surface, is used to identify background muons for DeepCore.

### 3.2.1 IceCube: A Detector for TeV Neutrinos

The IceCube detector is a regularly spaced hexagonal grid buried in the glacier with the proposed purpose of measuring astrophysical neutrino candidate events and identify the source of cosmic rays. The IceCube array has an energy threshold of around 50-100 GeV with an optimal response above 1 TeV[71, 37].

In the standard IceCube detector, an SMT using all DOMs with a threshold of 8 HLC launches within 5 microseconds is typically used [37]. This trigger, known as *SMT8* after the number of required hits, is designed for high signal efficiency at energies above 100 GeV with a minimum number of accidental triggers due to random detector noise. The IceCube detector records an SMT8 rate of around 2100 Hz with less than 1 Hz expected from neutrino interactions.

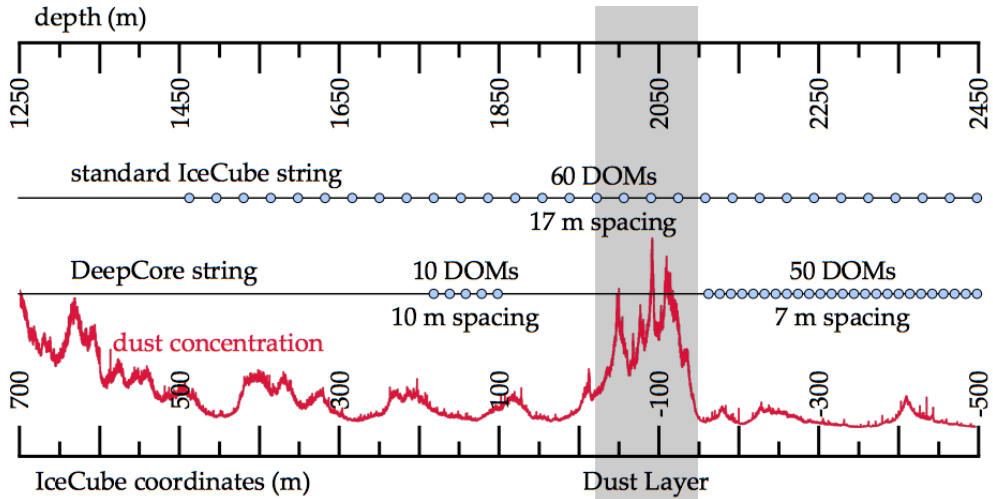


**Figure 3.5** – A comparison of the standard IceCube string (right) to the DeepCore string (left). The IceCube string uses DOMs spaced 17 m apart while DeepCore divides the DOMs into a fiducial (bottom) and veto plug (top). The dust concentration is shown in red. The concentration of dust in the ice affects the scattering and absorption of the glacial ice.

Events at the TeV scales of the IceCube detector show well-defined topologies, as shown in Figure ???. The IceCube detector has performed many measurements, including searches for sterile neutrinos [67], anisotropy in the cosmic ray flux [73], measurements of the neutrino cross section at high energies [74], and the first discoveries of an astrophysical neutrino flux [75].

### 3.2.2 DeepCore: Extending the Reach to GeV Scales

The DeepCore detector was designed to be a smaller, denser detector optimized for the measurement of atmospheric neutrino oscillations. The denser spacing and clear ice of DeepCore lower the energy threshold to around 10 GeV [71], permitting the study of oscillations. DeepCore was installed at the bottom of the IceCube array near the center of the IceCube hexagonal grid.

In DeepCore, the desire for lower energy events led to the introduction of a separate trigger, known as *SMT3*. This trigger, using only DOMs within the DeepCore fiducial volume, searches for at least three HLC launches occurring within 2.5 microseconds. This effectively lowers the triggering threshold from roughly 100 GeV with the larger IceCube array to approximately 10 GeV. The SMT3 rate, at 250 Hz [37, 71], is substantially smaller than the SMT8 rate due to both the increased overburden as well as the smaller number of PMTs included in the SMT3 DOMSet. By placing the detector inside of the larger IceCube array, DeepCore allows analyzers to use the IceCube detector as an active veto, reducing the background rate to 17 Hz.

DeepCore events do not show the clean topological separation of the higher energy IceCube events as seen in Figure ???. Events may be separated broadly into *cascade-like* and *track-like* statistically using information contained in the timing of hits in the detector. Such separation techniques are energy-dependent and do not perform well at very low energies.

DeepCore has observed atmospheric neutrino oscillations in the  $\nu_\mu \rightarrow \nu_\tau$  in the disappearance channel [78, 79, 80], with the most recent measurement showing competitive precision to dedicated measurements performed with particle accelerators.

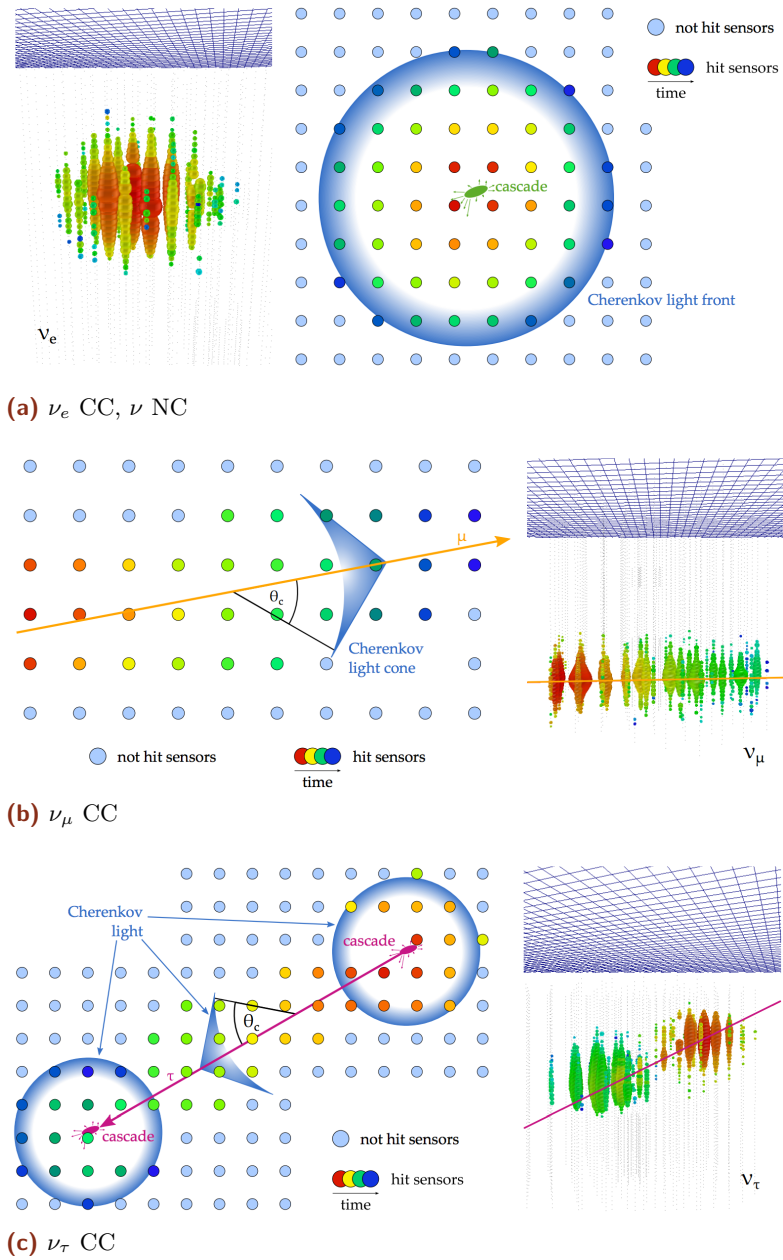


**Figure 3.6** – Examples of event topologies above 1 TeV using the full IceCube array. Event views shown in (a) and (b) are from actual events discovered by the IceCube detector [76]. Images taken from [77]. (a)  $\nu_e$  CC and  $\nu$  NC show similar behavior from electromagnetic and hadronic interactions, which result in a shower of particles that quickly scatter in the ice. Cherenkov emission from these events appears roughly spherical in the detector. These events are known as "cascades". (b)  $\nu_\mu$  CC events begin with a hadronic interaction, then produce Cherenkov light from the outgoing muon. Above 1 TeV, the track of the outgoing muon becomes clearly visible. (c) Above 10 TeV, the tau lepton from a  $\nu_\tau$  CC may travel a significant distance before decaying. This results in two well-separated cascades in the detector, a tell-tale signature of  $\nu_\tau$  CC interactions.

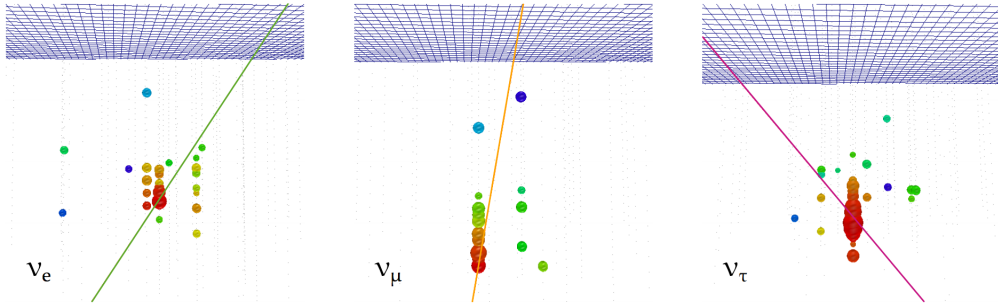


**Figure 3.7** – A selection of 50 GeV simulated events in DeepCore taken from [77]. Unlike the event topologies at high energies, DeepCore events do not show distinct event types.

While DeepCore was designed for oscillation physics, the neutrinos may be used for other purposes as well. Recent work with DeepCore has shown sensitivity to studying dark matter interactions in the sun [81] and in the galaxy [82].

### 3.3 Optical Properties of the Antarctic Glacier

#### 3.3.1 The Bulk Ice Model

The Antarctic glacier, with a thickness of 2.8 km at the geographic south pole [72], forms both the support structure and the interaction medium for IceCube. During deployment, measurements of the scattering properties of the ice were taken during deployment of the IceCube strings. The IceCube dust logger emitted laser light aimed into the undrilled ice and detected backscattered photons[83, 84]. The results are shown in Figure ??

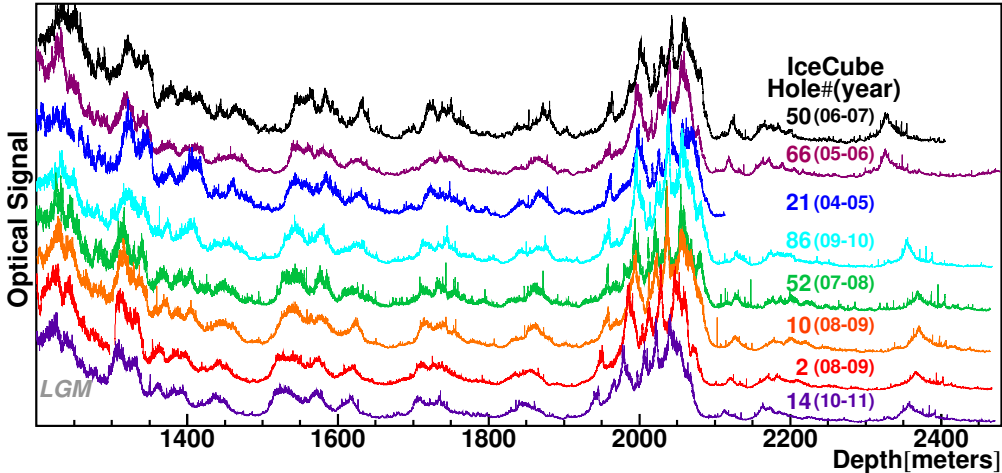


**Figure 3.8** – The data from the dust loggers deployed in various drill holes in IceCube during deployment. Data from individual holes has been offset in the y direction for clarity. Larger relative values of the "Optical Signal" represent more scattering in the ice while smaller values indicate clearer ice. The "dust layer" is visible in all drill holes around 2000 m. Deepcore DOMs are deployed below this layer. Image taken from [85].

Peaks are present in the dust logger data due to volcanic events in the Earth's past [83]. The most significant peak, a set of features around a depth of 2000 m, form what is known as the *dust layer* of IceCube, a region with significantly higher scattering and absorption properties than the surrounding ice.

To improve the modeling of the glacier, dedicated measurements have been performed using light-emitting diodes (LEDs, also known as *flashers* in IceCube) onboard the DOMs [72, 37]. In specialized calibration runs, the LEDs are flashed at a few Hertz for a few minutes while nearby DOMs receive the emitted light. Monte Carlo simulations of the flashers are used with varying ice properties in order to identify the most likely properties of the ice. Each flashing and detecting DOM pair provides a set of known times, positions, and light output in the ice, allowing for the properties of the intervening medium to be determined.

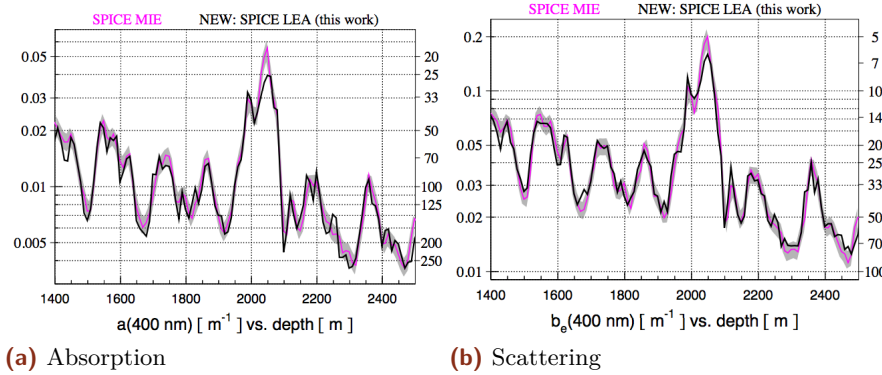


**Figure 3.9** – The absorption and effective scattering properties of the ice as fit to flasher data. Two models are shown representing different generations of ice models used for simulation. The "Mie" model does not include anisotropy while the "Lea" model does. Figure from [86].

The modern ice model used for this thesis consists of three main properties: the absorption, the scattering, and the anisotropy of the ice [86]. The measured properties of the absorption and scattering may be seen in Figure ?? while the effect of the anisotropy can be seen in Figure ???. Scattering photons change direction, losing information about the direction of the emission source. Absorbed photons are not visible to the detector, potentially modifying the observed number of photons and the reconstructed energy of an event. The anisotropy, consisting of a direction and magnitude, modifies the ice properties as a function of direction due to movement and compression of the glacier over time. The anisotropy affects both the scattering and absorption from each direction in the x-y plane and can affect the azimuthal directions of reconstructions in IceCube.

### 3.3.2 The Hole Ice

After the strings were deployed, each drill hole was allowed to refreeze. The refrozen column of ice around each string is referred to as the *hole ice*. Using a dedicated camera deployed at the bottom of string 80, the refreezing process of the hole ice has been observed over the course of several years [87, 37]. Images obtained from the camera show the refrozen ice divided into three distinct regions.

The outermost region, the *bulk ice*, is the original glacial ice and is unaffected by the deployment of the detector. The outer part of the drill hole shows improved clarity compared to the bulk ice. The central region of the drill hole, a central core of about 16 cm in diameter, shows significantly worse scattering properties than the bulk ice [37]. This central column, referred to as the *bubble column*, affects the photon acceptance of the PMT. Measurements to characterize the hole ice are ongoing.

find good quality  
swedish camera pics?

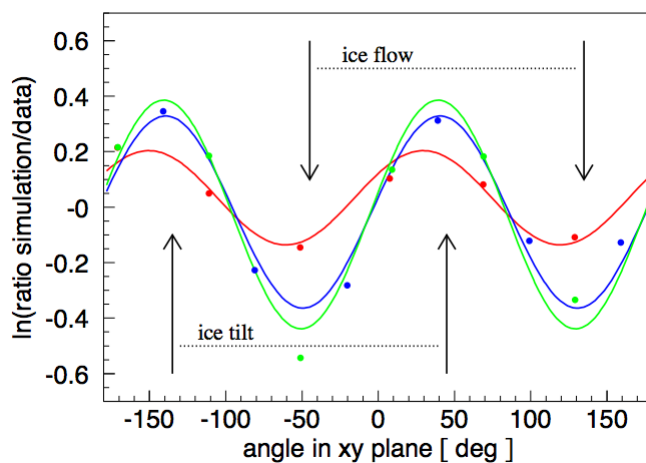


**Figure 3.10** – The effect of the anisotropy on the light output from a flasher on string 63. Measurements (points) are shown for receiving DOMs at three distances: at 125 m (red), at 217 m (blue), and at 250 m (green). A line is included to show the expected effect of anisotropy at each distance. The y-axis shows the ratio of a simulation of the same flasher without including anisotropy to data. A modulation is observed as a function of direction in the x-y plane.

# Simulation of the IceCube-DeepCore Detector

## 4.1 Monte Carlo Generators

### 4.1.1 Background Generation

#### CORSIKA

The primary background for the observation of atmospheric neutrino events is the other particles present in the cosmic ray interactions in the atmosphere. These interactions produce many particles, most of which are stopped before reaching IceCube by the shielding provided by the Antarctic Glacier. In order to correctly account for the interactions and decays of these particles, the *CORSIKA* generator from the KASCADE Collaboration is used. The *CORSIKA* generator is a collection of code designed to simulate, interact, and propagate a cosmic ray air shower from the interaction point in the upper atmosphere to the surface. Originally designed for use with surface detectors such as Auger, HAWC, and IceTop, the code has been adapted for use in the IceCube collaboration by identifying the muon (and, sometimes, neutrino) components of the air shower.

*CORSIKA* has many modes of operation and options for configuration. The standard IceCube simulation of air showers uses the SIBYLL 2.1 hadronization model to follow the interactions through the shower. The low-energy tail of the showering code is handled by a separate hadronization parametrization, but is not relevant for the muon interactions visible in the IceCube detector.

The showers are produced assuming a primary cosmic ray spectrum. Two options are used in IceCube for the simulation of the primary spectrum. The Polygonato model, which throws cosmic rays approximately following the best fit from Hoerandel 20XX. The model requires a selection of a season to simulate due to the annual modulation of the muon flux due to temperature changes in the atmosphere. In typical IceCube simulation, *CORSIKA* produced using the Polygonato model includes a mixture of muons from all seasons, effectively producing an averaged flux useful under the assumption of equal livetime throughout the year. While this model is out-of-date and not used in recent analyses, it provides a similar shape to newer models until the knee in the cosmic ray spectrum. The natural spectrum of the Polygonato *CORSIKA* simulation has the benefit of allowing a direct physical interpretation of the resulting spectrum without the need for reweighting and simplifies the production of coincident showers, which require a natural spectrum for weighting.

The second model, the five-component mode, reduces the full spectrum of cosmic rays to five effective families: hydrogen, helium, nickel, aluminum, and iron. Each of these components is allowed to have different spectral properties. Elements within each family are assumed to behave similarly. The five-component mode is useful due to the ease with which the user can modify and reweight to different primary spectra, allowing the investigation of different models without the production of dedicated simulation. The simplicity associated with the reweighting of five-component simulation allows IceCube to produce unphysical spectra in order to optimize the production of simulated events necessary for the various analyses. While this slightly complicates the use of the simulation

in analyses, the ability to test with various spectra has been an invaluable tool for high energy analyses, which can be sensitive to changes in the cosmic ray spectrum above the knee. Five-component CORSIKA simulation, due to the unphysical generation spectrum, cannot easily be used for coincident production directly and are currently supplemented by the Polygonato CORSIKA for this purpose.

In both cases, the particles from the air shower are only propagated to the surface of the ice. For analyses using the in-ice array, we take the muons reaching the surface from a CORSIKA simulation and propagate them through the ice, simulating the continuous and stochastic energy losses along the way. The muons are propagated to a surface in the ice consisting of a cylinder with radius 800 meters and length 1600 m centered on the IceCube detector. In order to reach the detector, a muon must result from a cosmic ray interaction of approximately 600 GeV due to the shielding of the glacier. Because of this, CORSIKA simulations typically have a lower energy cutoff of about this value to avoid simulating events that will not reach the detector.

In principle, neutrinos may also be produced using the CORSIKA generator. In practice, this tends to be extremely inefficient for most searches that are no explicitly looking for muons and neutrinos from the same air showers given the extremely low cross section of the neutrino relative to the muon. For this reason, the background generation with CORSIKA in IceCube typically refers to muon events only with no accompanying neutrino.

## MuonGun

In many situations, the full CORSIKA generation is unnecessary and wasteful. In situations where the needed muon simulation falls within a relatively narrow phase space, whether that be in energy, angle, or position inside of the detector, it can be beneficial to taylor simulation to the needs of analyzers. Alternatively, there are situations in which the details of the cosmic ray interactions are an unnecessary complication to the final level IceCube analyses. In these situations, IceCube has developed a tool to bypass the full air shower simulation provided by CORSIKA, instead skipping directly to the cylindrical surface inside the ice. This tool, known as *MuonGun*, has the benefit of removing the computationally costly simulation of the full air shower and giving the user more control over the resulting simulated events.

In this generator, the muons are produced on a *generation cylinder* with a radius of 800 meters and length of 1600 meters, matching the final muon positions of the CORSIKA generator. The muons are pulled from a power law spectrum of the user's choice: in this work, an offset power law spectrum is chosen with break at 700 GeV and a range of 160 GeV to 100 TeV. The lower energy range is selected by using CORSIKA simulation to identify the minimum energy required for a muon at this surface to reach and trigger the DeepCore detector.

The angular spectrum of the MuonGun simulation is created by setting a *target cylinder* toward which the generated muon must intersect. For this work, the target is chosen to be the DeepCore fiducial volume, encompassing a cylinder with radius 150 meters and length 500 meters centered on DeepCore at  $x=(46.3, -34.9, -300)$ .

These features of MuonGun give the generator significant flexibility, allowing for a very focused simulation of muons that would not otherwise be possible with the current implementation of the CORSIKA generator. The downside, as with all targeted generation, is of course that one must be aware of the limitations. For example, the settings described above will provide a good description of muons reaching and triggering the DeepCore

array, but will not include the correct contributions of muons in the outer IceCube detector. This can result in disagreement between data and simulation if the limitations are not acknowledged and accounted for.

Of course, this abstraction also disassociates the muon at the detector from the air shower, and therefore the cosmic ray, that produced it. In order to properly account for dependence on the cosmic ray spectrum in the muon spectrum, dedicated simulations must be produced using the full CORSIKA generator. By following the interaction, showering, and propagation to the detector, IceCube is able to produce an effective parametrization of the association between a particular cosmic ray spectrum and the muons reaching the detector. This must only be done once, but requires a substantial number of simulated events in order to produce a clean parametrization in position, energy, zenith angle, and variables associated with shower multiplicities higher than one. The version of MuonGun at the time of writing provides the parametrizations for the Hoerandel and H4a cosmic ray spectra. At the time of production for the analyses contained hereafter, all MuonGun simulation is produced assuming a multiplicity of 1, meaning that no bundles are yet produced with this generator. This is a limitation of simulation time: the multiplicity parametrizations vastly extend the parameter space and therefore require significantly more time and effort to handle correctly.

## Noise-Only Events

While we only observe neutrinos and muons in the detector, we also observe a significant component of accidental triggers in the DeepCore array. These events, labeled *noise triggers*, arise due to the low trigger threshold. In these events, no actual particle interactions due to muons or neutrinos are observed. Instead, detector noise from various sources coincidentally occur in DeepCore in a way that mimics a very low energy neutrino. These events are simulated by skipping the generators entirely and allowing the simulation to trigger on the accidental coincidences. Because the events are relatively rare, the simulation requires a special mode, here called *long-frame* simulation, which produces continuous detector readout. Breaking the traditional concept of the "simulated event", these simulation sets instead produce a 100 ms long "event" of random detector noise with the Vuvuzela module. These hits are then run through the simulation of waveforms, coincidences, and triggering as a normal simulated event. After triggering, specialized code, known as *CoincidenceAfterProcessing* is used to divide the long-frame simulation into smaller events more similar to both other simulation as well as actual experimental readout.

Once the events are generated, weighting the events is relatively straightforward: the weight per event depends on the muon interaction rate and the total simulated time. The latter is straightforward to calculate, depending only on the number of long frame simulation events produced and the time window for each of these events. The former is important due to the definition of the noise triggers. These events are, by definition, only able to occur when no muon or neutrino is interacting with the detector. Therefore, the total effective livetime of the simulation must account for the "deadtime" for noise triggers due to particle interactions. This rate, assumed to be approximately 2800 Hz, leads to a change in the effective livetime per event of roughly 15

Noise triggers are particularly computationally expensive to produce, given that they rely on a relatively rare emergent property of random detector noise. In general, a few minutes of effective livetime can take up to two hours to create, with much of the processing time spent on DOMs and hits that do not make it into final triggered events. This limits the

total effective livetime that can be simulated in realistic timescales. Current simulations used in this work total approximately two months of effective livetime.

### 4.1.2 Signal Generation

#### GENIE

Of course, background simulation is only part of the generation in IceCube. In the end, studies are searching for neutrino candidate events that themselves must be simulated in order to infer properties of the original events. At energies ranging from approximately 1 GeV to 1 TeV, IceCube has adopted the *GENIE* event generator. This code, used widely throughout the oscillation community, includes information about the various interactions, cross sections, and uncertainties involved in neutrino physics from reactor energies upward.

Events in the GENIE generator are produced first by selecting events from a pure power law with a given spectral index, often chosen to be either  $E^{-1}$  or  $E^{-2}$  depending on the purpose. These events are then forced to interact with an electron or nucleon within a specified volume in the ice assuming a constant target density. This is a good assumption, given the small variability in density of the ice due to dust.

The interaction type is determined using the cross section for the given flavor and energy, resulting in a shower of particles. The cross section model, an updated version of GRV98, includes resonant, elastic, quasielastic, and deep inelastic events. The final states are computed using Pythia6, resulting in a final state of particles that is returned to the IceCube software for further processing.

The GENIE code includes tools to reweight events based on uncertainties in eg. the axial masses, cross sections, and various aspects of the interactions themselves. The code is regularly updated, including both new features and retuning of parametrizations to match the latest data. The events produced in this work use GENIE version 2.8.6.

#### Neutrino-Generator

At energies higher than approximately 100 GeV, there are two changes to the simulation code. At these energies, the contribution to the cross section from deep inelastic interactions becomes dominant while the other interactions become negligible. This allows the simplification of the cross section calculations for no loss in generality. In addition, the cross section continues to rise linearly with the energy. This latter feature requires a detailed simulation of potential interactions far from the detector: namely, the higher energy neutrinos have a non-negligible chance of interacting en route to the detector as they pass through the Earth.

The *Neutrino-Generator* code (hereafter, *NuGen*) is designed to handle these higher energy interactions. In this model, neutrinos are no longer produced and forced to interact in the ice directly. Instead, a neutrino is produced from a power law spectrum in the atmosphere surrounding the Earth. The event is then propagated through the planet, using the PREM model of the density layers in the Earth to simulate potential interactions en route. Neutrinos which interact may be lost or may be regenerated following the decay of the daughter particles. The energy loss between parent neutrino and surviving daughter neutrinos is recorded in the NuGen files. The daughters are then forced to interact in the detector fiducial volume to give a simulated event.

NuGen can be configured with various Earth models as well as different generation properties. For the studies contained herein, the NuGen files are produced with an  $E^{-2}$  spectrum and interact following the CSMS cross section.

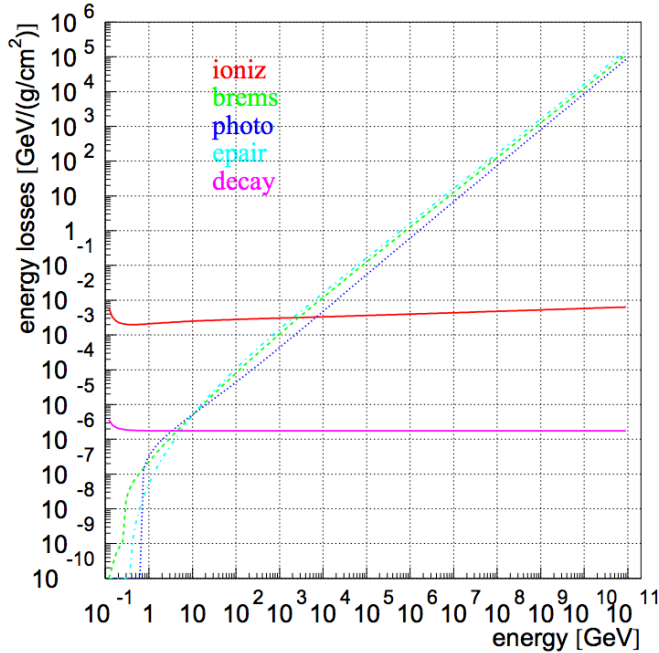


**Figure 4.1** – Average energy losses ( $\frac{-dE}{dx}$ ) for a muon in ice. At very low energies, ionization losses dominate. Above approximately 1 TeV, pair production and photonuclear effects become more important. Image taken from [21]

## 4.2 Propagation of the Particles and Light

### 4.2.1 Modeling with GEANT4

I don't know shit about geant4. Something about how great and wonderous and slow it is at doing particle interactions at low energy.

### 4.2.2 Lepton Propagation with PROPOSAL

At higher energies, events may be simulated following a parametrization of the energy losses instead of direct simulation of the processes and particles themselves. This parametrization, known as *PROPOSAL*, contains tools to simulate the propagation of leptons and hadrons with ionization, electron pair-production, bremsstrahlung, photonuclear interactions, and decay processes. Each of these is done with a parametrization of the associated energy deposition for a given true particle energy as shown in Figure ???. PROPOSAL may be configured with a minimum energy for the stochastic losses, with all losses below this threshold energy being simulated as continuous, rather than stochastic, losses.

Each of the PROPOSAL parametrizations has its own associated uncertainty ranging between 2% and 10%. For some purposes, these uncertainties are somewhat negligible and result in a linear shifting of the final energy of the events at the detector. This could be accounted for using reweighting techniques, but can generally be handled by a loose normalization uncertainty. For particles with energies below approximately 10 TeV, the additional complication due to the increasingly important ionization losses make the calculation of uncertainties due to propagation non-trivial.

### 4.2.3 CLSim for Photon Propagation

Once the energy deposition at each position is calculated with GEANT4 or PROPOSAL, the resulting photons must be propagated. There exist two modules which can handle this:

Photon Propagation Code *PPC* and OpenCL Simulation Code *CLSim*. The differences are largely of implementation details and both have been verified to give identical results. We will therefore only discuss the latter, *CLSim*, for the purposes of this document.

*CLSim* is a code designed to handle the photon propagation in parallelized calculations using an OpenCL device, typically a GPU. The code takes the energy depositions and converts them to photon yields via parametrizations and assumptions about the resulting wavelength spectra of the depositions.

These photons are then propagated through the ice with the current best-fit knowledge about the scattering and absorption properties. Photons continue to scatter until either absorbed or until they reach the face of a PMT in the ice.

At high energies, the light yield is large enough that the propagation of individual photons is both excessively costly as well as unnecessary. In those cases, a feature known as *oversizing* is applied using an oversizing factor typically set to 5. This allows for the production of "weighted photons", which effectively represent bundles of photons with size proportional the square of the oversizing factor. The DOM radius is then increased by the oversizing factor in order to increase the light collection in simulation. With fewer photons to propagate, the simulation proceeds more quickly. The underlying assumptions, that the photon flux is roughly proportional to area and that the flux is high enough that bundles of photons will have similar properties to single photons, is a convenience at high energy when single events may have many photons. This breaks down at low energies, where the photon flux is comparably low and scattering or loss of individual photons matters. Because of the complications associated with oversizing at low energies, most simulations of DeepCore events are done with the oversizing features disabled.

#### 4.2.4 Angular Acceptance and Hole Ice

Once the photons have been propagated to the face of the PMT, an effective angular acceptance is applied. This acceptance, calculated from a combination of lab and in-ice measurements, represents the PMT efficiency as a function of the arrival direction. As expected, the PMT is parametrized to have a negligible efficiency for photons arriving in the downward direction and high efficiency for photons traveling in the upward direction. All other directions follow a curve between these two points. The most forward direction in the PMT, shown with  $\cos(\eta) = 1$ , is thought to be affected by the hole ice (see Section ??).

There exist three models of the hole ice, two of which utilize the angular acceptance parametrization. The first, known as *H2* gives a model with a scattering length of 50 cm in the bubble column. The  $1\sigma$  range, represented by the *H1* and *H3* models, model a bubble column with scattering lengths of 30 cm and 100 cm respectively.

The second, known by the name of the author, *Dima*, is a fit that occurred more recently while simultaneously fitting properties of the ice. This model has been extended with an additional parameter, *p2*, which gives a modification of the most forward region of the PMT. This region is believed to have the most uncertainty, although further studies are ongoing to more directly characterize the most upgoing region.

The last, which exists as part of an updated model of the scattering and absorption in the ice, is labeled *SpiceHD* after the name of the new ice model. This model differs from the previous two in that the hole and bubble column are directly simulated in the ice with no effective angular acceptance curve necessary. In this model, the PMT will have 100% efficiency for any photon reaching the face of the PMT and 0% efficiency for all photons reaching the back of the PMT. This results in a potentially more accurate simulation at the cost of additional processing time and less ease of use for producing systematics sets.

Once the photons have been propagated and the wavelength and angular sensitivity has been applied, the simulation results in a series of *I3MCPE* objects for each DOM. Each I3MCPE represents a single photoelectron worth of charge ejected at the photocathode of the associated PMT.

## 4.3 Simulating the Detector Electronics

### Noise within IceCube-DeepCore

Once the processing of particles and photons has reached the photocathode, detector effects will need to be applied. The first of these, detector noise, is handled by the *Vuvuzela* module in the simulation chain.

Detector noise in IceCube has been studied in depth previously, most notably in my own master's thesis. In brief, studies have shown that there exists a large fraction of the detector noise that displays non-Poissonian behavior in time.

The noise simulation for each DOM is provided by a set of five characteristic parameters, each representing a separate aspect of the assumed process. All five parameters have been previously fit individually for all DOMs using untriggered raw data from the IceCube detector. The simplest of these, the *thermal rate* leads to a standard Poisson process noise model in which all hits are assumed to occur independently with a rate that depends on the temperature of the electronics. The thermal rate appears to fall as the temperature decreases and is a relatively large component of the noise in IceCube DOMs, with typical rates of approximately 200 Hz.

The next component is another Poisson process, thought to be due to radioactive decays in both the ice and the DOM glass. These noise hits occur at a rate that is independent of temperature with a characteristic rate on the order of 50-100 Hz. Studies of these radioactive components are ongoing, with some evidence that Potassium-40 and Uranium-238 may be responsible for at least some of the observed decays.

Once a decay occurs, there is evidence of a rapid series of pulses occurring in the PMT, leading to a "burst" of noise that can last up to millisecond timescales. These hits are believed to be due to a scintillation or luminescence process related to the glass of both the DOM and PMT. In order to model this bursting behavior, an effective model which represents the timing of consecutive hits from the scintillation process is implemented using a log-normal distribution. This introduces three additional parameters to the noise model: the average number of hits in a "burst", giving the normalization; the mean time between hits within a burst; and the standard deviation of the timing within a burst.

Noise hits in simulation are added to the detector in the form of additional I3MCPEs for each DOM. Once the noise simulation is completed, the combination of I3MCPEs due to particles as well as noise are passed to the next modules.

### PMTResponseSimulator and DOMLauncher

The IceCube detector does not directly measure photoelectrons emitted from the photocathode. Instead, the simulated I3MCPEs are converted to *I3MCPulses* within the PMT using the PMTResponseSimulator module. This module, which models the cascading effects within a single PMT, also adds in effects such as the pre-, late-, and after-pulses which are thought to come from defects in the cascading process. The pre-pulses, arriving within a few dozens of nanoseconds prior to the main signal, are thought to arise from the small probability of an electron bypassing one of the dynodes. Late-pulses are likewise thought to be produced by electrons which return to a previous dynode, inducing a signal

a few dozens of nanoseconds immediately following the main signal. These signals tend to be small and generally not of importance in the remainder of this document.

After-pulses, which arise from ionization of residual gases in the PMT, are a more significant concern for the purposes of this work. The ionized atoms tend to travel significantly more slowly than electrons, resulting in a delay between the main signal and the subsequent afterpulses that may be as large as 10 microseconds.

The resulting cascade of electrons in the PMT, now including a combination of pulses due to particle interactions, noise, and PMT effects, is detected at the anode as a voltage drop, with the shape of the voltage change referred to as a *waveform*. When the PMT observes more than a threshold voltage drop, typically corresponding to 1/4 of the expected drop from one photoelectron ejected from the photocathode, the DOM begins recording a *I3DOMLaunch*, often referred to simply as a 'launch'.

The waveform of a launching DOM is passed to two onboard digitizers. The first and more precise of these, the *Analog to Digital Waveform Digitizer*, or *ATWD* will digitize the waveform using 322 bins with 3.3 nanoseconds per bin. Two ATWDs are provided for each DOM, as the digitization process may lead to significant deadtime. In addition, each of the two ATWDs possesses three channels with separate gains. This provides the ability to accurately measure the waveform, even in cases of saturation. The unsaturated ATWD with the highest gain provides a record for the launch.

In addition to the ATWD, there exists a longer-timescale digitizer known as the *Fast Analog-to-Digital Converter*, or *FADC*. The FADC is able to record up to 6.4 microseconds of the waveform in bins of XYZ nanoseconds with no deadtime. This digitizer allows for longer-term behavior to be recorded for the DOM in addition to the detailed information from the ATWD.

As the waveform is being recorded, a signal is sent to nearby DOMs requesting status information. If a nearby DOM, here defined as any of the two nearest above or two nearest below the current DOM, observes a launch within 1 microsecond, then both DOMs are labeled as in *Hard Local Coincidence*, or *HLC*. If no nearby DOM observes a launch within the specified window, then the launching DOM is referred to as having a *Soft Local Coincidence* or *SLC*.

In the case of HLC launches, the DOM will request the full digitization of the waveforms from both the ATWD and FADC, providing a complete record of the launch. If the launch is instead given the SLC label, the information in the ATWD is dumped and the FADC instead digitizes only the three bins associated with the largest peak of the waveform. While this limits the information available for these launches, the lack of associated nearby launching DOMs provides strong evidence of a launch due to random detector noise.

## 4.4 Post-Simulation Processing

### 4.4.1 Pulse Extraction

From this point in the processing, both data and simulation receive identical processing. The first step of this processing is to read and extract charge information from the digitized waveforms. This is done using the *wavedeform* module, which accepts and processes the information from the launches in each triggered event. Wavedeform attempts to reconstruct the original I3MCPulses from the digitized waveform information.

Wavedeform uses a parametrized version of the PMT pulse associated with a single photoelectron. Beginning with a single pulse template, a least squares minimization is performed to find the best-fit timing of the pulse to the observed digitized waveform.

Additional copies of the pulse template are added and new minimizations are performed until the goodness-of-fit improvement from additional pulses is negligible. The resulting sets of pulses, including associated timing and normalization, are returned with the *I3RecoPulse* class, more commonly referred to as simply *pulses*. These pulses represent the best-fit recreation of the analog pulses in the PMT prior to the digitization process. Both HLC and SLC waveforms are fit, although the limited information in SLC waveforms necessarily results in the loss of information. When available, information from the ATWD is provided a larger weight relative to the information from the FADC due to the finer binning in time, allowing for more detailed information on PMT behavior near the beginning of the launch of the DOM.

#### 4.4.2 Hit Cleaning

In general, a set of pulses, known as a *pulse series*, contains a significant amount of information due to random detector noise. These additional pulses are not useful for understanding the particle interactions and are therefore typically removed during processing. There exist multiple ways to identify pulses likely to be due to detector noise, three of which will be detailed in order from most strict to most accepting.

#### LC Cleaning

The most strict cleaning method is also the most straightforward. By selecting only pulses that result from HLC launches, the resulting pulse series can be cleaned of nearly all detector noise. This comes at the expense of a potentially significant amount of information about the event, since all SLC hits are removed.

#### SeededRT Cleaning

Instead of simply using HLC hits, additional processing may be used to identify potentially interesting SLC hits as well. The *SeededRT* algorithm is one such algorithm, requiring a seed, radius, and time in order to search for additional information in the event. SeededRT begins with a subset of "interesting" pulses, often a selection of the HLC pulses, as a seed. Once a seed is selected, a sphere of the given radius is drawn around each seeded DOM. Any nearby DOMs within the sphere and time window are added to the output pulse series. Once all seed DOMs have been checked, a new seed is created composed of the current output pulse series. The process is then run again, once again updating the output pulse series with any newly discovered pulses. Once no additional interesting DOMs are observed, the final pulse series is written out, able to be used for any subsequent processing.

The most effective set of parameters is dependent on the detector geometry, since a given radius sphere will contain more DOMs in the DeepCore fiducial than the same sphere outside of DeepCore. Because of this, different settings are chosen for these two regions.

#### Time Window Cleaning

The most general cleaning results in very little loss in pulses due to particle interactions, but allows nearly all noise pulses into the final hit series. This *Static Time Window* cleaning, often referred to using just the acronym *STW* cleaning, looks for pulses near the times associated with triggers. For DeepCore processing, any pulses more than 4 microseconds before or more than 6 microseconds after the SMT3 time are removed.

There exists a second type of time window cleaning applied more rarely. The *Dynamic Time Window* cleaning, hereafter *DTW* cleaning, removes the association with the trigger time. Instead, the window is chosen to maximize the number of hits. DTW cleaning is generally chosen with a significantly tighter window, often consisting of only a few hundred nanoseconds compared to the multiple microseconds used in the STW cleaning. Time window cleaning is typically used in combination with additional cleaning methods, resulting in little loss in useful signal due to the wide time window (in STW cleaning) or in a very pure set of hits likely to be due to unscattered light.

#### 4.4.3 The DeepCoreFilter

Triggers are generally designed to be as accepting of the proposed physics signal as possible, regardless of the background rates. Typically, limitations exist solely in the processing and storage capabilities in order to prevent the unintentional loss of valuable information. After triggering, various filters may be applied with the sole purpose of removing the collected background. For the purposes of this document, the only filter considered is the *DeepCoreFilter*.

The DeepCoreFilter proceeds by splitting the pulses identified by the SeededRT cleaning into "veto" and "fiducial" pulses, with each DOM given a designation based on its position in the detector. The average and standard deviation in time are first calculated for the fiducial pulses.

$$\begin{aligned}
 & \bar{t}', \sigma_{t'} = 0 \\
 & \text{For DOM } i \text{ in } [1 \dots N_{\text{hits}}] : \\
 & \quad \bar{t}'_i = \bar{t}'_{i-1} + \frac{t_i - \bar{t}'_{i-1}}{i} \\
 & \quad \sigma_{t'_i}^2 = \sigma_{t'_{i-1}}^2 + (i-1) \frac{(t_i - \bar{t}'_{i-1})^2}{i} \\
 & \quad \bar{t}' = \bar{t}'_{N_{\text{hits}}} \\
 & \quad \sigma_{t'}^2 = \sigma_{t'_{N_{\text{hits}}}}^2
 \end{aligned} \tag{4.1}$$

All hit DOMs with the first pulse occurring more than one standard deviation away from the mean time are removed from the fiducial pulse series. With the updated fiducial pulse series, a center of gravity, or *CoG*, of the remaining DOMs is calculated.

$$\vec{x}_{\text{CoG}} = \frac{\sum_i^{\text{DOMs}} \vec{x}_i}{N_{\text{hits}}} \tag{4.2}$$

An average time is calculated by assuming that all pulses are caused by light emission at the CoG, as would be the case for a cascade-like event.

$$t_{\text{CoG}} = \frac{\sum_i^{\text{DOMs}} t_i^0 - \frac{\vec{x}_i - \vec{x}_{\text{CoG}}}{c_{\text{ice}}}}{N_{\text{hits}}} \tag{4.3}$$

where  $t_i^0$  denotes the time of the first observed pulse. The standard deviation of this time is then calculated using the fiducial pulses.

$$\sigma_{t_{\text{CoG}}}^2 = \sum_i^{\text{DOMs}} \tag{4.4}$$

# Updates to the Noise Simulation

5

## 5.1 A Summary of Previous Fits

Detector noise is a nuisance in most physics and astronomy experiments. In general, detector noise for PMTs is assumed to be due to random emission from the photocathode. In this simple model, the noise may be related to the gain and voltage of the PMT, but is independent of external factors. The noise hits appear uniformly in time with a known or measurable average rate following a Poisson process.

This model of the noise was successfully used in the past in IceCube. With the introduction of the lower trigger threshold in DeepCore, however, it quickly became clear that additional sources of noise exist. These additional hits appeared to occur in 'bursts' on a single PMT extending for up to a millisecond. Due to the time-correlations of these hits, the phenomenon was labeled *correlated noise*.

Work done in 2011-2014 ?? showed that the overall noise of the IceCube and DeepCore detectors is well-modeled using a combination of correlated and uncorrelated noise. The empirical model, consisting of a Poisson process for electronic noise and a Poisson process-triggered correlated component modeled with a log-normal distribution, contains five free parameters per DOM fit to each DOM using untriggered raw data from the detector collected over a span of approximately 10 minutes.

The 2014 calibrations were fit DOM-by-DOM by minimizing the chi-squared between the untriggered data and simulation produced with parameters identified using a Metropolis-Hastings algorithm. A distribution of the time between observed hits was used for this fit. Due to the computationally-intensive nature of the fits, the stopping condition was intentionally loosely defined, with a goodness-of-fit of approximately 10% used for most DOMs.

The resulting distributions of the number of hit DOMs and the number of accidental triggers due to detector noise were shown to improve significantly after inclusion of the updated noise model. Analyses at final level reported a significant improvement in fits and a reduction in previously-observed unphysical behavior in fits. The change in the noise model resulted in a change in the rate of neutrinos at final level of up to 50% for a standard oscillation selection in DeepCore and general improvements in agreement between data and simulation rates of other low energy analyses.

## 5.2 Limitations and Disagreement with Previous Fits

While the rate and shape of the accidental triggers improved significantly compared to past attempts, significant disagreement remained. In particular, the number of triggered events with very few hits (here defined as five or fewer hit DOMs) was shown to still be approximately a factor of two higher in data than in simulation. This region of the parameter space was shown to be dominated by accidental noise triggers in simulation. The rates of accidental triggers, as an emergent property of the collection of individual PMTs, contains unknown uncertainties due to the individual uncertainties associated with the noise modeling of each PMT separately. A rescaling of the simulated accidental rates, while difficult to justify a priori without changing the noise rate themselves, proved to be effective in some distributions. In particular, the number of hit DOMs was well-modeled with this approach, resulting in an overall rate agreement of better than 95%.

An evaluation of the limitations of the previous calibration was begun in 2014, uncovering a number of possible improvements.

The original fits were limited due to a number of factors. For example, the fits excluded the effect of atmospheric muons in the detector under the assumption that the approximate hit rate per DOM due to atmospheric muons (approximately 5 Hz) is significantly smaller than the noise hit rate observed in previous calibration (about 600 Hz).

Furthermore, the choice of minimization methods was known to result in potentially-incomplete minimization due to computational limitations. Due to the nature of the fit distributions, there existed significant degeneracy in the parameter space, leading to further difficulties.

In addition, disagreements over the modeling of PMT effects such as afterpulsing led to fits artificially limited to timescales longer than 10 microseconds, allowing the minimizer to only observe part of the correlated noise distribution.

Full waveforms are only recorded from the detector in the case of HLC hits. Because these are rare for noise hits, negligible information was available for fitting at timescales shorter than the FADC readout time of 6.4 microseconds. The noise model itself was used down to 2 microseconds, however, resulting in uncertainty due to the extrapolation of the noise model to shorter times. The limit of 2 microseconds was implemented due to the inherent difficulty in characterizing effects at these timescales due to artificial deadtime related to the HLC launch readout.

## 5.3 Low-dt Noise from Vuvuzela

In an attempt to address the arbitrary limit imposed, a new version of the Vuvuzela code was created with the ability to remove the cutoff. The resulting noise, labeled *low-dt* noise for the short timescales ( $\Delta t$ ), was used to produce a simulation of accidental noise triggers for testing without further calibration. These events were used with standard CORSIKA simulation to test the effect of the low-dt noise on low level variable distributions.

The low-dt noise was shown to increase the rate of accidental triggers, leading to better agreement in data and simulation rates. The distribution of the number of locally-coincident DOMs improved, primarily due to the increased rate of accidental triggers.

The distribution of the total charge of events was tested for both HLC hits alone and for all hits. The charge distribution for HLC hits slightly improved. However, the charge expected from simulation and data showed significant disagreements using the low-dt noise when looking at the HLC+SLC hit distribution.

This disagreement implied that the number of SLC hits was increased significantly with the additional low-dt noise. This demonstrated that the noise distribution at very short timescales was an important effect that deserved further attention.

When the noise distribution is extended to shorter timescales, a fraction of the tail of the distribution falls into a single ATWD window of 322 nanoseconds. Furthermore, some fraction of the hits in a burst of correlated noise occur within the three bins read out of the FADC for an SLC hit. With multiple noise hits occurring in such a short time, the DOM will observe a higher voltage in each of the SLC bins. The result is that SLC hits due to noise no longer occur as single-photoelectron pulses, as is the case when noise hits are rare at the 10 nanosecond timescales, but as an integration of multiple single pulses. The observation of higher charge in SLC pulses in simulation than data gives one an indication of the extremely short timescale end of the noise timing distribution. Alternatively, the charge distribution of each DOM may therefore be used in the fitting procedure in order to characterize the low-dt end of the noise timing distribution. This

provides a direct handle missing from the previous fit, removing some degeneracy that previously existed.

## 5.4 Updating the Fitting Code

The newly available information provided the potential for improvement in the noise fit distribution as well as a way to remove the arbitrary cutoffs used in the previous version of Vuvuzela.

With the opportunity to refit, a number of additional improvements were implemented. In order to include the effect of atmospheric muons, a collection of long-frame CORSIKA was produced. The simulation was halted after photon propagation, giving a collection of muons without detector noise and effects yet applied.

A simulation script was produced to apply the noise, PMT, and DOM simulation for a single DOM using a given set of noise parameters to this long-frame CORSIKA. Information on the timing and charge of the DOM is put into a ROOT file format to ease plotting and fitting. The simulation code was wrapped inside of a calling function, simplifying usage inside of the minimization process.

After the simulation for a given set of parameters, histograms are produced for untriggered data and simulation. As in the previous fits, the time between subsequent hits is used as one of the histograms for calibration of the noise behavior. In addition, the observed charge on the DOM is also histogrammed for use as a second observable.

The range of the histograms, from 6 microseconds until 1 second in the time between hit and 0-5 photoelectrons per DOM launch, provides sensitivity to the full range of the noise distribution.

Using the two distributions, a Poisson binned likelihood is formed using the standard equations. In this case, with the simulation in bin  $i$  of histogram  $j$  denoted by  $f_{ji}$  and the data hits in the same bin denoted by  $d_{ji}$  and ignoring normalization constants, the log-likelihood takes the form

$$LLH = \sum_j \sum_i^{\text{nbins}_j} d_{ji} \log(f_{ji}) + f_{ji} \quad (5.1)$$

For more information on the derivation of the likelihood, see ???. The negative log-likelihood,  $-LLH$  is minimized as a function of the five noise parameters using the iMinuit, a python wrapper for the minuit2 package.

Initial fits showed a lack of constraining power from high charges in the charge distribution. To provide more weight to high charges, the histogram of the charges was weighted by the value of the observed charge. This reduces the weight of very low charge launches, but increases the weight of higher charges.

Additional work showed that the charge distributions between data and simulation demonstrated significant disagreement. A scale factor applied to the charge in simulation was introduced as a free parameter in the fit to account for this. To limit the computational complexity of the added parameter, the minimization over this charge scale factor is done as a separate step in the calculation. This assumes that the difference is a calibration issue in the data rather than a simulation problem. This, in fact, has been shown to be the case, with an updated charge calibration now applied to data at final level. Further information on the charge disagreement between data and simulation can be found in section ??.

The previous calibration attempts explicitly avoided fitting the behavior below 10 microseconds due to the potential for mismodeled PMT effects. In particular, it was noted

that mismodeled afterpulsing behavior could lead to pulls in the noise parameters. The default value in simulation, assumed to be 5.6% for all PMTs, failed to take into account variations in the effects on each individual DOM. In the updated fit, the afterpulsing behavior has been investigated for each PMT by including an overall scale factor on the afterpulsing probability.

Late pulses, produced by electrons which backscatter to previous dynodes during the multiplication process, were also investigated for their effect on the goodness-of-fit in the noise distributions. These pulses occur at timescales of 50-200 nanoseconds and therefore are outside of both the SLC charge and timing distribution window. Regardless, the late pulsing behavior was found to have a small impact due to both the rarity of late pulses as well as the lack of detailed information to constrain the distribution.

The effect of the afterpulsing parameter allowed some fits to fall into a poor local minimum. In those cases, the interplay between the parameters led to a fit that could no longer produce a reasonable fit. In these cases, the probability of observing an afterpulse following a photoelectron would be moved from 5.6% to the unrealistically high value of 20%. This would, in turn, force the mean value for the log-normal timing distribution to move toward higher values and the sigma value to become unrealistically large.

These fits were noticeable when looking at the best fit value of the afterpulsing probability, with a distinct population appearing due to this behavior. In order to constrain the fit to more realistic values, bounds were added to both the log-normal mean and afterpulsing probability.

Due to the computational power required to produce large amounts of effective livetime, a tiered approach was employed in the calibration process. Initial fits were seeded with the previous noise parameter fit values obtained in 2014. For these events, a coarse binning and short effective livetime of just one minute were used. In addition, a weak tolerance value was used, allowing the minimizer to quickly migrate to the neighborhood of the global minimum.

When the first tier completes the minimization process, the fit is begun anew with more effective livetime, more bins, and a stronger tolerance. The second tier used a 5 minute effective livetime.

The third and final tier increased the effective livetime to 10 minutes and again increased the number of bins.

## 5.5 Results of New Noise Fits

New calibration fits were completed over the course of approximately two months for nearly all DOMs in the IceCube detector. String 21 was absent from the updated untriggered data and was therefore left unfit.

The noise fits were checked for correlations between parameters after convergence. One immediately notable feature is the number of DOMs with afterpulsing at the fitter boundary. The likelihood values associated with these fits, however, appear to be consistent with other fits. Due to a planned overhaul of the afterpulsing simulation, the fit values of the afterpulsing probabilities have not been adopted for simulation. Therefore, no further investigation of the probabilities has been pursued.

Some of the noise parameters have expected behavior. In particular, there exists a Poisson process component of the noise model that is assumed to be associated with the electronic noise, which should show increasing rate with increasing depth due to the rising temperature. This effect, though weak, is apparent after the fitting procedure.

Other parameters should be independent of depth. As a test of the fits, each of the other parameters is plotted as a function of depth as well. No significant correlation is observed.

Finally, the likelihood itself should be independent of depth. This final test shows surprising results in at least two ways: a 'band' structure appears in the plot. and there appears to be a depth-dependent decrease in the likelihood value, indicating that the lower part of the detector yields better fit results. This was initially unexpected, given that the noise is an internal property of the DOM and not of the surrounding medium. This effect occurs due to a combination of factors. It is worth noting that the fits are not independent of external factors. Indeed, the fits themselves use the long-frame CORSIKA to model the effects of muons in the untriggered data from the detector.

This leads to two subtle limitations in the fitting process. The long-frame CORSIKA is produced with a single flux model, in this case the model of Hoerandel. Because the long-frame CORSIKA cannot be reweighted to other models, uncertainties or mismodeling in the muon flux can lead to disagreement in the fitting of noise parameters. The muon flux decreases with increasing depth, resulting in a lower muon contamination, and consequently smaller effects from mismodeling of the muon background, for deeper DOMs.

In addition, the long-frame CORSIKA implicitly assumes a single model of the ice for photon propagation. Mismodeling of the scattering and absorption of the ice therefore may also give rise to disagreement in the noise calibration process. While large-scale properties of the ice are believed to be well-reproduced by the chosen ice model, SpiceLea, there will inevitably be remaining disagreements.

The net effect of these two assumptions in the muon simulation is effectively correlated with the convolution of the ice model and the muon flux. In particular, the best fits occur where the DOM is either A) well-shielded from light due to muons by the large depth or B) well-shielded due to large absorption in the ice. In both cases, the contamination from light due to muons in the fitted time and charge distributions will be small, leading to a more 'pure' noise distribution that is well-fit by the assumed model.

The sensitivity of the noise calibration procedure to underlying physics of both the muon flux and the absorption properties in the detector imply that little further improvement is likely without work on one or both issues. Simulation of long-frame CORSIKA is, unfortunately, unlikely to be updated to a newer flux model in the near-term due to technical limitations. As the primary uncertainty affecting the goodness-of-fit appears to be due to the visibility and flux of the muons themselves, merely updating to a newer model of the ice will be unlikely to significantly improve the current fit parameters.

The newly calibrated low-dt Vuvuzela was provided to the IceCube simulation group in January of 2015 and quickly integrated into the low-energy simulation chain. New neutrino, muon, and accidental noise trigger simulations were produced soon thereafter. The updated noise model shows significantly better agreement in both the total charge distribution and the number of hit DOMs for both HLC and SLC+HLC hits. The rate of accidental triggers improved relative to previous calibrations, with the remaining rate disagreement reduced from 50% to approximately 15%. Negligible effect was observed in the low-energy neutrino events at final level for existing samples.

# Low-Energy Muon Simulation

## 6.1 Long-Frame CORSIKA for DeepCore

One of the primary difficulties for low energy analyses in IceCube is the modeling of backgrounds. Two significant backgrounds exist for a standard muon neutrino disappearance measurement: the events due to cosmic-ray induced muons and the events from accidental triggers in the detector due to random detector noise.

The two types of simulation are somewhat interdependent. In particular, the accidental trigger rate, defined to include only events in a trigger is primarily caused by noise hits, relies on the rate of atmospheric muons to calculate an effective livetime for possible noise triggering. In turn, the atmospheric muon triggering and filtering rate depends somewhat on the characteristics of the noise model used in the simulation.

At the lowest energies, the interplay between atmospheric muons and noise becomes more muddled. The falling muon spectrum ensures that there are a significant number of muons that potentially reach the IceCube detector even down to cosmic ray primary energies of approximately 600 GeV, where the overburden from the glacial ice yields a natural cutoff to the spectrum. At these energies, a shift in either the muon rate or the noise rate can change the hit rates at the top of the detector. These low-brightness muons are largely indistinguishable from noise hits, but are not simulated using the Vuvuzela module. Ignoring these muons can result in a systematic mismodeling of the detector background that changes as a function of depth, with the worst agreement at the top of IceCube. These muons, called *sub-threshold muons*, have been shown to be responsible for a significant fraction of hits in the detector [[heereman\\_thesis](#)].

While the 5-component CORSIKA described in ?? generally gives much more freedom to fit and correct for spectral characteristics, the events cannot easily produce the low-energy muon background characteristics at the top of the detector. Instead, the most accurate way to model these effects relies on long-frame simulation described in ?. These frames, consisting of a continuous detector simulation over the course of tens of milliseconds or longer, can be combined with CORSIKA simulation in order to produce the most accurate background simulation possible with current tools.

Long-frame CORSIKA generally requires a modeling of a natural flux of events in the detector. Given the currently available toolset, only the polygonato mode of the CORSIKA generator is therefore able to be used for long-frame generation. While there are currently ideas for how to generate with a more accurate spectral model, they prove to be inefficient without a reparametrization of the generation from the CORSIKA code itself and will not be discussed here.

To produce long-frame CORSIKA simulation, a few modifications of the standard simulation scheme are required. A frame length,  $\tau$  is chosen at the start of simulation. Longer values of  $\tau$  will generally yield more accurate simulation due to issues at the start and end of a frame, although this is a minor concern in practice. With this time, an expected number of particles may be extracted given a spectrum  $\Phi_\mu$  and a simulation volume  $V$ :

$$\bar{N}_\mu = \int_{t=0}^{\tau} \int_E \int_{\Omega} \int_V \Phi_\mu \quad (6.1)$$

This is an analytic formula, yielding the poissonian expectation on the expected number of muons in the simulation volume. A number of muons is then calculated as a poisson-fluctuation of this number. The CORSIKA generator will produce the requested number of muons in this time frame. These muons can be either single muons or occur as muon bundles. In the latter case, the entire bundle is treated as a 'muon' for the purposes of this section.

The muons are evenly distributed throughout the simulation window following the assumption that each muon is independent of all others (ie, that they are not due to the same cosmic ray interaction in the atmosphere). From this point, the long-frame simulation scheme described in ?? continues, with detector simulation and splitting occurring in the CoincidenceAfterProcessing module.

Long-frame CORSIKA simulation is a useful tool for low energy analyses, yielding a collection of accidental trigger events and muons that would otherwise be produced separately and require reweighting. In addition, emergent properties of the subthreshold muons are included in these simulation sets. Unfortunately, the production of long-frame CORSIKA simulation is particularly computationally expensive and of limited use for most higher energy analyses ongoing in the IceCube collaboration. Very little long-frame CORSIKA simulation is therefore available.

For this work, long-frame CORSIKA simulation was created with an effective livetime of approximately two weeks. Such a sample required months of simulation time, severely limiting the potential usefulness for analyses. Still, the existing sets proved useful and necessary for the work in ?. Furthermore, the sets provided the first background estimates for both accidental triggers and atmospheric muons for the PINGU/Phase 1 detector described in ?.

Initial tests with the long-frame CORSIKA simulation showed, for the first time, notable disagreement in the charge distributions in data and simulation described further in ??.

## 6.2 MuonGun for DeepCore

## 6.3 Simulation Efficiency with KDE Filtering

The production of background atmospheric muons is the most computationally expensive part of oscillation analyses in IceCube. For the primary analysis of this thesis, full CORSIKA simulations have proven to be impractical. When simulating at the detector threshold, many of the produced showers lead to no significant contribution to the detector output, leading to significant inefficiency. In addition, the choice of cuts employed (see ??) lead to a low simulation efficiency at final level that has both strong energy and zenith dependences.

For this work, a set of  $3 \times 10^9$  muons were produced using collaboration resources over a period of approximately three months. Muons were produced following the MuonGun scheme described in ??, with all muons aimed toward the DeepCore fiducial volume. The resulting generation-level distributions are shown in ?. The muons follow the offset power law described in ?? in energy and the expected zenith angle spectrum from the underlying flux model of [h4a]. The generated muons show azimuthal symmetry as expected.

After processing to the final level of the GRECO event selection (see ??, the background muon simulation retains approximately 9000 simulated events of the original sample. This remaining subsample may be used to estimate the simulation efficiency of muons in this selection. The efficiency is most easily observed with low energy muons that travel

very downgoing, as seen in ???. These events make up the majority of simulated muons at generation level, but no such events reach the final level of the analysis.

In addition to the energy- and zenith-dependent effects, the GRECO selection exhibits strong azimuthal selection bias. This arises due to two main effects. The first is the offset between the center of IceCube (and therefore the center of the generation volume) at  $(x, y, z) = (0, 0, 0)$  and DeepCore at  $(x, y, z) = (XXXXXXX)$ . This gives rise to an azimuthal effect appearing as a sinusoidal variation of the minimum generated energy of events at final level.

The second is the regular hexagonal structure of the IceCube volume, with long "corridors" through which muons may reach DeepCore without crossing any strings. Cuts designed to look for hits left in the veto region produce these azimuthal biases when muons close to strings (ie, outside of the "corridors") are more likely to be identified and removed than those further from strings (inside of the "corridors").

In order to improve simulation statistics at final level, the existing MuonGun simulation scheme was modified to include an energy-, zenith-, and azimuthally-dependent prescale factor. This approach, here entitled *KDE Filtering*, allows simulation to be produced with a known bias matching that of a given set of input files.

In this scheme, the *kernal density estimator (KDE)* from SciPy [88] is applied to all remaining events at final level of the GRECO event selection. The KDE uses a Gaussian kernal to represent each event in energy, zenith, and azimuth. The resulting KDE is normalized to produce an approximation of the final selection probability density function. In the new simulation scheme, an event is produced using standard settings for MuonGun generation. Immediately following generation, the probability of the new event reaching final level is calculated from the KDE, with typical values of approximately  $10^{-4}$  for a likely event and  $10^{-9}$  or lower for unlikely events. A prescale multiplicative factor of  $10^5$  is used to set the overall probability scale. The product,  $p$  of the prescale factor and KDE-derived probability may not exceed 100% and any values for which this may be the case are directly set to 100%.

Using a random number generator, this  $p$  factor is used to retain or reject the muon event. The simulation then proceeds as normal, with photon propagation, detector simulation, triggering, and filtering.

When events need to be weighted by a flux model, the  $p$  factor must be included as well. The modification to the weighting scheme requires the use of the original MuonGun weighting code in the usual scheme. The total weight is then scaled by  $\frac{1}{p}$ , which corrects the rates and uncertainties for the simulated events.

By removing unlikely events early in the simulation chain, the required computational resources are significantly reduced. In addition, the updated simulation scheme gives the opportunity, for the first time, to study various detector systematics affecting the atmospheric muons at the final level of oscillation analyses.

By way of comparison, the total amount of time required to produce 9000 events at final level of the GRECO selection with similar available resources reduces from three months under the standard scheme to approximately four days using the KDE filtering method.

# GRECO: An Event Selection at the Limits of DeepCore

## 7.1 Low-En Level 3 Cuts

### 7.1.1 GRECO Level 4 Cuts

The first GRECO-specific cut level, designated *level 4*, or *L4*, was first introduced in 2011 using variables common to higher energy cascade analyses within IceCube.

At the start of this series of cuts is requirement of at least three hit DOMs in the hit series associated with an event. This is an extremely loose cut, required solely for the successful processing of other cuts.

The remaining cuts at L4 can be divided into two groups: those that rely on a rough reconstruction of the event and those that are based solely on charge deposition.

#### FirstHit Z

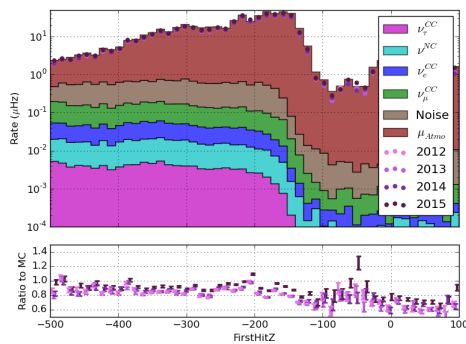


**Figure 7.1** – The Z position of the first hit in a cleaned hit series. Note the shape difference between the atmospheric muons in red and the various neutrino flavors, particularly above -200 meters.

Muons generated in the upper atmosphere through cosmic ray air showers will generally be visible as they enter the detector. As they pass through the veto layers, the muons may emit light via Cherenkov emission or via stochastic processes. This light leaves a signature behind in the detector in the form of hits along the true muon track.

Because the muon tracks are primarily steeply inclined, most will leave hits in the upper part of the detector. Neutrinos, on the other hand, will emit light following an interaction. For the low-energy neutrinos of interest to this analysis, interactions will occur primarily in the DeepCore fiducial region, leading to little or no light emission in the top half of the detector. This difference between neutrino and muon emission in the upper part of the detector can be used to identify background muons with little additional processing. For this analysis, the first hit in a cleaned hit series, the time-window cleaned DeepCore pulses, is called the *FirstHit Z* in the Level 4 cuts.

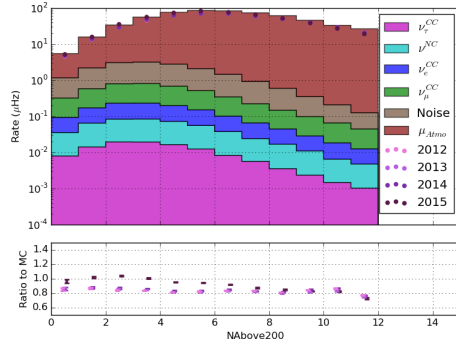


**Figure 7.2** – The number of hits above  $Z = -200$  meters

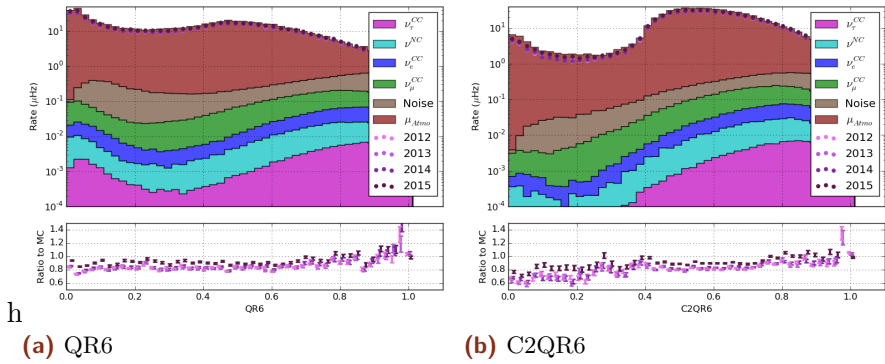


**Figure 7.3** – The charge ratio variables used in the L4 cuts.

## NAbove200

The position of the first hit in DeepCore is not the only low-level cut to arise from the emissions of the muon and neutrinos. The total charge of recorded hits occurring in the top of the detector is also used in the analysis. This variable, known as  $NAbove200$ , counts the amount of charge occurring before the SMT3 trigger above a depth of -200 meters.

## QR6/C2QR6

After a particle interacts, the light emission as a function of time will depend on the type of particle emitting. A very basic model of cascade-like events assumes that photons are emitted roughly instantaneously from a point-like source at the interaction vertex. The photons then travel outward according to a random walk with absorption, leading to a decay in the observed number of photons over time. A muon, however, acts as an extended source and will emit at multiple points along the muon track until it either falls below the Cherenkov threshold or is stopped.

The light emission is, therefore, more likely to be "peaked" in time for neutrinos than for muons. Using this information, two variables are designed to search for this peakedness in the light detection over time.

The first of these, the *charge-ratio within 600 ns* (hereafter  $QR6$ ), is the ratio of the charge occurring within 600 ns of the first hit compared to the total charge of the event. The value of 600 ns was chosen in a previous analysis and is not re-optimized here.

Regardless, this time corresponds to roughly two ATWD time windows or approximately 180 meters at the speed of light in vacuum. This distance, which will correspond to a wide swath of the DeepCore fiducial volume, provides some separation between muons and neutrinos.

## QR6 plot

Neutrinos and muons do not produce the only hits observed in the detector, however. Random detector noise, in particular, can significantly change the choice of time used. In order to check the effect of random noise contributing the first few hits of the event, a second variable, known as *C2QR6*, is introduced. This variable is calculated in an identical way to QR6, but the first two observed hits are ignored.

*C2QR6 plot*

## Tensor of Inertia

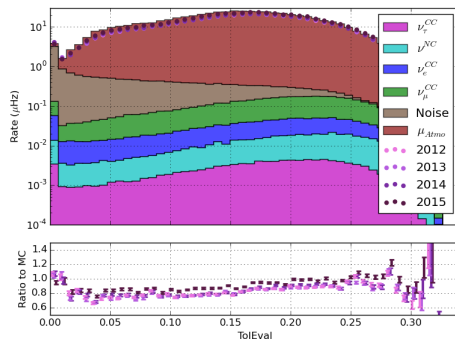


**Figure 7.4** – The eigenvalue ratio from a ToI calculation. Larger values indicate more apparent elongation in the event.

At this early level, the shape difference in the observed hit pattern will be relatively clear. Neutrinos with energies in the range of 1-100 GeV will appear to be rather small and compact, while muons will have a longer extent in one direction along the muon track than perpendicular to it. In order to utilize the shape differences between these two types of particles, the *Tensor of Inertia eigenvalue ratio* (more briefly, *ToI*) is used. This variable is defined in a similar way to the tensor of inertia from mechanics, with the measured charge taking the place of the mass.

$$I_X = \sum_{i=0}^{nhits} (y_i^2 + z_i^2) q_i I_Y = \sum_{i=0}^{nhits} (x_i^2 + z_i^2) q_i I_Z = \sum_{i=0}^{nhits} (x_i^2 + y_i^2) q_i \quad (7.1)$$

These three moments yield information about the shape of the event. The eigenvalue ratio is defined as

$$e = \frac{\max_j(I_j)}{I_x + I_y + I_z} \quad (7.2)$$

## Improved Linefit Speed

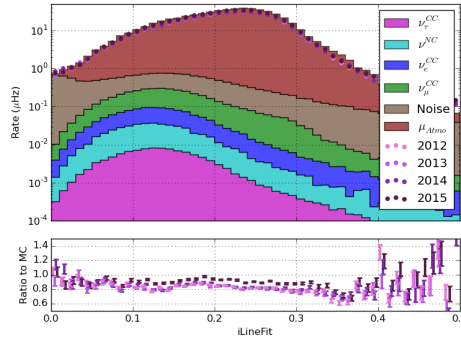


**Figure 7.5** – The apparent speed, in units of meters per nanosecond, corresponding to the hits in the event. Faster speeds are associated with particle travel instead of light travel.

## The L4 BDT

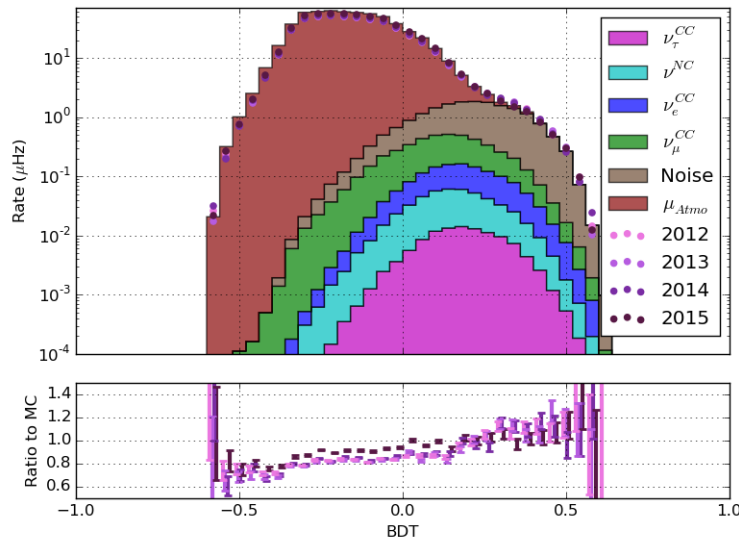


**Figure 7.6** – The distribution of the boosted decision tree used at L4. A cut is applied at 0.04 to remove a significant fraction of atmospheric muon background events. Note the ratio, which shows disagreement in the very muon-like region. The region of disagreement is removed by the cut.

A Boosted Decision Tree (*BDT*) is trained at L4 to further reduce the atmospheric muon background by a factor of 10x.

The variables described above were provided to a BDT training using the CORSIKA 7437 and IceSim3 GENIE simulation.

Burn sample distributions match in the years 2012/3/4/5, but are notably different for 2011. I believe the reason is related to the deployment: once new DOMs are deployed, they take 1-2 years to completely cool down 2011 is therefore excluded for this analysis. Comparisons to MC show mild disagreement, particularly in the most muon-like regions that get cut away. Its not obvious what is the cause of the disagreement, although its possible that the assumed cosmic ray flux model (H4a) is simply an inaccurate model of some part of the spectrum that contributes. This may be particularly true, since H3a and H4a contain different compositions at high energies. These differences would contribute

to different parts of the atmospheric muon spectrum at the detector, where the highest energy atmospheric interactions leading to visible muons will occur at the horizon. If these (or other systematics on the CR/muon spectra) give rise to different HE muon distributions, those muons would appear to have clear tracks and would show up on the far left of the BDT distribution.

In the right side of the plot, a shoulder attributable to the noise triggers is visible. While this is initially surprising, the reason for this is obvious: the BDT was originally trained with CORSIKA set 7437 and weighted GENIE sets. Both cases had incorrect modeling of the detector. Both had DOM oversizing applied and DOM efficiency set to 0.9 (the old nominal value) instead of the 0.99 that we now use. The training itself lacked any pure noise triggers as a reference, and so the BDT picked the most obvious feature of the GENIE sets: that the signal events were primarily low energy with lower light deposition than the background. These are also key features of the noise triggers.

### 7.1.2 GRECO Level 5 Cuts

The next stage of cuts, known as the *GRECO Level 5*, or more simply, *L5*, is structured in a similar manner. Once again, there exists both a relatively simple cut dedicated to removing accidental triggers due to noise as well as a BDT consisting of six variables.

#### L5 Straight Cuts

The former is again a cut on the number of hits similar to the cleaning applied in the L3 cuts. This time, however, a slightly different cleaning is applied, consisting of both a static and a dynamic time window applied to the split DeepCore pulses. The static window, with a width of 7500 nanoseconds, removes hits that are far from the trigger in order to limit the effect of random detector noise. The dynamic time window is designed to specifically look for a set of hits spaced very closely in time. For the L5 noise trigger cut, a dynamic window is chosen of 200 nanoseconds.

After the two time window cleaning algorithms are applied, the resulting hit series is required to possess at least 3 remaining hits to be accepted for further processing.

#### Time to 75% Charge

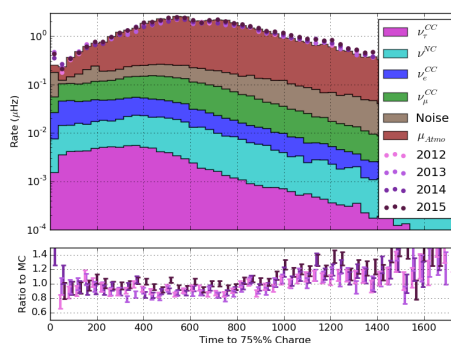


**Figure 7.7** – The time to accumulate 75% of the total charge of the event.

The first variable used to create the L5 BDT is the amount of time to accumulate 75% of the total charge, the  $t_{75}$ . The idea behind this variable is again similar to that of the QR6 and C2QR6 variables and will not be repeated here. However, the variable is now produced in the reverse manner: where the QR6 variable refers to the amount of a charge

in a given window, the  $t_{75}$  instead attempts to find the amount of time for a given charge level, providing an additional handle on the total event length and timing distribution.

## Veto Identified Causal Hits

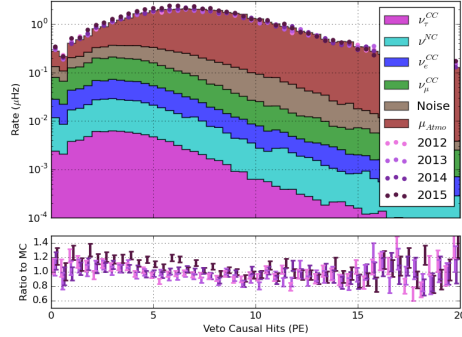


**Figure 7.8** – The amount of causally-connected charge discovered in the veto region.

The *Veto Identified Causal Hits* (*VICH*) algorithm is a second choice for the L5 cuts that relies solely on low-level charge information. In this case, we improve on causality constraints using the trigger time and the position of the first DOM to contribute to the trigger. The time and distance are calculated to each other hit relative to this simplistic event vertex. Any hits that occur in a window before the trigger that are approximately causally connected to this hit are recorded, with the total charge thus recorded giving the cut variable. The window is described in ??

## First Hit $\rho$

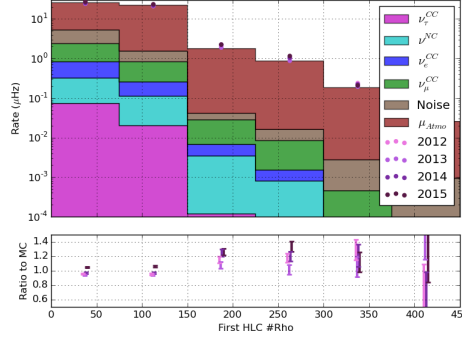


**Figure 7.9** – The radial position of the earliest hit of a cleaned hit series. The radial position is measured relative to string 36, the center of DeepCore.

Further simple event vertices give additional separation power. In particular, the radial position of the first hit in a STW cleaned (7500 ns) hit series encompassing solely the DeepCore fiducial volume may be used to identify incoming atmospheric muon events.

## Quartiles CoG

The traveling distance of a muon may be exploited in order to identify muons as well. In particular, a track-like event is expected to travel over a longer distance than a

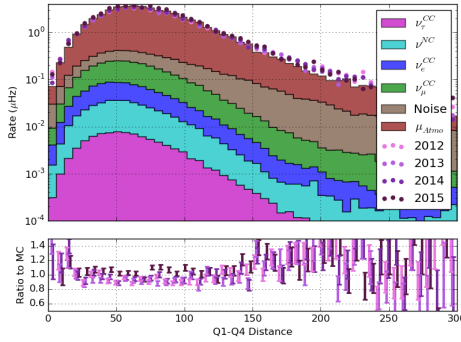


**Figure 7.10** – The distance between the centers of gravity of the first and last quartile in time.

cascade-like event of a similar energy. Looking at the first and last quartiles in charge, the length of the vector from one of the CoGs to the other can give some simple indication of the length of a hypothetical track in the event.

## Z-Travel

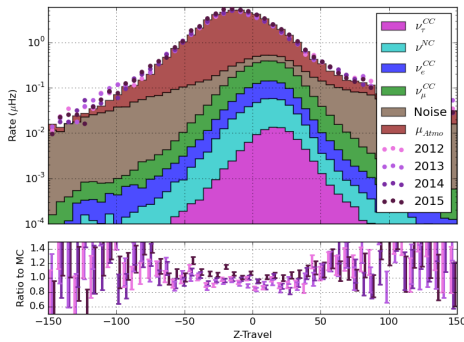


**Figure 7.11** – The distance traveled in Z between the first and last quartile of hits in time.

Atmospheric muons are primarily a downgoing feature of the detector, with a flux that approaches zero at the horizon. Muons will, therefore, leave some information in the depth and directional information collected by the detector. The first variable to utilize this, *Z-Travel*, identifies the distance in the z-direction between the first and the last quartile of hits using the CoGs calculated in the previous variable.

## SPE Zenith

More advanced reconstructions are viable at this level, providing new potential for the identification of atmospheric muons from neutrino candidates. Using the first pulse on each DOM, a likelihood reconstruction may be produced. A fast likelihood reconstruction assuming an infinite track passing through the detector with light scattered via the Pandel scattering model of ice is one such tool.

The Pandel model of scattering, while known to be inaccurate, provides an analytic form that is fast to evaluate in order to find the charge expectation as a function of relative position and direction between the hypothesized track and each DOM. The reconstruction begins with a seed of some description that my slightly gin-addled mind with no internet access cannot recall. A total of eleven directions are used as seeds around the

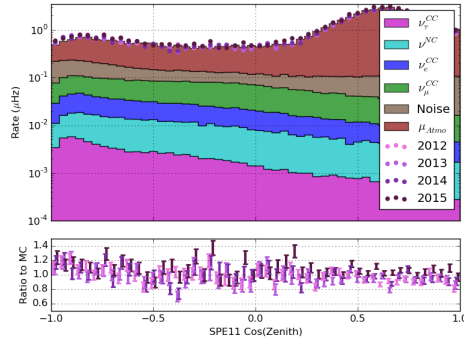


**Figure 7.12** – The zenith angle distribution of events from an 11-iteration SPE fit. The fit assumes an infinite track hypothesis and uses only hit DOMs.

seeded position and time, including a seeded direction. For each hypothesis, the expected charge at different time steps is compared to the observed charge at each DOM using a Poisson binned likelihood. The best-fit of the eleven reconstructions is returned.

Again, atmospheric muons are primarily downgoing events. Therefore the direction of the reconstructed track is a useful tool for separating neutrino signal and atmospheric muon background.

### The L5 BDT

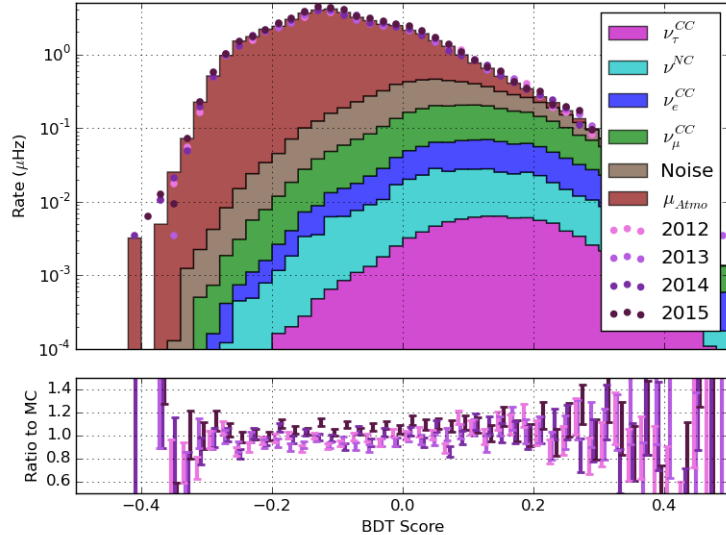


**Figure 7.13** – The distribution of the boosted decision tree used at L5. A cut is again applied at 0.04 to remove a significant fraction of atmospheric muon background events.

The six variables described in this section are again used to create a BDT. At the time of training, updated versions of both the GENIE and CORSIKA simulations were provided as part of an ongoing upgrade of the IceCube simulation. In particular, the L5 BDT was trained using simulation files containing the then-newly available Vuvuzela noise model and an updated version of the GENIE Monte Carlo generator.

A set of fifteen variables were tested. At each step of the training, the least important variable was removed to limit the possible effects of overtraining. The process continued

until changes in the cut efficiency larger than 1% were observed, resulting in a boost decision tree containing the six most important variables tested as described above.

The distribution of BDT score is shown in ???. The data and simulation show good agreement across the range of scores. In addition, the distribution of shows some separation from the neutrino events, providing some cut power.

A cut is placed at a score of 0.04, which gives approximately 95% background rejection with a somewhat significant hit of 30% to all neutrino rates.

### 7.1.3 GRECO Level 6 Cuts

Unlike previous levels, the GRECO L6 does not rely on a trained boosted decision tree. The choice was made to use solely straight cuts due to initial concerns about the significantly limited background simulation. Such a limitation could lead to overtraining, a situation difficult to test with so few simulated events.

Instead, there are effectively two types of cuts used in the GRECO L6: those that deal, directly or indirectly, with removing accidental triggers and those that focus on the starting containment of events in the DeepCore fiducial volume.

#### Fill-Ratio at L6

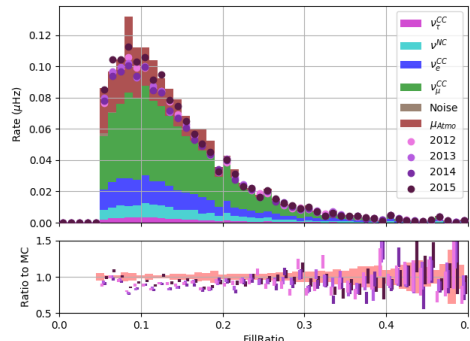


**Figure 7.14** – The fill-ratio distribution. Note the excess of noise triggers at low values. A cut is applied at 0.05 to remove these accidental triggers.

A continuing thread of the event selection deals with understanding and removing events caused by detector noise triggering in the DeepCore fiducial volume. While the rate of these accidental triggers is low at this stage relative to the rate at L3, they form an important background to the remaining set of neutrino events. In order to limit their effect, various cuts were investigated for the potential to separate signal neutrinos from the accidental background.

The most promising cut was discovered to be a remnant of earlier AMANDA processing efforts at separating atmospheric muon background and cascade signal events. This cut, called *Fill-Ratio*, looks at the topology and compactness of hits within an event.

Fill-Ratio requires a reconstructed vertex and pulse series. In the case of the GRECO L6, the first hit position in DeepCore within a 7.5 microsecond STW cleaned pulse series is used as an approximate event vertex. The hit series chosen, TWSRTOfflinePulses, offers some cleaning as well.

Once a vertex and pulse series are provided, a radius is computed. Many options are available for the calculation of different radii, although the most effective for this event selection is the mean distance from the vertex.

$$\bar{r}_{Fill-Ratio} = A \left| \frac{\sum_i^{npulses} (\vec{x}_i - \vec{x}_{vertex})}{npulses} \right| \quad (7.3)$$

where  $A$  is a configurable scale factor. Within this radius, the algorithm identifies all contained DOMs. The cut value is then given by the ratio of contained DOMs observing a pulse to the total number of contained DOMs.

$$f = \frac{\sum_i^{ncont} (|\vec{r}_i| < \bar{r}_{Fill-Ratio} \& Q_i > 0)}{\sum_j^{ncont} (|\vec{r}_j| < \bar{r}_{Fill-Ratio})} \quad (7.4)$$

This effectively results in a measure of the compactness of a hypothetical cascade, where we expect the resulting hit distribution to be approximately spherically symmetric. In the case of an extended track, this parameter will yield a larger value of  $\bar{r}_{Fill-Ratio}$ . The larger value, in turn, will result in a higher number of contained DOMs and, therefore, a lower value of this parameter. This is particularly true in the case of accidental triggers, where we have no reason to expect a compact hit distribution a priori. Using a loose choice of  $A$  of 1.6, we concentrate the accidental triggers in just a few bins close to  $f=0$ . The observed separation at a value of 0.05 allows up to one order of magnitude of reduction in the rate of accidental triggers with a relatively small reduction in signal rate of approximately 10%.

## The L6 NChannel Cut

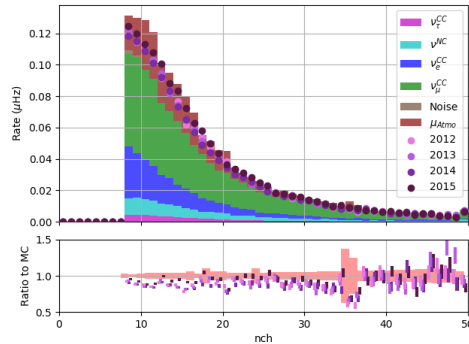


**Figure 7.15** – The number of channels in a cleaned hit series. At least 8 hits are required for the reconstruction.

The reconstruction chosen for the final stages of this event selection attempt to reconstruct a total of eight variables: the position ( $x, y, z$ ), time ( $t$ ), the direction ( $\theta, \phi$ ), the energy deposited in the proposed hadronic cascade ( $E_{casc}$ ), and the track length ( $L$ ). The reconstruction, described in more detail in ??, uses information both from the hit DOMs as well as unhit DOMs in order to constrain the reconstructed parameters. In order to constrain all parameters using observed hits, as opposed to relying on information from unhit DOMs, the decision was made to process only DOMs possessing more than 8 hits in the SRTTWOOfflinePulsesDC pulse series.

In addition to providing a more robust reconstruction, the additional cut on the required number of hits further reduces the expected rate of accidental triggers in the detector by

another order of magnitude. These accidental triggers make up about 0.3% of events in the sample following these cuts.

## CorridorCut

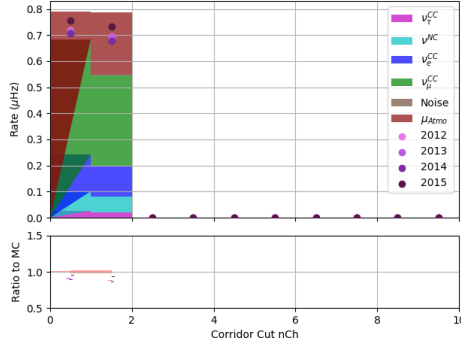


**Figure 7.16** – The number of channels discovered along one of the various "corridors" in the detector. Events with at least two hits discovered along a corridor are removed.

At later cut levels, atmospheric muons continue to be problematic. Unfortunately muons at this level tend to be difficult to identify muons based on many parameters. Indeed, any muons that were easily identifiable have been removed already by this stage of the selection.

In the past, minimum-ionizing muons were discovered to be leaking into the DeepCore fiducial volume along *corridors*, lines connecting the inner part of the detector to the outer edge without crossing any strings. These events pass between strings and leave little trace in the form of coincident hits in the outer detector.

In order to identify these muons, a cut was developed to look specifically along these pre-defined corridors for hits potentially correlated with pulses in DeepCore. Due to the effects of random detector noise, a cut limiting the number of discovered corridor hits to 0 would result in a significant loss of signal events. Instead, one hit is allowed, with two or more discovered DOMs leading to the removal of the event from further processing. At this stage, there are few events due to atmospheric muons with detectable energy in the veto, resulting in the removal of very few events.

## FiniteReco Starting Containment

The SPE reconstruction used in L5 was created using an infinite muon hypothesis. In order to refine this reconstruction, the *FiniteReco* algorithm is employed.

FiniteReco is a module that accepts a previous reconstruction and a given set of pulses. The pulses are then used in a likelihood reconstruction in order to obtain estimates for the starting and stoppoing positions as well as the starting time for the given muon track. The direction of the muon track remains unchanged.

The starting position of the resulting reconstructed particle may be used to estimate the interaction point of the particle. ?? shows the position of the reconstructed vertex in terms of depth and distance from the center of the volume. If an event begins outside of the DeepCore fiducial volume, particularly if the event appears at the top of the fiducial volume, the event is likely to contain a muon and can be removed from the sample. Cuts are applied at the positions shown, resulting in a significant reduction in the number of muon events expected at final level.

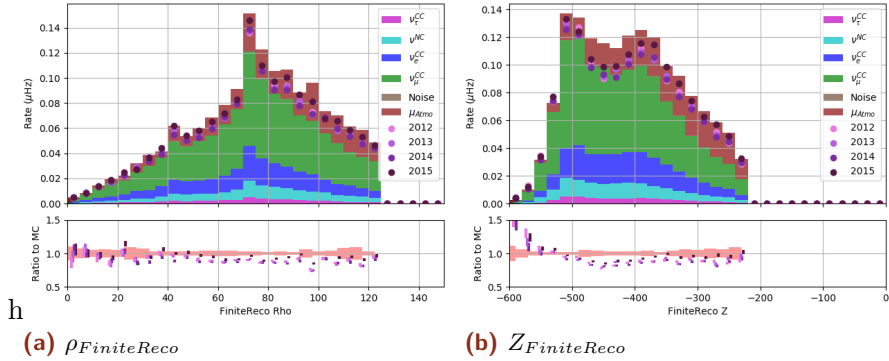


**Figure 7.17** – The FiniteReco containment cuts. Note the excess of muons at the top and outer edge of the DeepCore fiducial volume.

### 7.1.4 GRECO Level 7: Final Level Reconstruction using PegLeg

The existing reconstructions up to this point use either analytic or simplified likelihood reconstructions to estimate particle parameters. The position of the first hit and the finite muon reconstruction from FiniteReco provide straightforward separation power between atmospheric muons and neutrino events, but are designed to be computationally inexpensive instead of precise. At final level, these estimates are refined using a novel reconstruction method developed specifically for low-energy and oscillation searches with DeepCore.

The *PegLeg* reconstruction, developed by Martin Leuermann based, in part, on earlier work by Matt Dunkmann, is a low-energy reconstruction that uses a hybrid cascade+muon hypothesis. The reconstruction returns a total of eight parameters: the position ( $x_R$ ,  $y_R$ ,  $z_R$ ), time ( $t_R$ ), direction ( $\theta$ ,  $\phi$ ), total energy ( $E_R$ ) and track length ( $L_R$ ). The algorithm requires both seeds for each of the particle parameters, a collection of hits over which to run, and a set of splines fit to an ice model.

For each particle hypothesis, the event is broken into steps in time based on the timing of the observed hits in the event. At each time step, the expected charge at each DOM is calculated based on the energy and position of the particle emission scaled using the ice model splines. The charge expectation is evaluated for all DOMs, regardless of whether a hit is observed or not. The total likelihood of the hypothesis is then the product of the likelihoods at each DOM.

The likelihood space itself typically possesses multiple local minima due to the small number of hits. The fit is performed using the MultiNest minimizer package in order to handle the complex likelihood space.

Given the large dimensionality of the space, significant computational power is required for the fit. Various steps are used in order to reduce the resource requirements. Track lengths are limited to integer values that depend on parameters used to produce the spline tables. While this requirement is lifted in newer versions of the software, that change has not yet propagated to the current GRECO events. In addition, only DOMs within 150 meters of the current particle position are evaluated to find the expected charge. All other DOMs are assumed to have an expected charge consistent with noise

multinest

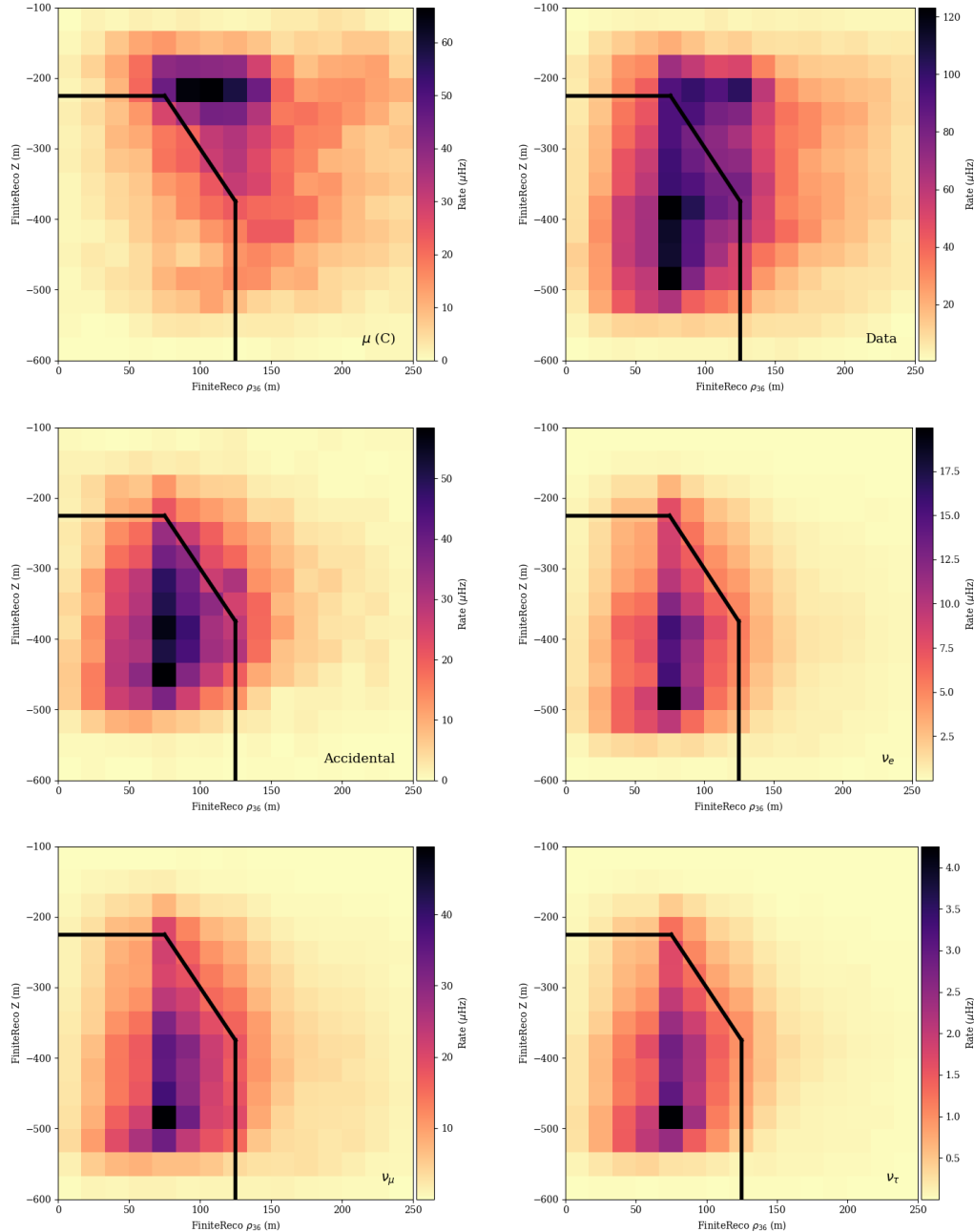


**Table 7.1** – The FiniteReco containment cut for each of the channels. The cut itself is shown with the black line.

martin's thesis  
millipede paper  
martin's thesis

rates. This assumption allows the minimizer to avoid costly calculations of expected charge for distant DOMs at the expense of higher energy event resolutions.

In early versions of the PegLeg fit, the charge of individual pulses is used directly in the likelihood calculations . Following the discoveries discussed in ??, however, the handling of the charge was changed . In the version of PegLeg used in the final version of this analysis, a deadtime window of 45 nanoseconds is introduced for each DOM directly following a pulse. During this window, the DOM may not contribute any further information to the fit, instead simply being labeled as "active". This changes the reconstruction likelihood from being charge-based to being hit-based. Using this modification, disagreements between the data and simulated pulses may be minimized.

Each event takes approximately 15 minutes on average to converge in the reconstruction. There also exists a significant tail to the reconstruction time, sometimes extending to multiple hours for a single event. With a large expected sample of events, the reconstruction time is the most computationally intensive part of the event selection

## Containment with PegLeg

With a more refined reconstruction, additional constraints on the containment of the starting vertices are possible. Similar to the work done with FiniteReco at L6, the  $Z_R$  and  $\rho_R$  receive cuts in two dimensions as shown in ???. Once again, events at the top of and near the edge of DeepCore are more likely to be muons. An additional cut is applied at the bottom of the detector in order to limit the effect of observed discrepancies data and Monte Carlo. Removing these events results in a 75% reduction of the atmospheric muon background at a cost of approximately 10% of the overall neutrino rate.

## Other Cuts at L7

In the course of further work on the event selection, a number of issues previously-unknown were discovered. The most important of these, discussed further in ??, is the discovery of flaring DOMs, where a DOM spontaneously emits light. Because the light is emitted from the DOM itself, these events are characterized by high light yield on a single DOM relative to the rest of the event. These events were first discovered with the GRECO sample and are under further investigation within the IceCube collaboration. Two DOMs are known to emit light in this way at a rate of approximately once per day, although more are under investigation as of the time of this writing.

The two known DOMs are removed from the reconstruction pending further investigation. In addition, any event event with a single DOM observing more than 80% of the total charge is removed to remove events with this characteristic signature.

Cuts are also applied to the average reconstructed energy per hit DOM (??) and the scatter in the timing distribution of hits (??). The former is expected to yields high values for events dominated by flaring DOMs or events where a particle interaction occurs very close to the face of a DOM. The distribution also shows some disagreement at low values, however. The reason for this is likely related to the issues discovered in ??, although this disagreement has not been investigated further. A cut removing events with more than 3 GeV/DOM is applied only to events with fewer than 14 hits, limiting the impact on the neutrino signal events.

The scatter in the hit times shows very good agreement between data and simulation and is useful as a proxy for the overall scattering of the event. The cut, which removes events

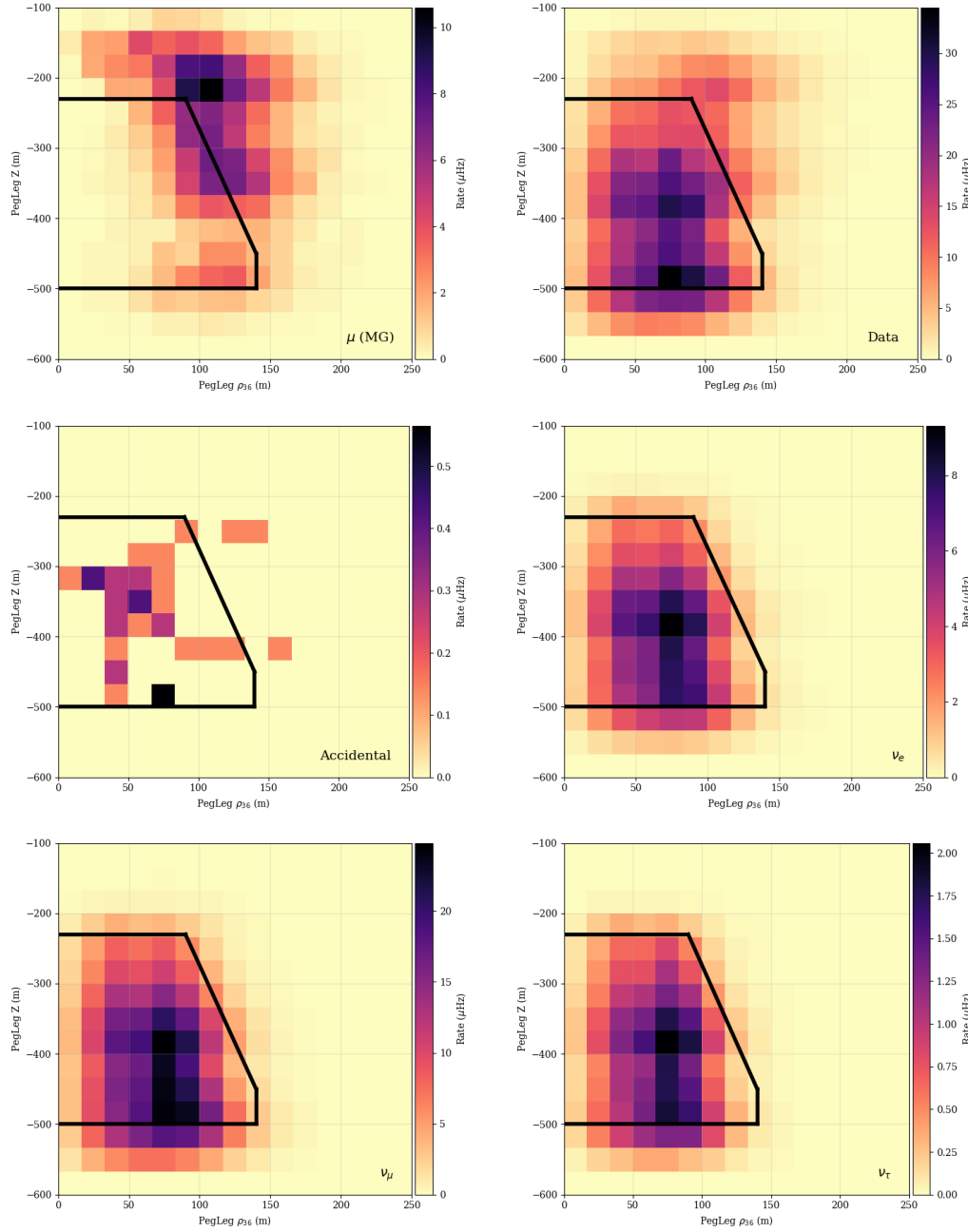


**Table 7.2** – The PegLeg L7 containment cut for each of the channels. The cut itself is shown with the black line. Note that the atmospheric muons are here represented by the higher-statistics MuonGun sample.

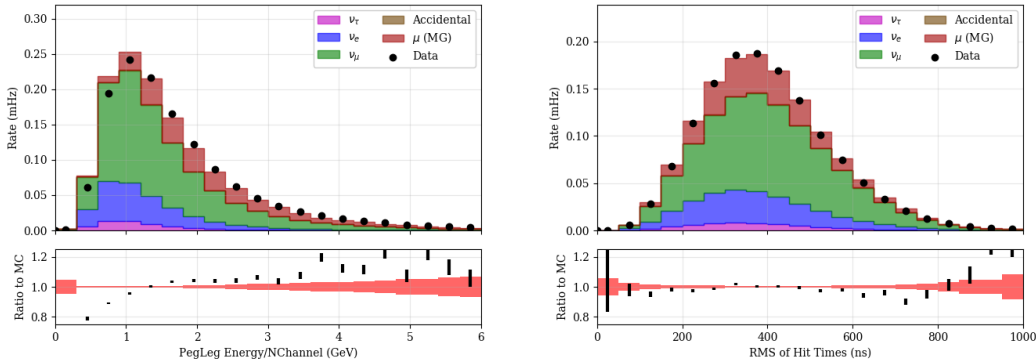


**Table 7.3** – The final two cuts applied to the sample prior to the analysis binning. All events are included here, although each cut is only applied to events with fewer than 14 hit DOMs. Note that the total simulation rate is scaled downward by 20% to approximately match the rate of the data events.

Type	IceCube Processing			GRECO				Analysis Binning
	Any Filter	DC Filter	Low-en L3	L4	L5	L6	L7	
CORSIKA	990598	9178	969.818	50.511	4.100	0.443	0.100	0.092
MuonGun	60669	2982	442.493	33.562	3.022	0.315	0.080	0.07
Accidentals	35855	8117	283.559	11.963	1.799	0.102	0.002	0.001
$\nu_e$	1.842	1.721	1.262	0.783	0.544	0.362	0.325	0.194
$\nu_\mu$	11.317	6.360	4.758	2.503	1.629	1.011	0.676	0.552
$\nu_\tau$	0.293	0.270	0.206	0.134	0.103	0.074	0.051	0.045
MC Total*	1026466	17303	1260	65.893	8.176	1.991	1.153	0.884
Data	1154426	19092	1092	68.592	7.422	1.841	0.871	0.715

**Table 7.4** – The event rates at each cut level in the GRECO selection. Note that the MuonGun events are included in this table, but do not contribute to the total Monte Carlo expectation to prevent double-counting of muon events from the CORSIKA sample. All rates are given in millihertz.

with a root-mean-square hit time of 600 nanoseconds, is also only applied for events with fewer than 14 hits. This limits the loss of neutrino events while removing a fraction of the remaining accidental triggers.

## 7.2 The Properties of the GRECO Event Selection

The completion of cuts yields the completed GRECO event selection. The rates of each sample of simulation and data are shown numerically in ?? or graphically in ???. Also included is the analysis binning as described in ?? for reference.

### 7.2.1 Energy and Zenith Reach

The GRECO sample covers a wide range of energies, with some final level events possessing energies as low as 2 GeV or as high as 1 TeV. The bulk of the neutrino sample, shown in ??, occurs at the expected oscillation minimum near 25 GeV. Most neutrino events originate at the horizon, as expected from the atmospheric neutrino flux, although there

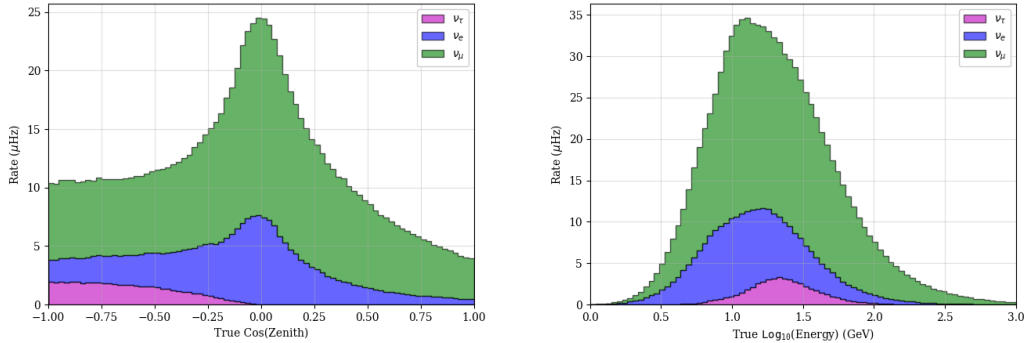


**Table 7.5** – The true neutrino energy and zenith of the GRECO sample at final level. The sample shows an asymmetry between upgoing ( $\cos(\theta) < 0$ ) and downgoing ( $\cos(\theta) > 0$ ) event rates in the neutrinos due to selection bias. The sample has a long tail of events at both high and low energies. Using the NuFit 2.2 oscillation parameters and the flux model from Honda, the  $\nu_\tau$  events are observed in the very upgoing region around  $10^{1.4} = 25$  GeV.

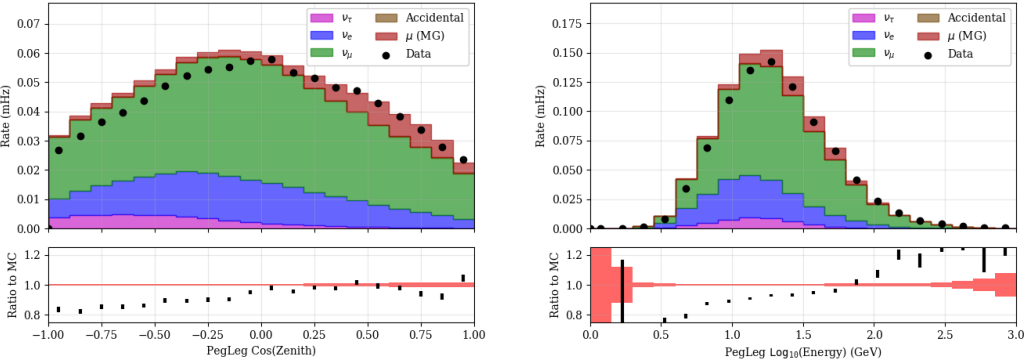


**Table 7.6** – The reconstructed energy and zenith of the GRECO sample at final level. Events in data reconstruct to both relatively high energies ( $E_R > 100$  GeV) and very low energies ( $E_R \approx 2$  GeV). Using the NuFit 2.2 oscillation parameters and the flux model from Honda, the  $\nu_\tau$  events are observed in the very upgoing region around  $10^{1.4} = 25$  GeV.

exists an asymmetry between the upward- and downward-going events. This asymmetry originates from the event selection, which selects against downward-going events in order to minimize the atmospheric muon background.

## 7.2.2 Reconstructed Variables

The true variables of the neutrino distributions are not observables in most GRECO analyses. Instead, all events are described using the reconstructed energies and zenith angles. The  $\nu_\tau$  sample reconstructs to slightly lower energies due to the loss in energy from the outgoing neutrino. The sample, when compared to data, shows reasonable shape agreement in both energy and zenith, although systematic disagreements occur above 100 GeV.

# A Search for Tau Neutrinos from Oscillations

## 8.1 Expectations from Monte Carlo

### 8.1.1 Choice of Binning

In order to understand the potential for IceCube's measurement of  $\nu_\tau$  appearance, a choice of binning must be decided upon. The analysis discussed here uses two variables to describe the oscillations: the reconstructed energy and zenith angle. These dimensions form an integral part of the standard oscillation analysis and are often used in measurements of atmospheric mixing parameters .

The choice of binning for zenith angles is selected to be similar, but somewhat finer than previous work . For this work, we use the fully sky, including upgoing events ( $\cos(\phi) = -1$ ) corresponding to events passing through the full diameter of the Earth where we expect the strongest oscillation effects to very downgoing events ( $\cos(\phi) = 1$ ) where events are originating in showers above the Antarctic. The energy binning is selected to match previous work from DeepCore and consists of 8 bins logarithmically spaced from 5.6 GeV to 56 GeV .

In addition, recent work with DeepCore has shown that a third dimension separating the sample into cascade-like and track-like events may provide better sensitivity than using solely track-like events. Two variables are available in the GRECO sample. The first, the reconstructed length of a muon track, provides a simple separation between events with a clear muon track from those without one. This, in general, leads to reasonable separation between the  $\nu_\mu$  events undergoing disappearance and  $\nu_\tau$  events undergoing appearance. This may be seen in , where the cumulative distribution of the various simulation components are shown as a function of the reconstructed track length. The separation between the  $\nu_\mu$  and  $\nu_\tau$  charged-current samples occurs between 30-50 meters. By separating the sample into cascade-like events (eg.  $L < 50$  m) and track-like events ( $L \geq 50$  m), the disappearance and appearance may be partially disentangled.

The second potential separating variable is the likelihood ratio between a cascade and PegLeg's mixed cascade+track reconstructions. A higher likelihood (lower log-likelihood) in the cascade fit implies that the event is more likely intrinsically cascade-like while the reverse is true for intrinsically track-like events. The cumulative plot of the likelihood ratio is shown in . There exists a broad choice of values with similar separation properties from approximately  $-4 < \Delta LLH < -2$ . Once again, separating events into two samples using the likelihood ratio may improve the ability of the analysis to disentangle the disappearance and appearance effects.

Both variables clearly show some separating power and likely have similar behavior: an event with a longer reconstructed muon track should be expected to prefer the PegLeg reconstruction over a cascade reconstruction. In order to choose between the parameters, the efficacy of separating each of the simulation samples from the  $\nu_\tau$  charged current signal was evaluated. The results are shown in , which give the fraction of each type rejected and the number of  $\nu_\tau$  events accepted into the "cascade-like" sample for various choices of the separating parameters. Values further from a diagonal indicate better separation between the  $\nu_\tau$  and other event types. Here we see that the track length performs uniformly better than the likelihood ratio in separating the disappearing  $\nu_\mu$

list of atmo disappearance measurements that use zenith and energy binning

dragon, leesard 3 year papers

dragon, leesard

cumulative plot of track length

cumulative plot of deltalh

roc curves for track length

this sentence needs to be rewored. its too verbose

charged-current and appearing  $\nu_\tau$  charged current events. Furthermore, the reconstructed track length performs significantly better in separating the neutrino components from the atmospheric muon background. The reconstructed track length is therefore selected as the separating variable for this analysis.

### 8.1.2 The MC Fit Templates

A choice of 50 meters of reconstructed track length is selected for this analysis. Because the PegLeg reconstruction assumes the muon track to be minimally ionizing, the division of track-like and cascade-like has an effect on the minimum energy of each sample. In particular, no track-like events ( $L \geq 50$  m) may have less than 10 GeV in total reconstructed energy. Both track- and cascade-like events may reconstruct with higher energies than 10 GeV.

The binned expectations used in the fit are shown in assuming the oscillation parameters given by . The lack of expected events in the track-like histogram is clearly visible. As expected, atmospheric muon background events tend to reconstruct as downgoing events, primarily visible in the track-like channel. The signal  $\nu_\tau$  events occur in the very upgoing cascade channel and make up, at most, approximately 10% of the events in those bins.

mc templates!  
nufit 2.2

## 8.2 Parametrizing the Tau Neutrino Appearance

In order to properly measure the appearance of  $\nu_\tau$  events, a choice of "appearance parameter" must be selected. Here, we discuss the choice of parameter used in this analysis.

### 8.2.1 CC vs CC+NC

As described in ??, neutrinos may interact in two distinct ways to produce light in the IceCube detector. These two methods, the charged-current and neutral-current interactions, provide separate windows into neutrino interactions. Tau neutrino events may interact in either of these channels depending on the neutrino energy.

With a mass of  $1776.82 \pm 0.16$  MeV and a lifetime of  $290.3 \pm 0.5$  femtoseconds ,  $\tau$  leptons produced during neutrino oscillations in DeepCore tend to travel very short distances before decaying. The charged-current interactions of the  $\nu_\tau$  result in a variety of signatures due to the unique decay behavior of the  $\tau$  lepton.

$$\tau^- \rightarrow \begin{cases} \mu^- \bar{\nu}_\mu \nu_\tau & 17.41 \pm 0.04\% \\ e^- \bar{\nu}_e \nu_\tau & 17.83 \pm 0.04\% \\ \text{Hadrons} & \text{Otherwise} \end{cases} \quad (8.1)$$

PDG

In either the muonic or the electronic decay modes, a fraction of the energy is lost to outgoing neutrinos, resulting in a smaller observed charge than would be associated with a corresponding interaction of another neutrino type. Furthermore, the muonic decay mode may lead to a visible muon track for the  $\nu_\tau$  interaction. These muon tracks associated with the appearance of  $\nu_\tau$  would appear at lower energies than the tracks corresponding to the  $\nu_\mu$  disappearance, allowing both effects to be observed simultaneously.

Unlike the varied results of the charged current interactions, neutral current interactions of neutrinos are assumed to have identical coupling and behavior, regardless of flavor and, therefore, undergo no observable change due to oscillations. Because of this, studies of the standard unitary PMNS matrix tend to treat neutral current events as effectively non-oscillating . In contrast, searches for new physics and sterile neutrinos result can result in a change in the apparent number of neutral current interactions in the detector.

superk paper, opera paper sources for unoscillating NC

For this analysis, both approaches have been adopted. A fit using charged-current events as the signal is used to provide limits on the modifications to a 3x3 mixing matrix without the introduction of neutral-current altering behavior. A second fit, including both neutral current and charged current  $\nu_\tau$  events, provides more insight into possible extra flavors of neutrinos.

### 8.2.2 The $\nu_\tau$ Normalization

Because effectively all  $\nu_\tau$  events observable in DeepCore are the result of neutrino oscillations, the total number of observed  $\nu_\tau$  interactions is a direct measure of the appearance itself. The number of  $\nu_\tau$  events interacting in DeepCore is, however, affected by many of the previously-discussed systematics. In particular, the number of events is strongly related to the assumed atmospheric oscillation parameters.

In order to provide a quantitative measure of the appearance, the overall normalization of signal events is used as a final physics parameter. The normalization is a fit parameter, defined to be a total modification of the number of candidate  $\nu_\tau$  events after all other systematic parameters are applied.

$$f'_{ijk} = \sum_{m \neq \nu_\tau} f_{ijk}^m(\theta_{23}, \Delta m^2, \dots) + N_{\nu_\tau} f_{ijk}^{\nu_\tau}(\theta_{23}, \Delta m^2, \dots) \quad (8.2)$$

In this case, we end up with two general cases for the result. In the expected case,  $N_{\nu_\tau} = 1.0$ , we find that the number of candidate events is consistent with our modeling of the  $\nu_\tau$  and unitary PMNS mixing. If the value is significantly different from 1.0, we may have hints of either mismodeled cross-sections or of novel physics. Due to the large existing uncertainties in the PMNS matrix described in ??, either situation is likely to yield valuable information.

### 8.2.3 Limits on the $\nu_\tau$ Normalization

This analysis is not the first to search for appearance in this way. Two other experiments, OPERA and Super-Kamiokande, have reported previous measurements parametrized in the same way.

#### The OPERA Limit

The Oscillation Project with Emulsion-tRacking Apparatus, better known by the acronym OPERA, is an experiment designed to search for  $\nu_\tau$  appearance. Unlike IceCube's use of atmospheric neutrinos, OPERA uses muon neutrinos produced in the CERN Neutrinos to Gran Sasso (CNGS) beamline. OPERA uses bricks of photographic films in order to accurately track and reconstruct neutrino interactions in the fiducial volume. This technique allows analysizers to clearly identify not only the initial neutrino interaction vertex, but also the decay products along the path of the charged lepton produced in charged current interactions. In OPERA, the muon and tau lepton produce significantly different signals due to the short lifetime and unique decay properties of the tau lepton. The impressive ability to identify the particle dynamics is balanced by the small fiducial volume of the experiment, yielding only 5408 useful events for analysis from five years of data-taking.

In 2015, OPERA released their final result in the search for  $\nu_\tau$  appearance. Five candidate events, shown in , were identified in the data sample with a signal expectation of  $2.64 \pm 0.53$  and a background expectation of  $0.25 \pm 0.05$ . The data unambiguously rules out the no-appearance hypothesis, with a rejection at  $5.1\sigma$ .

non-sterile explanations  
of non-unitarity? maybe  
the neutrino decay pa-  
per?

think up a better phras-  
ing to introduce the tau  
normalization

Crazy shit that I will  
probably take out, but  
maybe find the neutrino  
decay paper again?

opera tau neutrino event  
views

opera paper:  
<https://arxiv.org/abs/1507.01417>

Interaction Mode	Non-tau-like	tau-like	All
CC nue	3071.0	1399.2	4470.2
CC numu	4231.9	783.4	5015.3
CC nutau	49.1	136.1	185.2
NC	291.8	548.3	840.1

**Table 8.1** – The rates expected for each of the neutrino types in the Super-Kamiokande search for  $\nu_\tau$  appearance. Reproduced from.

In terms of the normalization described above, OPERA reported a final value of  $1.8^{+1.8}_{-1.1}$  at the 90% level. This value is consistent with the standard unitary oscillation scheme, but with large errors.

## The Super-Kamiokande Limit

Super-Kamiokande, described in ??, also has reported results in searches for  $\nu_\tau$  appearance. The Super-Kamiokande collaboration developed a new event selection in the search for  $\nu_\tau$  events, including the implementation of a neural net to identify  $\tau$ -like and non- $\tau$ -like events. The neural net itself includes information about the energy of the event and is trained against a background sample of simulated events. Events are analyzed in terms of the zenith angle and the neural net output variable.

These two categories of events are fit with an unbinned likelihood including 28 systematic effects included in the analysis.

here

The Super-Kamiokande measurement yields an expectation of 185.2  $\nu_\tau$  events in 5326 days or approximately 12.7 events per year. After fitting, the final rejection of the no-appearance hypothesis is found to be  $4.6\sigma$ . Like OPERA, Super-Kamiokande finds more  $\nu_\tau$  candidate events than expected, with a best-fit normalization of  $1.47 \pm 0.32$ .

superk paper  
on appearance  
<https://arxiv.org/pdf/1711.0>

<https://arxiv.org/pdf/1711.0>  
again

wtf is going on here? table 1 in the paper gives an expectation of 185.2 events, but the stuff at the top right of page 11 says the expectation is 224...?! and NEITHER of these give the 1.47 that they quote. wtf

figure 14 of  
<https://arxiv.org/pdf/1711.0>

nufit 2.2

## 8.3 Systematics Considerations

### 8.3.1 Oscillation Parameters

The GRECO selection is primarily sensitive to atmospheric neutrinos around 30 GeV. These neutrinos travel distances from approximately 30 km (directly downgoing) to 6400 km (directly upgoing). At these energies and distances, little effect is expected from the solar and reactor parameters. This has been tested with the GRECO sample by changing each parameter by the  $1\sigma$  range given in . The total value of the  $\chi^2$ , defined as in ??, was used to select the most important parameters for this fit.

The results are shown in ???. The atmospheric mixing parameters have significantly larger impacts on the analysis histogram than the other parameters. For the purposes of GRECO analyses, only these parameters are therefore considered.

### 8.3.2 Neutrino Flux Uncertainties

The underlying flux models of the neutrino and background muon provides significant uncertainties for this analysis.

## Neutrino Spectral Index

Parameter	Baseline	Tested Shift	$\sum_{bins} \chi^2$
$\Delta m_{31}^2$	$2.2526 \times 10^{-3}$	$+0.10 \times 10^{-3}$	2.776
$\Delta m_{21}^2$	$7.49 \times 10^{-5}$	$+0.19 \times 10^{-5}$	$5.392 \times 10^{-4}$
$\theta_{23}$	0.72431	+0.02094	1.262
$\theta_{13}$	0.14765	+0.00262	$1.802 \times 10^{-3}$
$\theta_{12}$	0.58853	+0.01379	$2.978 \times 10^{-4}$
$\delta_{CP}$	0.0	$+\frac{\pi}{2}$	$2.407 \times 10^{-2}$

**Table 8.2** – Total  $\chi^2$  impact of each of the oscillation parameters. The atmospheric mixing parameters,  $\Delta m_{31}^2$  and  $\theta_{23}$  are the most important oscillation parameters for the GRECO selection. Of the remaining parameters, the CP-violating phase is the next most important.

### $\nu_e/\nu_\mu$ Ratio

### $\nu/\bar{\nu}$ Ratio

### Upward to Horizontal Flux Ratio

### 8.3.3 Atmospheric Muon Flux

### 8.3.4 Propagation Uncertainties

### 8.3.5 Cross-section Uncertainties

#### Axial Masses

The axial mass terms control the cross section for the resonant and quasielastic interactions. Uncertainties are defined conservatively, following the default uncertainties available in the GENIE MC generator . These terms affect the number of low energy events in the sample, with the net effect shown in ?? . The breakdown of the final level neutrino sample is shown in ?? .

#### DIS Cross-sections

### 8.3.6 Detector Systematics

While the previous systematics have been concerned with global physics parameters, the remainder are dedicated to understanding the uncertainties associated with the IceCube detector itself, such as the properties of the PMTs and the ice. These parameters, collectively referred to as the *detector systematics*, do not have known analytic forms and may affect the rate of events, the reconstruction properties of a given event, or both. The effect of these uncertainties must be evaluated using additional Monte Carlo simulations. The GRECO event selection uses a number of simulation sets, shown in ?? for signal and ?? for background, to characterize the effects of these detector systematics. Each set contains at least one simulation parameter changed from the baseline set and are run through the full GRECO processing.

Set Number	Coincident Fraction	DOM Eff	Hole Ice	Forward Coeff	Absorption	Scattering	Livetime
Baseline	0%	100%	25	0	100%	100%	30 years
640C	100%	100%	25	0	100%	100%	30 years
641	0%	88%	25	0	100%	100%	30 years
643		94%					
644		97%					
645		103%					
646		106%					
648		112%					
660	0%	100%	15	0	100%	100%	10 years
661			20				
662			30				
663			35				
670	0%	100%	25	2.0	100%	100%	10 years
671				-5.0			
672				-3.0			
673				1.0			
674				-1.0			
681	0%	100%	25	0.0	92.9%	92.9%	30 years
682					110%	100%	
683					100%	110%	

**Table 8.3** – Systematics sets used for the characterization of the signal neutrino events. While all listed sets have up to 30 years of effective livetime available, not all events are processed in each set.

Set Number	Oversizing	DOM Eff	Hole Ice	Forward Coeff	Absorption	Scattering	Livetime	Comments
Baseline	1.0	99%	25	0	100%	100%	5 years	1 year standard + 4 years KDE Prescale
A	1.0	69.3%	30	0	100%	100%	1 year	1 year standard
B		79.2%						
C		79.2%	25					
D		89.1%						
E		105%						
F	1.0	99%	15	0	100%	100%	1 year	1 year KDE Prescale
G			30					
H	1.0	99%	30	-2	100%	100%	5 years	1 year standard + 4 years KDE Prescale
I				-4				
J	3.0	99%	25	0	100%	100%	1 year	1 year KDE Prescale
K					110%			
L					80%			
M					100%			
N						80%		
O						110%		
P						120%		
Q						92.9%		
						114.2%		

**Table 8.4** – Systematics sets used for the characterization of the atmospheric muon background.

## Coincident Fraction

The GENIE simulation sets are produced with exactly one neutrino interaction per event. In the actual detector, a fraction of triggered events will consist of a temporally coincident muon and neutrino pair which may be from the same air shower or from independent showers. In order to account for this possibility, a sample of such events are simulated assuming independent showers. In this case, every produced event contains at least one atmospheric muon in addition to exactly one neutrino interaction. By interpolating between this "100% coincident" sample and the standard "0% coincident" sets, the effect of these events may be included in the final analysis.

The GRECO event selection actively selects against atmospheric muon-like events. The lowest-order effect of this choice is that increasing the coincident event fraction leads to a correspondingly lower total event rate, as shown in ???. In order to distinguish the effect of the coincident events from a global normalization factor, the coincident event fraction is treated in a manner such that the total rate of events remains unchanged. The effect of this systematic in the final analysis is therefore shown in instead.

In most analyses in IceCube, a coincident event fraction of approximately 10% is assumed. This is derived from a combination of the atmospheric neutrino and muon fluxes assuming independent poissonian rates. At final level, the true fraction of coincident events is unknown, but previous oscillation analyses have found no clear issues using the standard simulation sets assuming no coincident events. A generous prior is therefore assumed to be a one-sided Gaussian distribution centered at 0% with a 10% width.

coin fraction figure

## DOM Efficiency

As with all PMTs, the light detection probability of the IceCube DOMs is not perfect. Indeed, the total efficiency of detecting incident photons as measured by Hamamatsu, shown in ??, is about 30% for the R7081-02 PMT used in standard IceCube DOMs. Before and during deployment, the net quantum efficiency of some DOMs were tested . The efficiency of the DOMs was again measured in-situ in order to better account for local effects like cable shadowing and the glass-ice interface. Dedicated measurement post-deployment have used minimum ionizing muons in data and simulation and derived a modification of the assumed efficiency, hereafter referred to as the *DOM efficiency*, of  $99\% \pm 10\%$ .

The DOM efficiency scales the probability of observing photons incident at the face of the DOM. A higher DOM efficiency leads to more information about individual particle interactions, leading to better reconstructions. The improved reconstructions lead to higher neutrino event rates at final level as well as more well-defined oscillation features in the reconstructed space. In addition, higher DOM efficiency increases the number of hits observed along atmospheric muon tracks, yielding improved veto efficiency. The net effect of changing the DOM efficiency by 10% is shown in .

Hamamatsu quantum efficiency? [http://www.hamamatsu.com/resources/pdf/etd/LARGE\\_AREA\\_PMT\\_TPMH1286E.pdf](http://www.hamamatsu.com/resources/pdf/etd/LARGE_AREA_PMT_TPMH1286E.pdf)

How many were tested in a lab before deployment?

Where does the domeff prior come from?

domeff

## Bulk Absorption and Scattering

The ice model used in IceCube is fit in-situ using various data from the deployment and detector operation in a process similar to the one described in ???. The model, here referred to as the *bulk ice model*, consists of scattering and absorption coefficients fit as a function of depth within the detector as well as information about anisotropy in the scattering properties of the ice . Uncertainties for these scattering and absorption coefficients, shown in , provide a significant source of uncertainty for physics measurements

ice model

bulk ice uncertainties vs depth

in IceCube. To handle these effects, global scale factors are used to modify all scattering or absorption coefficients in the bulk ice model simultaneously. Using the most recent published uncertainties on our ice model, a total uncertainty of approximately 10% is assumed for these global scale factors. Three variations are typically used, corresponding to sets with 10% larger absorption coefficients, 10% larger scattering coefficients, and a 7.1% reduction to both sets of coefficients.

The scattering and absorption exhibit different behaviors at final level in the GRECO sample. In general, the absorption behaves in a similar manner to the DOM efficiency, as both parameters modify the number of observed photons at the face of the PMT. In the signal samples, the effects of absorption uncertainties is relatively small. The most notable feature is an overall rate decrease (increase) for larger (smaller) absorption coefficients. As in the DOM efficiency, the depth of the oscillation minimum is also affected by the absorption coefficients due to a change in the reconstruction resolution.

absorption The absorption, shown in , affects the atmospheric muons much more strongly than the neutrinos. Once again, this is due to the event selection: with weaker absorption (ie, smaller coefficients), more photons from the muon track may be detected. The observation of additional photons from the muon track improves the veto efficiency, leading to a significant decrease in the number of muons at final level.

scattering The scattering, in contrast, has very little effect on the muon distribution, as seen in . No changes in rate or in reconstruction resolution are observed in the muon distributions. In the neutrinos, the effects of the scattering are more important. In particular, stronger scattering (larger coefficients) lead to a reconstruction bias, with more events reconstructing as downgoing. This is a known effect of the reconstruction, where we use a version of the ice model which interprets off-time hits as being due to backscattered photons in a downgoing event.

## Hole Ice and Foward Scattering

While the bulk ice refers to the scattering and absorption properties of the entire interaction volume, additional care must be taken for the ice close to the face of a PMT. During deployment, contaminants, including air, were introduced into the drill holes. These contaminants have been seen to form a dense column with unique scattering properties near the center of the drill holes. This bubble column, known as the *hole ice*, has properties separate from the rest of the ice model.

The uncertainties associated with the hole ice are significant and tend to elicit more attention than bulk ice uncertainties in searches for oscillations with DeepCore. The simulation of the hole ice model used here, discussed briefly in ??, requires two free parameters which will be referred to as the *lateral* and *forward* scattering parameters here for clarity. The lateral scattering modifies the efficiency of accepting photons incident from the horizon at each DOM while the forward scattering modifies only the acceptance of the very-forward region. The models of the angular acceptance are shown in .

hole ice and hifwd The effects of the two hole ice parameters show very similar behavior to that of the scattering uncertainty in the bulk ice, as all three coefficients are modeling the scattering properties of different locations in the ice.

## Parametrizing with Hyperplanes

For each of the simulation sets and each particle type, histograms are produced using the reconstructed energy, zenith, and track length. These systematic histograms give information about the expected change of the final histogram as a function of the changing

systematics parameters, but the information is encoded in discretized points with statistical fluctuations due to the finite simulation statistics. In order to produce continuous systematics for analysis, the discrete detector systematics must be parametrized.

For this work, a hyperplane is fit to the detector systematics sets for each particle type and for each bin in the analysis histogram.

For neutrinos, a simple linear model is assumed for each detector systematic, with one free coefficient associated with each systematic as well as one free constant term independent of the systematics. The form of the hyperplane for each neutrino type in the bin  $ijk$  is given by ??.

how do i flesh this out?

$$f'_{ijk} = \left( \sum_m^{detsys} \left( a_m^{ijk} (x_m - x_m^0) \right) + b^{ijk} \right) f_{ijk} \quad (8.3)$$

For atmospheric muons, the form is slightly modified due to the strong effects observed from both the DOM efficiency and the absorption. In these two cases, an exponential model is selected to better describe the observed effects in simulation.

muongun rates vs domeff and absorption to justify exponentials

$$f'_{ijk} = \left( \sum_{m \neq DE, Abs}^{detsys} \left( a_m^{ijk} (x_m - x_m^0) \right) + \sum_{m=DE, Abs}^{DE, Abs} \left( a_m^{ijk} e^{b^{ijk} (x_m - x_m^0)} \right) + c^{ijk} \right) f_{ijk} \quad (8.4)$$

Need to include some discussion of the goodness of fit for these sets. Maybe a plot of the chi2 values for all of the sets?

## 8.4 The Method of Maximum Likelihood

### 8.4.1 The $\chi^2$ Fit

chi2 values for hyper-plane parametrizations

The simplest implementation of a fitting algorithm begins with an assumption of the true and observed distributions. Namely, that the observed number of events in each bin of the histogram is drawn from a distribution approximately Gaussian with a mean  $\mu$  equal to the expectation from simulations and a variance  $\sigma^2$  calculated from the Poisson uncertainty on the expectation.

$$P(x|\mu) = N e^{\frac{1}{2} \frac{(x-\mu)^2}{\sigma^2}} \quad (8.5)$$

where  $N$  is a normalization constant and, in the case of Poissonian statistics of simple histograms, the variance is given by the event weights in the specified bin.

$$\sigma^2 = \mu = \sum w \quad (8.6)$$

From this point, taking the logarithm yields the standard  $\chi^2$  definition for the likelihood after dropping the constant terms.

This needs work. can't even be called a derivation. its just crap.

$$\chi^2 = \frac{(x - \mu)^2}{\mu} \quad (8.7)$$

### 8.4.2 Finite Statistics

The  $\chi^2$  distribution above implicitly assumes that the dominant source of uncertainty at the best-fit point comes from the statistical fluctuations of the data around the true distribution represented by the Monte Carlo simulation. While this is true in the ideal case, in practice the statistical properties of the simulation sets themselves cannot be

ignored. In general, every attempt should be made to ensure the statistical fluctuations of the simulation sets are negligible compared to those of the data. This typically leads to requests for at least an order of magnitude larger simulation statistics than expected from the data itself. In the situation where this is infeasible, modifications to the likelihood space itself may be used to account for the additional uncertainties. For this analysis the statistical uncertainties of the underlying simulation sets are added to the weighted uncertainties in quadrature.

$$\chi_1^2 = \frac{1}{2} \frac{(x - \sum w)^2}{(\sum w)^2 + \sum w^2} \quad (8.8)$$

Due to the large uncertainties associated with the atmospheric muon sample, further considerations are necessary. In particular, the large uncertainties associated with atmospheric muon simulation statistics may be used by the fitter in order to reduce the  $\chi_{FS}^2$  value. This situation proceeds with the minimization process as normal until a runaway effect is observed by increasing the statistical uncertainties at the expense of data/simulation agreement. In this case, the numerator becomes simply

$$\lim_{N_\mu \rightarrow \infty} (x - \sum w)^2 = (\sum w)^2 \quad (8.9)$$

The resulting limit in each bin as the event weights become large is therefore

$$\lim_{N_\mu \rightarrow \infty} \chi_1^2 = \frac{(\sum w)^2}{(\sum w)^2 + \sum w^2} \quad (8.10)$$

$$\lim_{N_\mu \rightarrow \infty} \chi_1^2 = 0 \quad (8.11)$$

While this is a particular concern for all simulation types, the dominant contribution to the  $\sum w^2$  term is the atmospheric muons. In addition, the atmospheric muons have the strongest impacts from non-normalization systematic uncertainties, particularly the DOM efficiency and the absorption. Modifying either of these parameters or the normalization systematics in the fit may lead to this runaway behavior.

In order to prevent this situation, a further modification of the  $\chi^2$  is necessary. For this analysis, the total scale of the statistical uncertainty is assumed to be set by the seed values of the fit.

$$N_{w^2} = \frac{\sum w_{Seed}^2}{\sum w^2} \quad (8.12)$$

With this modification, the  $\chi^2$  is now defined to be

$$\chi_{FS}^2 = \frac{1}{2} \frac{(x - \sum w)^2}{(\sum w)^2 + N_{w^2} \sum w^2} \quad (8.13)$$

Taking the limit of this  $\chi^2$  in a single bin as the event weights become large now gives

$$\lim_{N_\mu \rightarrow \infty} \chi_{FS}^2 = \frac{1}{2} \frac{(x - \sum w)^2}{(\sum w)^2 + N_{w^2} \sum w^2} \quad (8.14)$$

$$\lim_{N_\mu \rightarrow \infty} \chi_{FS}^2 = 1 \quad (8.15)$$

This is in agreement with the limit obtained from the standard  $\chi^2$ .

make a plot showing chi2 value as a function of mc stats scale factor to justify the 10x rule

this is only true for muons! how do i explain that?

### 8.4.3 Fit Priors

In many cases, the systematics listed in ?? have known constraints from external measurements. This information can be useful and should be included in the analysis to bias the minimization toward the most likely systematics values. These constraints are included in the form of *priors* in the analysis. Priors are additional terms included multiplicatively (additively) in the likelihood (log-likelihood) calculation. These often take the form of a Gaussian distribution with mean  $\mu$  and variance  $\sigma^2$  given by external measurements. For this measurement, most priors are handled assuming a standard Gaussian form. For a systematic  $i$  with value  $x_i$ , these additional terms take the form

$$\chi_i^2 = \frac{(x_i - x_0)^2}{\sigma^2} \quad (8.16)$$

These additional terms are added to ?? in order to calculate the final  $\chi_{FS}^2$  used in the minimization for this analysis.

$$\chi_{Total}^2 = \sum_{bins} \chi_{FS}^2 + \sum_{systematics} \chi_i^2 \quad (8.17)$$

A list of priors is shown in ?? . Note that the coincident event fraction is effectively a one-sided Gaussian due to physical constraints on the value.

All of these references  
for the priors...

	Systematic	Unit	Type	Baseline/Seed Value	Prior	Allowed Range	Reference
Physics Parameter	$N_{\nu_\tau}$	-	Analytic	1.0	-	0.0 - 2.0	-
Oscillations	$\Delta m_{3j}^2$ $\sin^2 \theta_{23}$	$10^{-3} \text{ eV}^2$ -	Analytic Analytic	2.526 0.440 (NO), 0.66 (IO)	- -	2.0 - 3.0 0.0 - 1.0	nufit nufit
Total Rates	$N_n u, N_m u$	Years	Analytic	2.25	-	0.0 - 10.0	-
Cross-section	Axial Mass (QE) Axial Mass (RES) $N_{\nu,NC}$	$\sigma$ $\sigma$ -	Analytic Analytic Analytic	0.0 0.0 1.0	$0.0 \pm 1.0$ $0.0 \pm 1.0$ $1.0 \pm 0.2$	-5.0 - 5.0 -5.0 - 5.0 0.0 - 2.0	GENIE GENIE NC prior
Flux	$\gamma_\nu$	-	Analytic	0.0	$0.0 \pm 0.10$	-0.50 - 0.50	Honda
	$\gamma_\mu$	$\sigma$	Analytic	0.0	$0.0 \pm 1.0$	-5.0 - 5.0	ste and davide's paper
	Up/Horizontal Ratio	$\sigma$	Analytic	0.0	$0.0 \pm 1.0$	-5.0 - 5.0	Barr
	$\nu/\bar{\nu}$ Ratio	$\sigma$	Analytic	0.0	$0.0 \pm 1.0$	-5.0 - 5.0	Barr
	$\Phi_{\nu_e}$	-	Analytic	1.0	$1.0 \pm 0.05$	0.8 - 1.2	Barr
	Coincident Fraction	-	Hyperplane	0.0	$0.0 + 0.10$	0.0 - 1.0	coin fraction...?
Detector	DOM Efficiency	-	Hyperplane	1.0	$1.0 \pm 0.1$	0.7 - 1.3	DOM eff
	Hole Ice (Lateral)	-	Hyperplane	0.25	$0.25 \pm 0.10$	0.0 - 0.5	hole ice
	Hole Ice (Forward)	-	Hyperlane	0.0	-	-5.0 - 5.0	hole ice
	Absorption	-	Hyperplane	1.0	$1.0 \pm 0.1$	0.5 - 1.5	bulk ice
	Scattering	-	Hyperplane	1.0	$1.0 \pm 0.1$	0.5 - 1.5	bulk ice
							for Tau Neutrinos from Oscillations

**Table 8.5** – Priors and allowed ranges for each systematic included in this analysis.

## 8.5 Expected Sensitivity to Appearance

### 8.5.1 Fitting Code

Checks in this analysis are first performed using solely simulation files. In order to understand the expected sensitivity of this analysis, a fitting package previously used to fit the  $\nu_\mu$  disappearance . The code, known as *OscFit*, works in multiple stages. After separating the simulation into separate channels consisting of  $\nu_e^{CC}$ ,  $\nu_\mu^{CC}$ ,  $\nu_\tau^{CC}$ ,  $\nu^{NC}$ ,  $\mu_{atm}$ , and accidental triggers, the analytic systematics are applied. These systematics solely rely on information about the particle interaction in order to calculate correction factors to the event weights and are not sensitive to the order of application. The oscillation calculations are performed at this stage and are based on the Prob3++ code to calculate the full three-flavor unitary oscillations including matter effects within the Earth.

When including the neutral current interactions from  $\nu_\tau$  events in the signal definition, the neutral current events are reweighted for oscillations at this stage. The *OscFit* code assumes the neutral current interaction rate is unaffected by oscillations and the  $\nu_\tau^{NC}$  events are not directly included in favor of the significantly higher simulation statistics from the other sets. Because no charged leptons are produced in the neutral current interactions, no differences in event topology are expected based on flavor of neutrino interaction. For the purposes of this analysis, the neutral current interactions from  $\nu_e$  and  $\nu_\mu$  events are instead used to model the effect of the  $\nu_\tau^{NC}$  events. The Prob3++ code calculates oscillation probabilities for these events given the expected contribution to the neutral current event rate from  $\nu_\tau^{NC}$  events.

$$R_{\nu_\tau^{NC}} = R_{\nu_e^{NC}} P_{\nu_e \rightarrow \nu_\tau} (\theta_{23}, \Delta m_{3i}^2) + R_{\nu_\mu^{NC}} P_{\nu_\mu \rightarrow \nu_\tau} (\theta_{23}, \Delta m_{3i}^2) \quad (8.18)$$

The modification to the total neutral current rate given the  $\nu_\tau$  normalization,  $N_{\nu_\tau}$ , is then given by

$$R_{\nu^{NC}} = R_{\nu^{NC}} + R_{\nu_\tau^{NC}} (N_{\nu_\tau} - 1) \quad (8.19)$$

The modified weights are then used to histogram the simulated event samples into one histogram per simulation channel. After histogramming, the detector systematics are applied to the each of the binned templates bin-by-bin using hyperplanes calculated for each bin as described in ???. The hyperplanes themselves are created using the same process, but are created only once using the baseline systematics values and oscillation parameters taken from . More in-depth tests have shown little change when accounting for changes in the hyperplane coefficients as a function of different oscillation parameters.

Once all systematics have been applied, the normalization terms representing the overall scale factors for the neutrino rate,  $N_\nu$ , the muon rate,  $N_\mu$ , and the accidental rate,  $N_{noise}$ , are multiplied to the respective histograms. The final histograms are summed together to form the final simulation expectation to be compared to the data using the  $\chi^2_{FS}$  described in ??.

The value of the  $\chi^2_{FS}$  is minimized as a function of the various systematics using the iMinuit2 package. The minimization continues until the requested tolerance,  $10^{-16}$ , is reached by the minimizer, after which the best fit histogram and systematics values are returned to the user.

Maybe all of this osc-fit stuff should just be moved to just before the systematics section.

should i even talk about oscfit itself? it seems a bit awkward

msu and desy disappearance

Flowchart of oscfit fitting. at least broadly

prob3++

nufit 2.2

iminuit

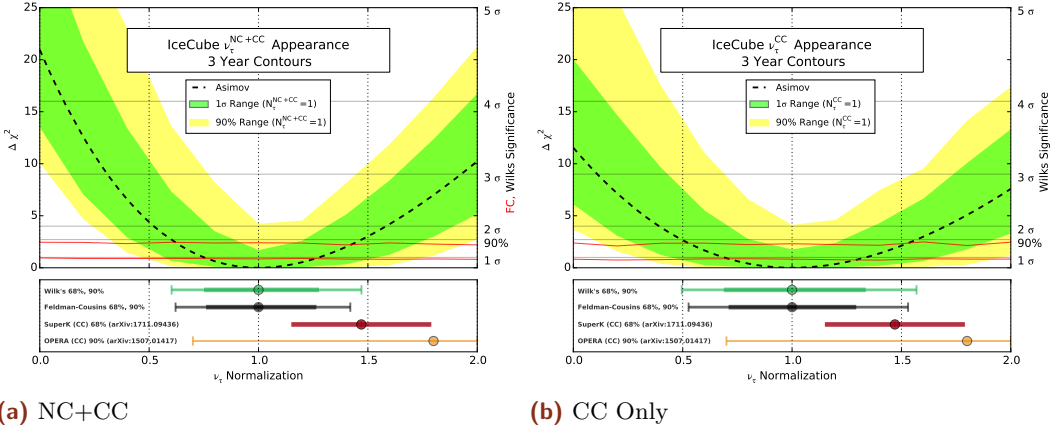


**Figure 8.1** – The sensitivity of this analysis in the (a) NC+CC and (b) CC-only channel. The top plot shows the Asimov expectation (black dotted line) and the Brazilian flag (green, yellow bands). The significances assuming Wilks's theorem (gray horizontal lines) and Feldman-Cousins (red horizontal lines) are also shown. The bottom plot shows the expected  $1\sigma$  and 90% ranges for Wilks theorem and Feldman-Cousins compared to the most recent results from the OPERA and Super-Kamiokande analyses.

### 8.5.2 Sensitivity of the Analysis

To evaluate the expected sensitivity of this analysis, the OscFit code is used to find the best-fit value of the  $\chi^2_{FS}$ . Multiple methods are used to evaluate both the average expected sensitivity and range of variation of the sensitivity due to both the data and simulation statistics. All of the methods are shown in Figure ?? Each component will be described in turn.

The first method, known as the *Asimov* expectation , begins by creating the expected histogram using baseline values of the systematics and oscillations. The produced histogram, representing an exact PDF of the expected events, is then used as an estimate of the data. The  $\chi^2_{FS}$  is then minimized while the value of  $N_{\nu_\tau}$  is fixed at regularly spaced points in the interval [0,2] in order to produce a contour. A final minimization is performed allowing the minimizer to identify the global best-fit value of  $N_{\nu_\tau}$ .

The final expected sensitivity in the Asimov approach is given by calculating the difference between the values of the  $\chi^2_{FS}$  at each point and the global best fit.

$$\Delta\chi^2(N_{\nu_\tau}) = \chi^2_{FS}(N_{\nu_\tau}) - \chi^2_{FS}(N_{\nu_\tau}^{Global}) \quad (8.20)$$

The value of  $\Delta\chi^2_{FS}$  as a function of  $N_{\nu_\tau}$  is shown in . These values may be converted into expected significance levels using the procedure described in Section ??.

The second method, producing what is known as a *Brazilian flag* plot due to the color scheme, provides an estimate of the expected range of sensitivities in this analysis. The production of a Brazilian flag begins with the production of a pseudo-data histogram from the Asimov histogram. Because the simulation sets used here have significant uncertainties due to limited simulation statistics, the first step is to vary the event rate in each bin within the statistical uncertainties of the Monte Carlo. To do so, histograms of the uncertainty in each bin are produced using the baseline systematics values

$$\sigma_{ijk}^{MC} = \sqrt{\sum_m^{Evt} w_{ijkm}^2} \quad (8.21)$$

This uncertainty is assumed to be approximately Gaussian. The event rate in each bin of each simulation template is then varied using a Gaussian distribution using the expected rate as the mean and  $\sigma^{MC}$  as the uncertainty. The new templates are then summed together and each bin is fluctuated around the new expectation assuming Poisson statistics, creating a representation of one possible realization of the data in the analysis. The OscFit minimization then proceeds as described in the Asimov case using each of 500 realizations of pseudo-data, with the calculation of the  $\Delta\chi^2$  as described in ??.

The Brazilian flag shows the  $1\sigma$  and  $2\sigma$  range of  $\Delta\chi^2$  values around the median at each value of  $N_{\nu_\tau}$ . This provides a graphical representation, shown in , of the expected range of variation of the sensitivity given solely statistical uncertainties.

brazilian flag

### 8.5.3 Feldman-Cousins vs Wilk's Theorem

Estimates of the sensitivity of the analysis were performed using a theorem by Samuel S. Wilks [89]. The theorem gives a statement about the distribution of the likelihood ratio when the likelihoods form a "nested model". The nested model indicates that the fit parameters used in one fit,  $H_0$ , form a subset of those used in another fit,  $H$ . if the two likelihoods that go into the likelihood ratio differ by  $N$  parameters, Wilk's theorem states that the distribution of the test statistic  $-2\ln\left(\frac{L}{L_0}\right)$  will asymptotically approach a chi-squared distribution with  $N$  degrees of freedom.

Wilk's theorem is a powerful tool that may be used to estimate the significances of results and is widely used. In the case of the measurement of  $\nu_\tau$  appearance, fits are performed twice in order to obtain the likelihood ratio: once with the value of  $N_\tau$  fixed to various points and once with  $N_\tau$  freely floating. The likelihood ratio is then calculated at each fit point relative to the overall best-fit likelihood using Equation ??.

These two fits form a nested model with  $N=1$ , allowing the application of Wilk's theorem to estimate significances.

Wilk's theorem gives a useful estimate of the significance and requires negligible additional computational power. However, the theorem states only an asymptotic limit. Evaluation of the applicability of Wilk's theorem requires a more robust analysis using Monte Carlo trials.

A more thorough procedure, introduced by Gary Feldman and Robert Cousins [90], may be applied instead. Instead of assuming a number of degrees of freedom, the Feldman-Cousins procedure requires directly using the test statistic distribution in order to evaluate the significance. For public IceCube oscillation results, a method similar to the procedure by Feldman and Cousins is used.

To begin, a value of  $N_\tau^{True}$  is selected. Monte Carlo trials are produced with this true value and the likelihood ratio between the best-fit value of  $N_\tau$  and  $N_\tau^{True}$  for each trial is calculated. The distribution of the likelihood ratios is used to identify the value of  $(\Delta\chi^2_{FS})$  below which  $P_{i=1\sigma}(\Delta\chi^2_{FS}) \approx 68.2689\%$  of trials lie. This value is interpreted as the  $1\sigma$  level for the chosen value of  $N_\tau^{True}$ . The procedure may be repeated for each required value of  $N_\tau^{True}$  and different significance levels  $i$ .

Examples of the likelihood ratio distribution for various values of  $N_\tau^{True}$  are shown in Figure ??.

A  $\chi^2$  distribution with 1 degree of freedom is overlaid, showing the expected distribution assuming Wilk's theorem. The difference in the 90% level from Wilks (green) and Feldman-Cousins (red) is also shown. In general, the distributions show a preference for a slightly narrower distribution than expected from Wilk's theorem. The difference indicates that the Wilk's theorem approximation may be inaccurate and that the Feldman-Cousins procedure is necessary to correctly characterize the final result.

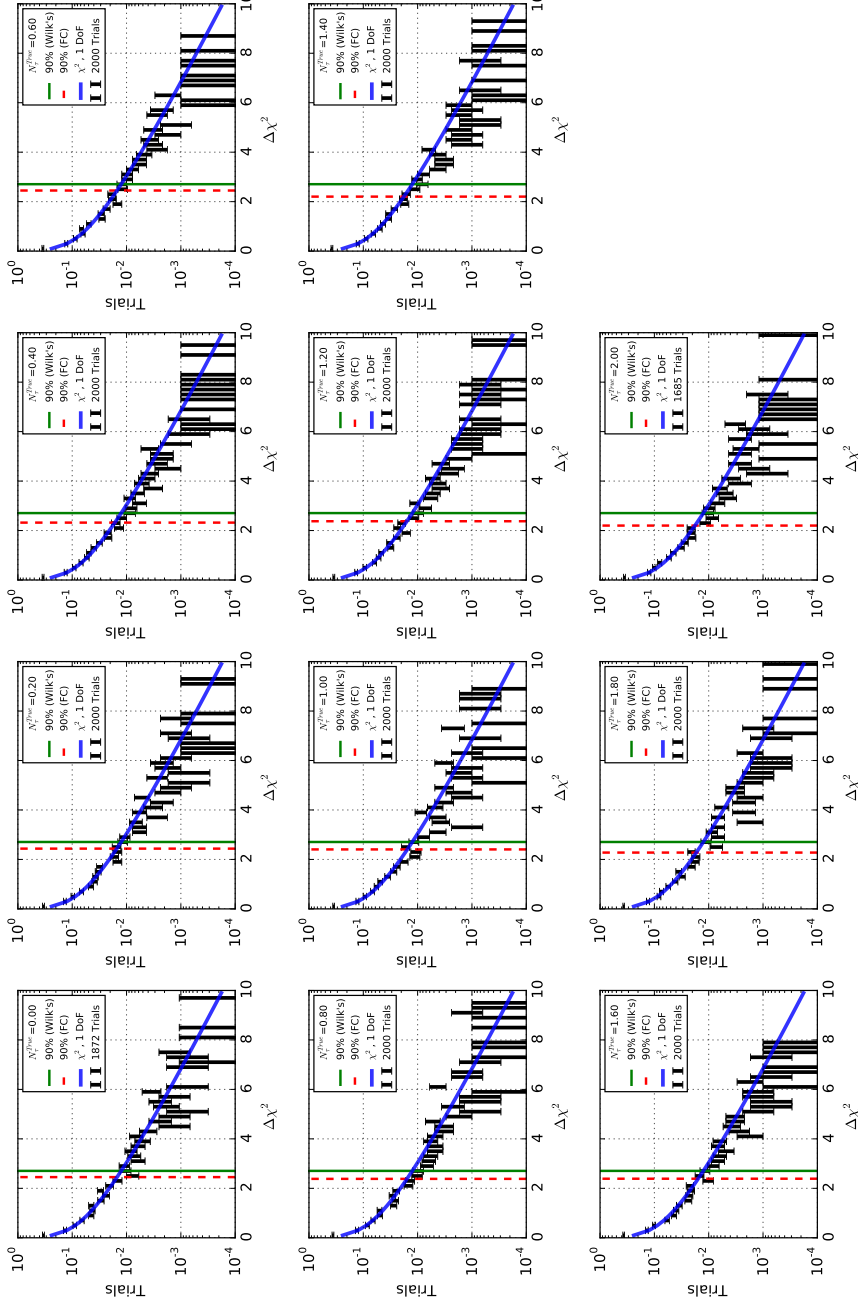


**Figure 8.2** – The test statistic distributions for 11 points in  $N_\tau^{True}$  in the NC+CC fit. The assumption of 1 degree of freedom from Wilk’s theorem is tested by looking at the location of  $(\Delta\chi_{FS}^2)_{90\%}$  for each point. The distribution calculated from Monte Carlo trials is narrower than that predicted by Wilk’s theorem, indicating that a more complete treatment with the Feldman-Cousins procedure is necessary.

Once each significance level is obtained for all values of  $N_\tau^{True}$ , a fit to data is performed. The final confidence intervals at level  $i$  are obtained by finding the crossing points between the data contour and the limit obtained for  $P_{i=1\sigma}(\Delta\chi^2_{FS})$ , here referred to as  $(\Delta\chi^2_{FS})_i$ . The evaluated  $(\Delta\chi^2_{FS})_i$  are limited to the discrete values chosen in  $N_\tau^{True}$ . In order to obtain a continuous model, the values of  $(\Delta\chi^2_{FS})_i$  and the contour from data are splined using the UnivariateSpline from Scipy [88]. The crossing points of the two splines may then be calculated to obtain the best estimate for the final result.

The procedure does not rely on assumptions about the test statistic distribution and works even in cases where the likelihood ratio distribution does not chi-squared distributed. The number of trials required to reduce the effect of statistical fluctuations in the evaluation, however, can make such evaluations prohibitively expensive. In order to evaluate the 90% confidence interval at 10 points from  $0 \leq N_\tau^{True} \leq 2$  with minimal fluctuation requires on the order of 1000 trials at each point. Higher significance levels may increase the number of trials required exponentially. Each of these 10,000 trials must be fit a total of four times: each combination of  $N_\tau$  free/fixed and each of the two octants in  $\sin^2\theta_{23}$  must be tested separately. The procedure must be run separately for the CC-only and NC+CC fits, doubling the computational resources required. At approximately one hour per fit, this leads to a requirement of approximately 10 CPU-years worth of computing power. Any changes to the analysis, including additional cuts and systematics changes, may lead to differences in the values of  $(\Delta\chi^2_{FS})_i$ . In order to reduce the total computation power required for tests in this analysis, the full Feldman-Cousins procedure as described here was only applied once the final result was unblinded. Until that point, all significances were calculated assuming Wilk's theorem.

### 8.5.4 Impact of Systematics

There are various ways to measure the impact of the included systematics in this analysis. Described here are methods to evaluate, in order of increasing importance, the total systematics impact, the impact of each systematic individually, the correlation between systematics, and the effect of non-baseline values. Each of these test different aspects of the sensitivity and all are included for completeness.

#### Total Systematics Impact

The total impact of the systematics on the sensitivity may be measured by comparing the total Asimov sensitivity to an Asimov sensitivity calculated using no systematics. This is shown in . It is clear from the comparison that the analysis is very sensitive to the included systematics set.

comparison of stat-only fit to full systematics fit

#### N+1 Tests: Sensitivity of Analysis to Systematic

A different test is also possible: Instead of calculating likelihoods with no systematics included, a single systematic may be used at a time. This test, called an N+1 test for the addition of one systematic at a time, yields useful information on a sample's sensitivity to single systematics. A small change in sensitivity between the no-systematics case above and an N+1 Asimov sensitivity may have two possible explanations. The first that the current analysis is unaffected by changes in the systematic, implying that the systematic may be investigated for removal in the analysis. The second possibility is that the systematic may interact with other parameters in order to produce an effect. The second case is more difficult to diagnose, but further tests may be possible.

N+1 tests

## N-1 Tests: Redundancy Between Systematics

In contrast to the N+1 tests, N-1 tests start with the full suite of systematics included. One systematic is then fixed to the baseline value and removed before redoing minimization. The change in the contour as a result of the removal of systematics allows for the investigation of redundancy between systematics. If, for example, two systematics have similar effects in the final histogram, then the N-1 test will show no change in sensitivity due to the removal. It is also possible that the analysis is strongly sensitive to the value of the systematic and is unlikely to move from the baseline value. These tests can be useful in identifying redundant parameters for removal, although with the caveat that combinations of parameters are not tested. After removal of multiple redundant parameters, the updated Asimov sensitivity should be tested once again to verify that the combination of removed parameters remains irrelevant for the fit

N-1 tests

## "Hidden Potential" Tests: Non-Baseline Values

Both the N+1 and N-1 test suffer from a particular flaw. Both fail to test the analysis for exceptionally strong sensitivity to particular systematics. In order to identify these parameters, the "hidden potential" test has been proposed. In this test, the Asimov sensitivity of the full analysis containing all proposed systematics is used as a baseline. Each systematic is then fixed, one at a time, off of the baseline value before rerunning the minimization. The parameters with priors tend to be fixed to one standard deviation from the prior mean. The change in the sensitivity gives an indirect measure of the strength of the systematic effect in the analysis. If no change is observed, the parameter is likely to be redundant and may be investigated for removal from the analysis.

hidden potential martin  
n-1 tests

## 8.6 Fitting Data

Icecube analyses are developed blindly in order to minimize bias. This proceeds in a few distinct stages, each described separately here.

### 8.6.1 Burn Sample Fits: Testing the Fitting Code

Analyzers are initially restricted to a small fraction of the full dataset while developing the event selection and fitting codes. The size of the burn sample, here limited to 1% of the total dataset, is selected in order to provide reasonable statistics while maintaining limited sensitivity to the final physics parameters. Once end-to-end tests are completed using solely simulated events, this small sample, known as the *burn sample*, is fit in order to verify that results obtained are reasonable.

### 8.6.2 Blind Fits: Checking the Goodness-of-Fit

Once the burn sample tests are complete, the next stage is to perform what is known as a *blind fit*. The concept, developed for oscillation analyses in IceCube, exists as an intermediate stage between the low-sensitivity burn sample tests and the final fit. Unlike the burn sample fits, the blind fits use the full data sample for testing. All systematics are included in the fit as normal. The final physics parameters, in this case the oscillation parameters and the  $\nu_\tau$  normalization, are allowed to fit freely, but the final results are obfuscated. The goodness-of-fit and systematics values are free for investigation.

should i be including  
the dropped dis/theta13  
systematics here? and  
maybe deltacp? otherwise  
this section feels a  
bit pointlessmay just remove the  
burn sample crap. its  
so out of date that its  
too weird to go back and  
redo it.blahdy blahdy blahdy.  
no point spending time  
here if i may just kill it

Analyzers are free to move onto a request for full unblinding if the goodness-of-fit exceeds 5%. If the goodness-of-fit is significantly lower than this limit, the sample and fit is investigated further to identify any potential issues or oversights. The blind fit is a test designed to look for problems prior to full unblinding in order to implement necessary fixes while remaining blind to the effect on the final result.

The goodness-of-fit, known more informally as the p-value associated with the fit, may be calculated via two closely-related methods. An ensemble of Monte Carlo trials is fit and the resulting  $\chi^2_{FS}$  values are used. The fraction of trials with  $\chi^2_{FS}$  larger than that observed in data gives the first p-value. The second method uses SciPy to fit a  $\chi^2$  distribution. The p-value may then be calculated from the continuous distribution by finding the total probability of observing a fit with a  $\chi^2_{FS}$  value equally or worse than the data fit,  $P_2(\chi^2_{FS} \geq (\chi^2_{FS})_{Data})$ .

scipy

The first method generally will yield more accurate results, particularly if the resulting distribution is poorly fit by a simple  $\chi^2$  distribution. If the fit is particularly poor, a large number of trials may be necessary in order to calculate an accurate p-value. In these cases, the second method may be used to provide an estimate of the p-value of the fit. During the first work with blind fits, this analysis used a wide range of reconstructed energies, including events up to 800 GeV in order to better constrain systematics terms in the non-oscillating higher energy regions. Blind fits in the GRECO analysis initially showed significant disagreement between the data and simulation, with a goodness-of-fit of  $10^{-7}$ . Investigations yielded new discoveries about both the calibration of the Monte Carlo simulation and previously-unknown erroneous events in the data.

## Disagreement in Charge Templates

Continuing problems with the goodness-of-fit led to still more unique discoveries using the GRECO sample. While checking variables, significant disagreement was discovered in numerous charge variables. A proxy for the most fundamental variable, the average charge per hit DOM, shown in , shows systematic disagreement between the simulated events and all years of detector data.

q/nch at L7

The first suspected cause was the erroneous splitting of waveform pulses in the WaveDeform charge extraction module. The expected charge from a single incident photoelectron is used in WaveDeform to convert the digitized waveforms from the FADC and ATWD into reconstructed photoelectrons consisting of charge and timing information. While the simulated response is known exactly, the associated charge response of the DOM in data requires careful calibration. Using a mismodeled charge response to extract pulses in the data can result in single photoelectrons being erroneously split into multiple smaller reconstructed pulses. Potential mismodeling effects of the charge extraction were checked in ???. In these figures, the charge of each individual pulse is shown as a function of the arrival time, which is normalized to the time of the largest extracted pulse in the DOM for each event.

wavedeform?

Significant disagreements between the data and simulation are visible. The erroneously split pulses are visible in data as a low-charge tail from t=0 until t=50 nanoseconds. In addition to this effect, however, many other regions of disagreement are visible. In data, there appear to be a significant number of prepulses not visible in the simulation occurring between t=-50 and t=-20 nanoseconds. The structure of the late pulses, appearing with approximately 0.4 PE of charge and at time t=30 nanoseconds also

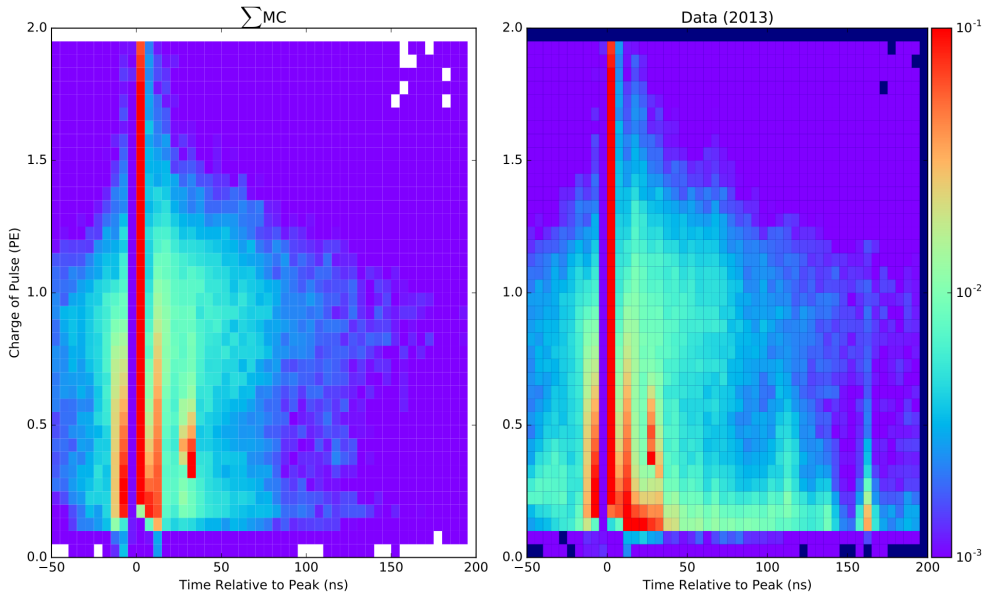


**Figure 8.3** – A comparison of the charge extraction in data and simulation at GRECO L7. Both the time and charge are shown for individual pulses on all DOMs. The time is measured relative to the largest pulse observed on each DOM during an event. The data and simulation histograms are independently normalized to 1.0. While the two show broad agreement, notable differences occur at low charge.

appears notably different between the data and simulation. A final set of pulses, occurring at 160 nanoseconds, also appears to be unsimulated. This timing structure requires additional calibration resources to identify and better simulate, the scope of which is beyond this work. Regardless, the presence of unsimulated features indicates that at least some charge information in the simulation is unreliable.

The absence of features led to investigations of the charge produced in PMTResponseSim module of DOMLauncher. In the module, photoelectrons at the photocathode of the PMT are propagated through the dynodes to the anode. The resulting output, a series of pulses emitted from the PMT to be passed onto the simulation of the DOM discriminator and digitization processes, requires a conversion from the number of raw incident photoelectrons to a total charge profile in the form of a waveform. The conversion, known as the *single photoelectron template*, or *SPE template*, is calculated from calibration measurements performed prior to deployment of the DOMs in the ice . The SPE template, used for all DOMs, has been known to vary somewhat between DOMs in a lab setting for many years, but the problem was deemed unimportant given other ongoing calibration work.

With the identification of the issue using the GRECO event selection, new efforts were dedicated to the production of in-situ measurements of the SPE templates for each DOM. These new template are entering production as of the time of this analysis, but the time required for newly updated simulation is prohibitive. Other methods are therefore necessary to avoid introducing spurious systematic biases into the final results.

In order to attempt to characterize the expected effect due to the change in the SPE templates, a new method of reweighting was developed with the GRECO selection. The average charge per DOM,  $\bar{q}$ , is shifted by a known amount,  $\Delta\bar{q}$  and binned. The ratio of the shifted and unshifted average charge histograms is calculated. An example of this

TA003 charge template

process for the  $\nu_\mu^{CC}$  is shown in . This process is performed for various values of  $\Delta\bar{q}$  and the resulting ratios are splined using the SciPy splining function `RectBivariateSpline`, yielding a continuous function describing the change in the number of events at each charge as a function of  $\Delta\bar{q}$ . This spline, an example of which is shown in , may be evaluated for each event by providing the values of  $\bar{q}$  of the given event and the  $\Delta\bar{q}$  requested. The output is interpreted as a rescaling factor for the event weight.

This process, referred to as *MC charge rescaling*, has limitations. In particular, threshold and selection events are completely ignored in this formulation. A changed charge response of the detector acts roughly as a DOM efficiency shift, discussed in ??, which may lead to significantly different numbers of atmospheric muon background events reaching final level. The average charge per DOM is also potentially a poor proxy if the variation in the SPE templates for each DOM is large. Still, this process provides an estimate of the potential effect that such a correction may induce in the final event selection. These effects are calculated and applied per-flavor, resulting in changes such as that shown in .

In order to verify the method, various sets of detector data were used. Beginning with IC86-5 in the 2015-2016 operating season, the SPE templates used in the detector data were adjusted, leading to an approximately 4.5% average shift in the expected charge. This dataset therefore provides a known effect very similar to a recalibration of the SPE templates in Monte Carlo when compared to previous years of detector data. The procedure described above was applied to the IC86-5 detector data and a  $\chi^2$  was used to find the best-fit charge rescaling to match the IC86-2, -3, and -4 datasets. In tests, the average expected shift between the datasets was recovered in each case, although the limitations of the method prevented a particularly strong statement about the goodness-of-fit. This is expected due to the expected differing atmospheric muon background contributions between the earlier seasons and the IC86-5 data.

With the verification successful, the MC charge rescaling was included as a continuous systematic in `OscFit` to evaluate the change in the goodness-of-fit. Performing the blind-fit checks, the total goodness of fit was evaluated, showing a large improvement in fit quality. The best-fit value of yielded a change in the goodness-of-fit of . This indicated that the MC charge rescaling could explain at least part of the disagreement observed between the data and Monte Carlo.

Due to the limitations observed in the calculation of the charge rescaling as well as the previously discussed disagreements in the simulated charge features, a decision was made to attempt to exclude the charge information from the analysis. No changes were mandated to earlier selection levels, which showed reasonable reasonable agreement between data and Monte Carlo simulation. Instead, this resulted in a change to the reconstruction likelihood space, excising the charge in favor of a simplified hit/not-hit model described in ?? . All events were reconstructed with the newly updated PegLeg reconstruction and the blind fits were reproduced. The removal of charge information from the fit led to a significant improvement of the goodness-of-fit relative to the original blind fits on par with the introduction of the MC charge rescaling, which was made partly obsolete.

## Discovery of Flaring DOMs

Initial investigations into the poor fits in data led to comparisons of the data and Monte Carlo in various reconstructed quantities believed to be independent of the expected signal. The decision was made to investigate these quantities using the simulation weights

example of shifted and unshifted charges for eg numu

scipy rectbivariate spline

2d splines for mc charge scale correction

systematic effect of mc charge scale

figure 4.2.3 from my wiki

find the best-fit of the mc charge scale

what was the change in the pvalue from the mc charge scale?

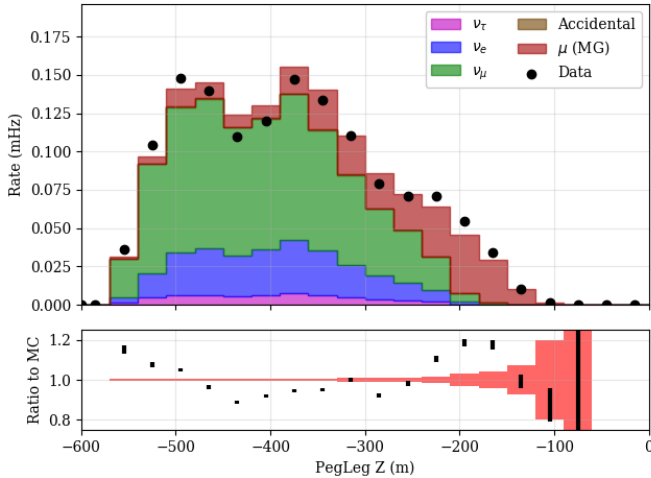


**Figure 8.4** – The reconstructed Z position using PegLeg. The GRECO L7 cuts have not been applied in order to show discrepancies below the detector. Noticeable disagreement is seen around a depth of  $z=-450$ .

calculated with the baseline values. Past experience has shown that the uncertainties in the ice model can lead to significant disagreements. Existing uncertainties on the bulk ice assume that the coefficients for all ice layers are fully correlated. In practice, it is possible that the ice model coefficients in parts of the detector are more poorly modeled than others. By looking at the event rate in data and simulation as a function of the depth and position in the detector, discrepancies in the ice model can be identified.

The initial plots are shown in ???. A significant difference is observed at a depth of around  $Z \approx -400$ . Checks performed with other samples have shown similar disagreements at these depths, indicating disagreement in the ice model. Previously unblinded oscillation samples showing this issue have not observed significant issues in the goodness-of-fit. New ice models are underway with dedicated work to fix this region is underway.

Two-dimensional histograms of the depth and radial distance also show systematic disagreement in some regions, as shown in ???. These excess events appear to occur on string 83, shown in ???, indicating an effect occurring due to the DOM hardware in the detector. Follow-up work has shown that these DOMs, known here as *flaring DOMs*, appear to spontaneously emit light for unknown reasons. The light output is identifiable both based on the position of the hits and the amount of charge observed in nearby DOMs. These spurious events, first discovered in the GRECO selection, have since spawned dedicated searches to better understand spontaneous light emission from the DOMs. A small handful of DOMs have been identified by these searches with emission times as frequent as 1 Hz .

internal search for flaring doms

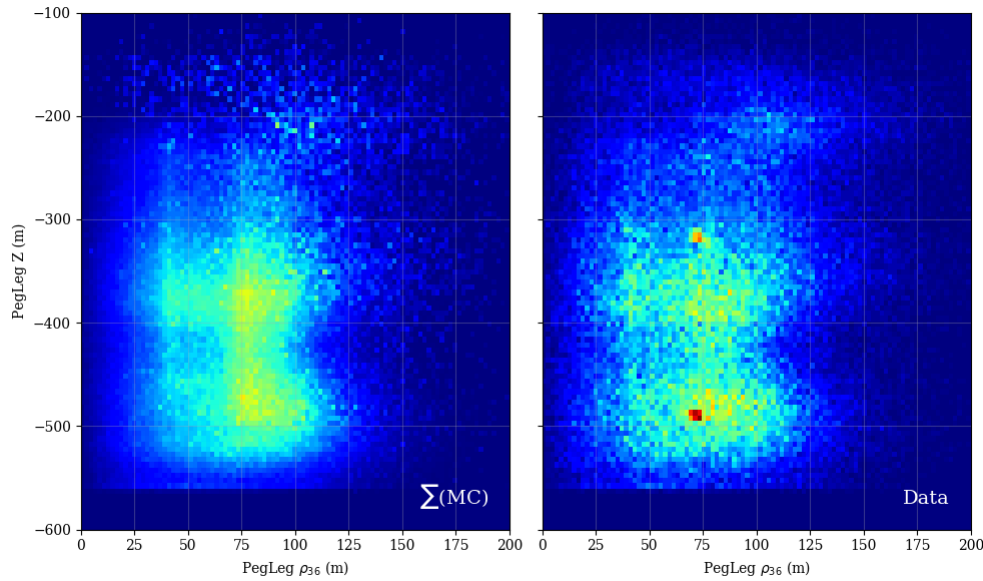


**Figure 8.5** – The reconstructed Z position plotted against the reconstructed distance from string 36. The L7 cuts from GRECO have been removed for this plot. The colorbars in both plots have been normalized to be identical. The data and simulation show reasonable agreement except for two points in the data, near  $\rho_{36} = 75$  at depths of -310 and -490.

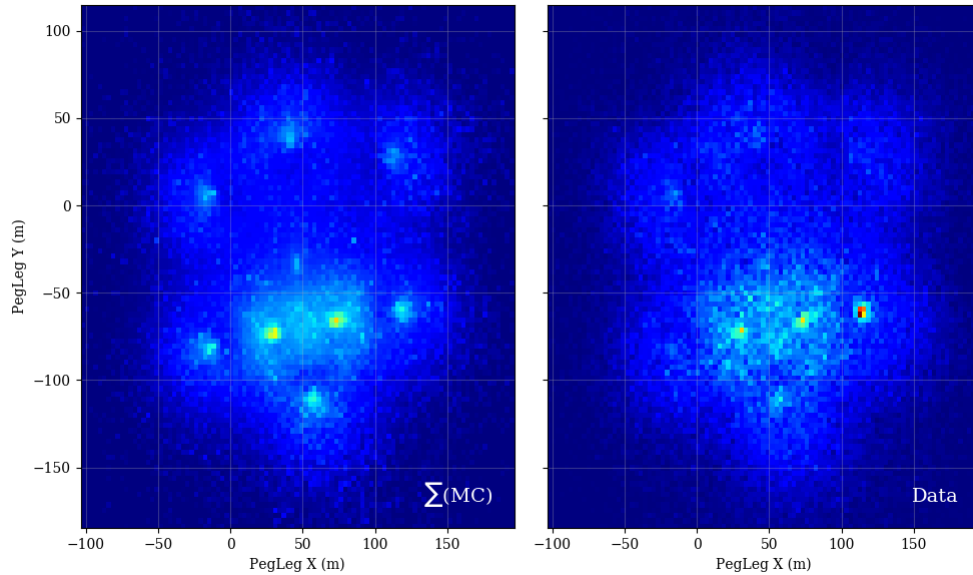


**Figure 8.6** – The reconstructed X position and Y position of events in the detector. The L7 cuts from GRECO have been removed for this plot. The colorbars in both plots have been normalized to be identical. Once again, reasonable agreement is observed in most regions, although data events have a clear excess near  $x=110$  m,  $y=-60$  m. This position corresponds to string 83.

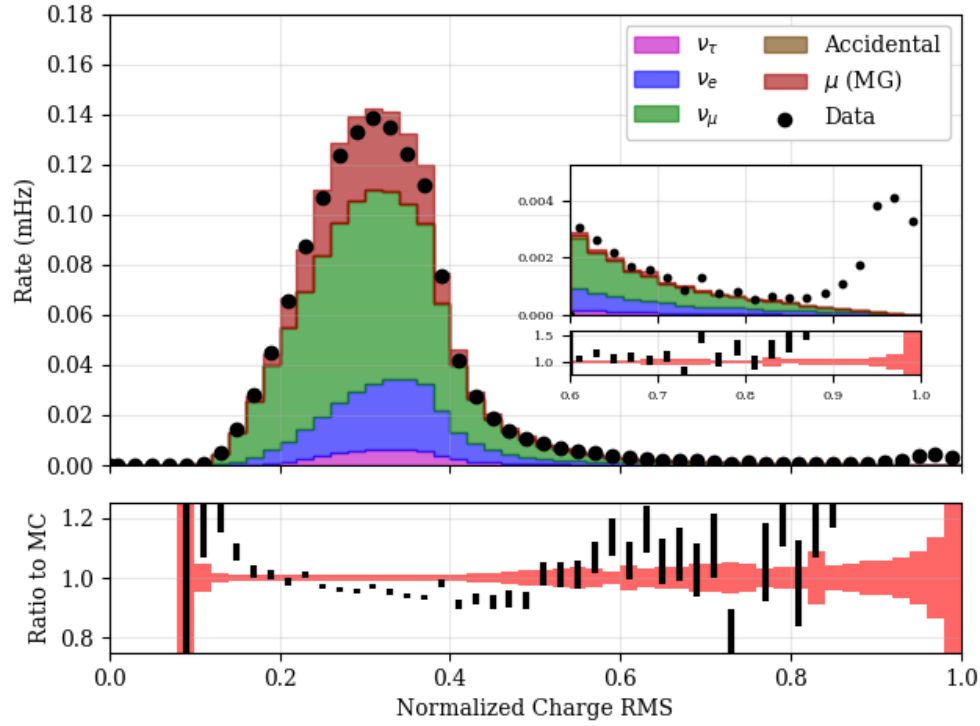


**Figure 8.7** – The RMS of the charges within each event at final level. The value of the RMS is normalized using the total charge observed. The L7 cuts from GRECO are not applied here. The events with flaring DOMs cluster at high values of the charge RMS, visible in the inset.

The affected events may be identified based on the charge profiles. In particular, DOMs directly adjacent to the emitting DOM observe a significant fraction of the total charge of the event. This may be characterized using the 'charge RMS' of the event.

$$q_{RMS} = \frac{\sigma_q}{\sum_{hits} q_i} \quad (8.22)$$

This is shown in . Events with a  $q_{RMS} > 0.85$  are removed from the analysis, removing the most obvious spurious events. A total of events are removed from the GRECO data, resulting in a total reduction of %. The removal of these events in data and simulation does not significantly impact the goodness-of-fit of the sample due to the low event rates involved.

## Simulation of Bedrock

Additional disagreement was observed in the reconstructed Z position. Near the bottom of the detector, a clear excess of events in data indicated a mismodeling in the simulation. This disagreement increased below the detector, shown in . Notable disagreement was also discovered in the reconstructed energy, shown in . Events interacting below the detector may have significantly higher energies than the reconstructed energy due to the lack of instrumentation, indicating a possible connection between these two discoveries. In the GRECO selection, events with energies above 1 TeV are modeled using NuGen simulation in order to account for events not properly simulated in the GENIE generator.

Previous investigations have shown that the two generators use similar models of the cross-section and return similar event rates at low levels. Still, the events from the NuGen generator were shown to make up a significant fraction of the high energy tail in the GRECO sample. These events were therefore checked for potential issues.

The NuGen and GENIE simulated event samples are used in the GRECO analyses in non-overlapping phase spaces. The simulations do include overlapping regions, however. For the purposes of testing, the full sample of GENIE and NuGen events were compared in true and reconstructed energy and Z position. Initial work comparing the overlapping energy range of NuGen and GENIE events contained within the DeepCore fiducial volume showed little apparent disagreement.

Removing the constraint on the event containment, however, led to the discovery shown in . The two generators show broad agreement until a depth of approximately -830 meters, corresponding to the interface between the Antarctic glacier and the underlying bedrock. The difference is visible in the overlapping energy range of 100 GeV to 1 TeV. Further checks discovered the issue in IceCube's implementation of the GENIE generator. When calculating the interaction probability for the neutrino interactions, the density of material is included. In the implementation of GENIE previously used by the IceCube collaboration, events were assumed to occur solely within or near the fiducial volume of DeepCore due to the low energies involved. The bedrock was therefore deemed unnecessary and not implemented in favor of assuming a uniform density of ice throughout the simulation volume. During initial implementation, the GENIE generator was planned for use up to 100 GeV due to technical limitations. Later work expanded this range up to 1 TeV with future work ongoing to push toward 10 TeV. The problems with the bedrock were mistakenly overlooked during the upgrades of the generator, leading to the systematic disagreement shown in .

The bedrock has been properly included in both the NuGen generator as well as the PROPOSAL module for propagating the charged leptons. GENIE events therefore suffer solely from an incorrect interaction probability due to the discovered bug. The density of interaction medium enters as a linear term in the interaction probability, indicating that a correction of the form  $\rho_{\text{rock}}/\rho_{\text{ice}}$  is sufficient to correct the Monte Carlo. The fixed distributions in energy and zenith are shown in .

In order to limit other potential issues from the bedrock, the analysis space was further limited, removing events both at higher energies ( $E_{\text{reco}} > 56\text{GeV}$ ) and those reconstructing at or below the bottom of the detector ( $Z_{\text{reco}} \leq -500$ ). These cuts significantly reduce the size of the sample by reducing the high energy events included at final level. These changes have some impact on the expected sensitivity, but were deemed necessary to minimize the potential impact of systematics issues associated with the NuGen sample and, more broadly, limitations in the simulated event samples interacting below the detector.

reco z of overlapping events in nugen and genie showing the bedrock problems

reference the reco z plot showing bedrock issues again

energy and z distributions after reweighting genie bedrock events

these updates with event rates should be lines on a data/mc rate table in the selection section.

PDFs for gof

## 8.7 Results from the Search for Appearance

After the removal of the flaring DOM events, the correction of bedrock events, and the elimination of the charge in the PegLeg fit, a new blind fit was performed and the goodness-of-fit was again tested. The resulting  $\chi^2_{FS}$  for the charged-current only and neutral-current + charged-current fits were 127.095 and 127.623 respectively. One thousand trials were run for each fit using the updated sample, yielding estimates of the probability density function shown in . The data is well-described by the systematics set, with a pvalue of approximately 57% for both fits. The full map of the  $\chi^2_{FS}$  values is

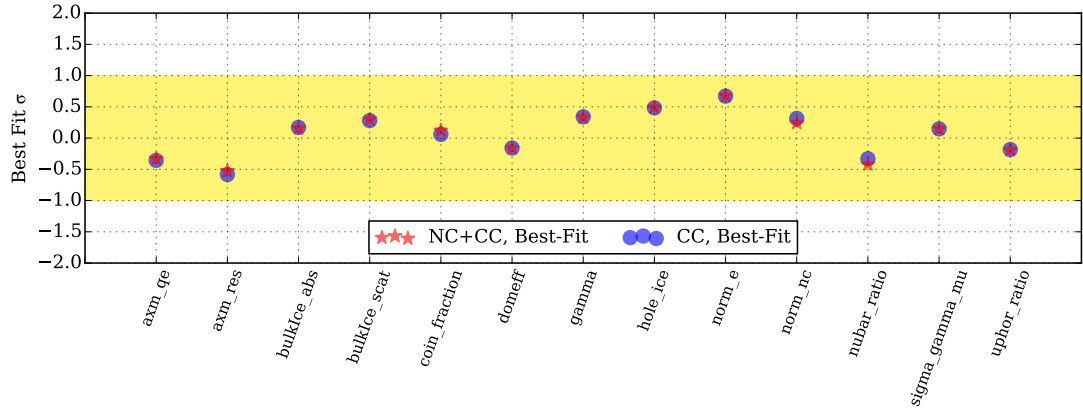


**Figure 8.8** – The value of each systematic with priors. The best-fit values are shown for each while the priors are shown by the yellow band. The CC and NC+CC fits are highly correlated, as expected, with very little difference in the systematics best-fit values. All values fit well within the expected  $1\sigma$  ranges.

shown in Figure ???. No single region of disagreement is visible, indicating that there are no significant remaining unmodeled systematic uncertainties.

With the observation of good fit p-values, the final results for both the CC-only and NC+CC fits were fully unblinded. Both results, shown in Figure ?? and Figure ??, fit lower than expected from unitary 3-flavor oscillations, although both are consistent with such a model.

The final value of the systematics, shown numerically in Table ?? and graphically in Figure ??, are within  $1\sigma$  of the expectation at the best-fit points. Many systematics were expected to be determined primarily from the data instead of from priors. Figures ?? and ?? shows the expected values of each systematic for 1000 trials. The shaded band shows the assumed  $1\sigma$  prior range for each of the parameters, if present. Not only are all systematics within the relevant priors, but most systematics fit within the expected posteriors.

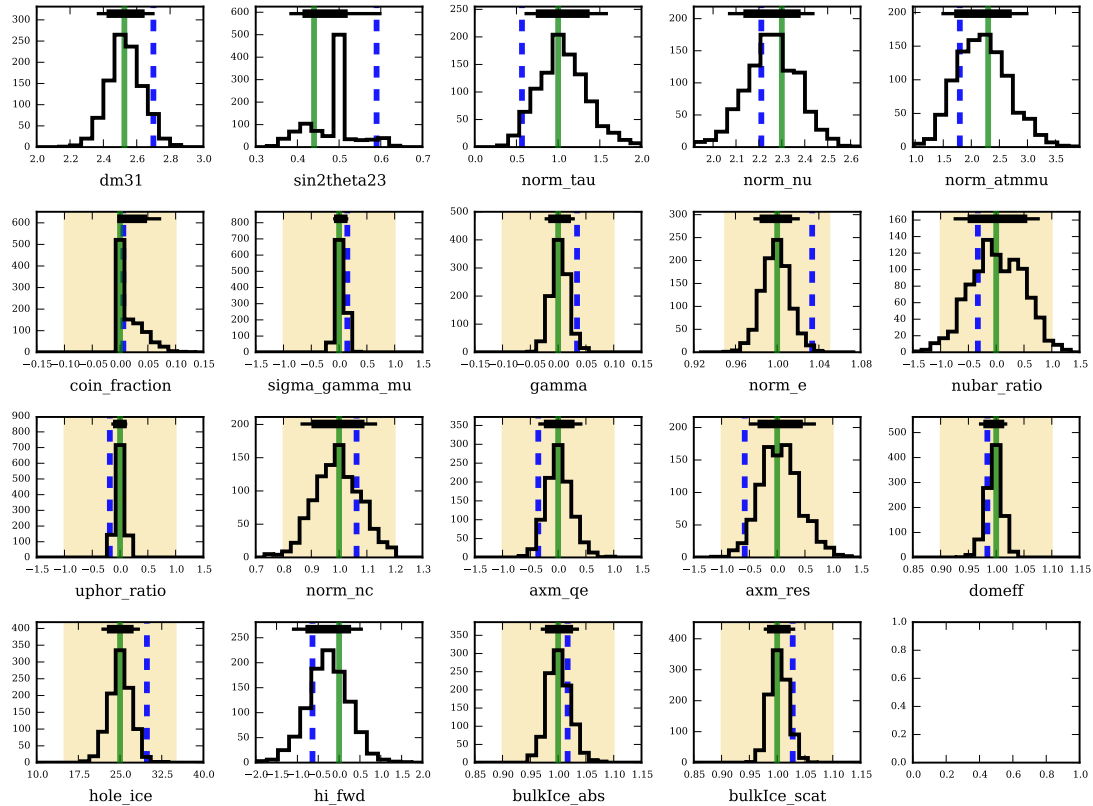


**Figure 8.9** – A comparison of the posterior expected from trials to the final data fit value for each parameter for the CC-only fit. The trials used to build the posterior distribution in each parameter assume baseline values for systematics,  $N_\tau^{CC} = 1$ , and Nu-Fit 2.2 values [57]. The green vertical line shows the true injected value. The blue dotted line shows the best-fit value from data. The black bar shows the  $1\sigma$  and  $90\%$  ranges calculated from the posterior distribution.

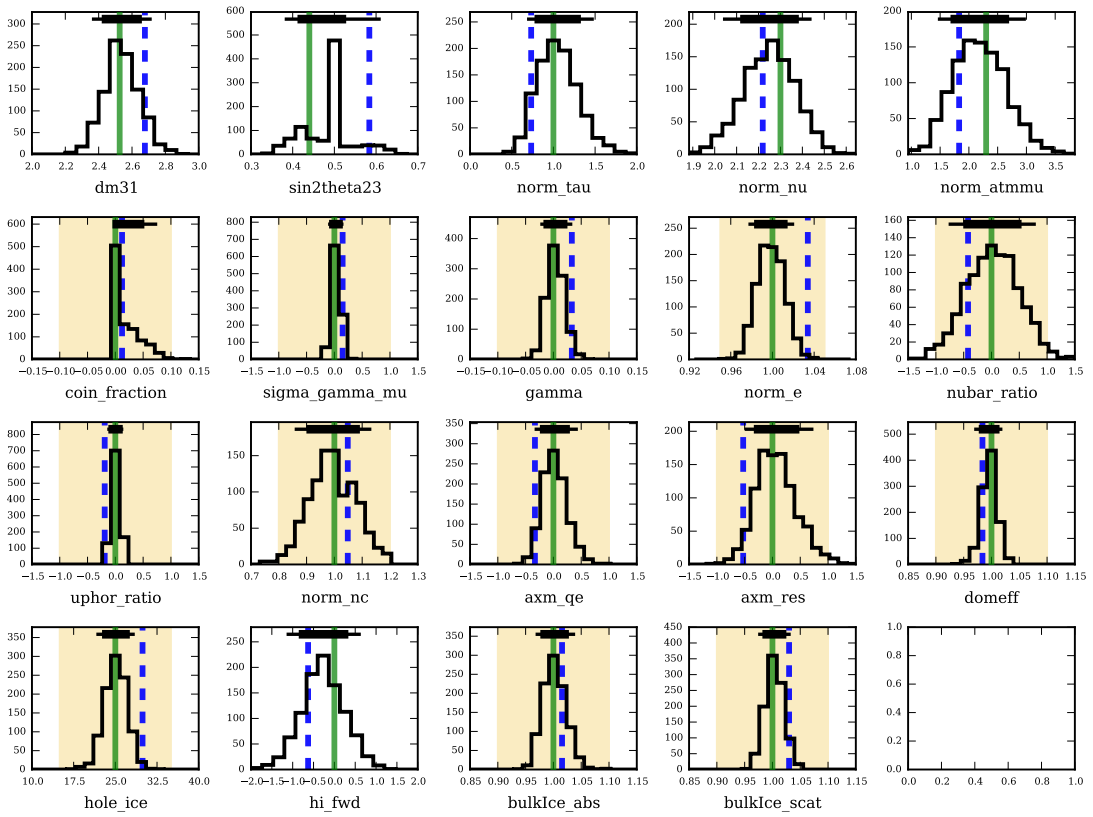


**Figure 8.10** – A comparison of the posterior expected from trials to the final data fit value for each parameter for the NC+CC fit. The trials used to build the posterior distribution in each parameter assume baseline values for systematics,  $N_{\tau}^{NC+CC} = 1$ , and Nu-Fit 2.2 values [57]

Parameter Type	Fit Parameter	Units	Prior	Disappearance	Appearance	
					CC-Only	NC+CC
Oscillations	$\Delta m_{32}^2$	$10^{-3} \text{ eV}^2$	-	2.548	2.625	2.602
	$\sin^2(\theta_{23})$	-	-	0.576	0.590	0.584
	$N_\tau$	-	-	1.0 (Fixed)	0.566	0.733
Cross-section	Axial Mass (QE)	$\sigma$	$0 \pm 1.0$	-0.250	-0.357	-0.332
	Axial Mass (RES)	$\sigma$	$0 \pm 1.0$	-0.3737	-0.583	-0.526
	$N_{NC}$	-	$1 \pm 0.2$	1.016	1.063	1.048
Neutrino Flux	$\nu_\mu$ Norm	Years	-	2.151	2.210	2.219
	$\nu_e/\nu_\mu$	-	$1 \pm 0.05$	1.031	1.034	1.033
	$\gamma_\nu$	-	$0 \pm 0.10$	0.045	0.034	0.033
	$\nu/\bar{\nu}$	$\sigma$	$0 \pm 1.0$	-0.700	-0.330	-0.422
	Up/Hor	$\sigma$	$0 \pm 1.0$	-0.207	-0.184	-0.191
	$f_{Coincident}$	%	$0 + 0.1$	0.027	0.006	0.012
	$\mu$ Norm	Years	-	1.845	1.795	1.830
Muon Flux	$\gamma_{CR}$	$\sigma$	$0 \pm 1.0$	0.113	0.148	0.148
	DOM Efficiency	-	$1.0 \pm 0.1$	0.980	0.984	0.984
	Hole Ice (Flasher)	-	$25 \pm 10$	30.526	29.833	29.894
	Forward Scattering	-	-	-0.839	-0.638	-0.630
	Absorption	%	$1.0 \pm 0.1$	1.014	1.017	1.016
	Scattering	%	$1.0 \pm 0.1$	1.033	1.028	1.030

**Table 8.6** – The best-fit systematics values for each nuisance parameter in the fit. The corresponding parameters for  $N_\tau = 1$  (ie, the disappearance fit) are included for reference. The CC-only and NC+CC fits are highly correlated, as expected.

## 8.8 Complementary Measurements from This Analysis

### 8.8.1 Oscillation Parameters

Thanks to significant contributions from others , dedicated measurements of the atmospheric mixing parameters have also been performed using the GRECO selection. In these measurements, the value of  $N_{\nu_\tau}$  remains fixed to unity. The derived results are therefore directly comparable to results from other oscillation experiments.

#### $\nu_\mu$ Disappearance Results

Using similar tools as the appearance analysis, a complementary search for  $\nu_\mu$  disappearance was performed . The measurement of the disappearance parameters,  $\Delta m_{3j}^2$  and  $\theta_{23}$ , used an identical choice of binning and systematics set as the appearance search described above. The  $\chi^2_{FS}$  statistic was found by minimization with the iMinuit package across a grid of values arranged linearly in  $\Delta m_{3j}^2$  and  $\sin^2 \theta_{23}$  covering both octants. At each point, the disappearance parameters were fixed during minimization. Both the normal and inverted ordering are tested separately.

The result is shown in with comparisons to previous atmospheric oscillation measurements by IceCube , Super-Kamiokande and the MINOS experiment . Results from accelerator measurements are shown from the NO $\nu$ A and T2K experiments. All results show the

90% contour around the best-fit point. The GRECO result mildly prefers the normal ordering and the second octant, although maximal mixing ( $\sin^2 \theta_{23} = 0.5$ ) is well within the best-fit contours.

The GRECO result improves upon the most recent IceCube result significantly, particularly in the measurement of the mass splitting. Both results are statistically consistent with one another, although the GRECO result prefers a larger mass splitting than the previous result. Global fits, which prefer a value of the mass splitting of  $2.494^{+0.033}_{-0.031}$  as of the time of this writing , favor the new GRECO result over the previous IceCube result. Precise measurements of the atmospheric mixing angle continue to elude us, however. While the GRECO result provides competitive constraints on the mixing angle, no significant improvement is observed.

#### Mass Ordering

In order to quantify the preference for the mass ordering, a dedicated measurement using the GRECO sample was performed . This measurement included numerous differences relative to the appearance and disappearance measurements. Only upgoing reconstructed GRECO events were included, although the energy range was extended to 3-100 GeV. All simulation templates were smoothed during the analysis using a dedicated implementation of the kernel density estimation technique implemented in the C++ programming language . This code, unlike the SciPy KDE implementation used in ??, includes functionality for weighted event samples and variable bandwidth estimation.

The systematics set used in the mass ordering analysis was identical to that of the disappearance measurement, with the value of  $N_{\nu_\tau}$  fixed to unity. Systematics included in the mass ordering measurement were applied using a parallel branch of the OscFit code used in the appearance measurement.

Statistical uncertainties arising from the simulation statistics were estimated using a bootstrapping technique included in the KDE implementation. The test statistic used in

future reference to martin, elim's theses

elim's thesis

iminuit

elim's result!

icecube 2017 result

superk 2015 oscillation result

minos oscillation with atm

nova oscillation

t2k oscillation result

nufit 3.2

martin's thesis

martin's kdes from the aachen group. who did that?

the mass ordering measurement was defined to be the numerical convolution between the Poissonian uncertainty due to the expected event count and a Gaussian model of the bootstrapped Monte Carlo statistical uncertainty.

Unlike the appearance and disappearance measurements, the neutrino mass ordering is not a continuous parameter. The calculation of a final significance proceeds following the method described in , a full description of which is beyond the scope of this work. Using GRECO events, a good fit is obtained at the best-fit point with a pvalue of approximately 80%. Using the cited technique, a weak preference for the normal mass ordering is found at approximately  $0.3\sigma$

pingu paper and/or pisa paper describing nmo measurement

Need martin's final result!

## 8.9 New Constraints on Detector Systematics

The statistics available in the GRECO dataset provide a unique chance to derive new constraints on systematic variables. For each of the parametrized detector systematics, a scan was performed to evaluate constraints from the dataset. In all cases, the value of  $N_{\nu_\tau}$  remained fixed to unity. The results of these scans are shown in .

chi2 scans of the detector systematics to show greco constraints on domeff, holece, hifwd, absorption, and scattering

These new constraints imply new, tighter limits derived from fits to the detector data. They do have limitations, however. During the parametrization process, all systematics were assumed to be uncorrelated, which is unlikely to be the case in practice. The DOM efficiency and absorption properties in the ice are known to have correlations in dedicated calibration work in the detector, for example. These correlations are included in the prior uncertainties for each parameter. Although

Each also assumes an accurate modeling of the effects in question. All effects are assumed to equally apply to the entire detector. Bulk changes of the properties associated with each systematic are assumed to be more important than the spread of uncertainties for each DOM (DOM efficiency, hole ice parameters) or layer in the ice (absorption, scattering). This assumption indicates limited insight may be gained. Testing the properties for each DOM is unlikely to be within the statistical reach of any dataset in the foreseeable future given the number of DOMs in the detector.

The new constraints from GRECO demonstrate significant power in the dataset to identify new effects like those discussed in ???. The dataset provides the collaboration with a novel set of low energy events sensitive to evaluate detector properties. These new constraints may be used in future analyses to limit systematic uncertainties affecting other measurements.

### 8.9.1 Implications and Future Work

There exist various ways to interpret the value of  $N_{\nu_\tau}$ . The value of the tau neutrino normalizations in the exclusive and inclusive channels are both consistent with the expected value of 1.0. The standard 3-flavor oscillation model is not strongly disfavored from the GRECO oscillation result. The current result does, however, provide some tension with the most recent exclusive result from Super-Kamiokande , which reported  $1.47 \pm 0.32$ . The GRECO and Super-Kamiokande inclusive results differ by approximately  $1.8\sigma$ , assuming the total uncertainties are added in quadrature. In practice, various systematics, including the atmospheric mixing angle and mass splitting, are likely correlated between the analyses, implying approximately  $2\sigma$  of tension between the two results.

change cc and nc+cc to exclusive and inclusive respectively?

superk result

Assuming Gaussian uncertainties for the two results, the simple weighted average can be calculated in order to estimate the expectation from a combined fit. This value,  $1.06 \pm 0.22$ , shows remarkable agreement with the expected value of 1.0, favoring the standard 3-flavor mixing matrix with large uncertainties. The OPERA value , which

opera result

strongly excludes the no-appearance hypothesis but little else, has a negligible effect on this average.

This analysis, like previous oscillation analyses produced by IceCube, has limitations. The GRECO selection includes only three years of detector data. The runs of data from those three years are selected using strict criteria that explicitly excludes non-standard runs, including those that are ended prematurely. These short runs are often otherwise unremarkable, but make up a significant fraction of the uptime of the detector in these years and are potentially useful for analysis. The addition of these runs may increase the total number of events in the GRECO sample by up to 15%. The addition of these events presents a simple way to improve the existing result on relatively short timescales. The three years of data may also be extended in other ways. The data was originally collected between April 2012 and May 2015. Since the beginning of this work, additional years of detector data have been collected and are awaiting analysis. These additional years of data were not included due to calibration changes in the IC86-5 season which may lead to disagreement between years. These updated calibrations have since been applied to the earlier years of detector data as well, leading to a self-consistent dataset of approximately 7 years.

The analysis of these events requires a number of upgrades to the simulation which are ongoing at the time of this work. New efforts are underway updating the simulated SPE templates (??) to better describe the charge profile observed in the detector. These new templates are fit to detector data for each DOM and are updated for each year, although the year-to-year variations have proven to be small. New signal and background simulation is therefore necessary to incorporate these upgrades. The new simulations are underway, with completion and verification expected within the coming year. If the new sets show good agreement with data, charge information may be reintroduced to the reconstruction, potentially leading to improvements in the reconstructed resolution of events.

The current GRECO selection was the first oscillation analysis in IceCube to successfully use simulated atmospheric muon background events at analysis level. The simulated livetime is too limited, at 10 months, to allow for precision measurements using the additional years of data. While the GRECO selection is efficient at rejecting these simulated muons, additional simulation efforts require vast computational resources. Future analyses will require significantly larger muon datasets in order to adequately describe backgrounds. The production of additional events for these analyses will require nearly a factor of 9 more events to reach parity between the expected number of muon events in 7 years of data and the raw Monte Carlo statistics. If only the standard simulation methods are used, this will require about 1.5 years worth of production time. While the new sets would include muon bundles, a feature not present during production of this work, the sets may still be limited outside of the DeepCore fiducial volume.

To remedy this situation, work is ongoing to further develop and standardize the work described in ???. That effort has been shown to yield significant improvements to the production time of MuonGun simulation, with a typical speedup of 3-4x for muons produced for the GRECO selection when using no DOM oversizing. This can improve to factors of 15-20x if using a DOM oversizing factor of 3. This may be a viable option for the production of various systematics sets in order to speed the production of background events. Additional improvements to the simulation efficiency are possible and will undoubtedly be investigated in the near future. Even using the improvements described here, however, large muon sets are, for the first time, viable as background models in IceCube oscillation analyses.

what's the livetime increase from loosing the GRL?

check the run dates

Improvements are not only possible in the background simulation, however. Investigations described in ?? have spawned discussions of the limitations of the current GENIE generator production scheme. While GENIE was originally planned to be used solely for very low energy oscillation analyses, the dawn of new event selections such as GRECO spanning wider energy ranges can lead to notable disagreement traceable to the generation scheme. To better describe the detector, GENIE generation must be expanded to identify unsimulated phase space necessary for further analyses. The simulation of events below the detector, in both the GENIE generator as well as in future MuonGun background simulations, must be given priority in order to explain the events occurring at the bottom or below the IceCube detector.

# Bibliography

- [1] H. Becquerel. "Sur les radiations émises par phosphorescence". In: *Comptes Rendus* 122 (1896).
- [2] J Chadwick. "Intensitätsverteilung im magnetischen Spectrum der  $\beta$ -Strahlen von radium B + C". In: *Verhandl. Dtsc. Phys. Ges.* 16 (1914), p. 383.
- [3] W. Pauli. *Offener Brief an die Gruppe der Radioaktiven bei der Gauvereins-Tagung zu Tübingen*. ETH Zürich, 1930.
- [4] C. L. Cowan Jr., F. Reines, F. B. Harrison, H. W. Kruse, and A. D. McGuire. "Detection of the Free Neutrino: A Confirmation". In: *Science* 124 (July 1956), pp. 103–104.
- [5] Nobel Foundation. *Nobel Prize in Physics*. 1995.
- [6] G. Danby, J-M. Gaillard, K. Goulian, et al. "Observation of High-Energy Neutrino Reactions and the Existence of Two Kinds of Neutrinos". In: *Phys. Rev. Lett.* 9 (1 1962), pp. 36–44.
- [7] DONUT Collaboration, K. Kodama, N. Ushida, et al. "Observation of tau neutrino interactions". In: *Physics Letters B* 504 (Apr. 2001), pp. 218–224. eprint: [hep-ex/0012035](#).
- [8] K. Kodama, N. Ushida, C. Andreopoulos, et al. "Final tau-neutrino results from the DONuT experiment". In: *Phys. Rev. D* 78.5, 052002 (Sept. 2008), p. 052002. arXiv: [0711.0728 \[hep-ex\]](#).
- [9] The ALEPH Collaboration, the DELPHI Collaboration, the L3 Collaboration, et al. "Precision Electroweak Measurements on the Z Resonance". In: *ArXiv High Energy Physics - Experiment e-prints* (Sept. 2005). eprint: [hep-ex/0509008](#).
- [10] A. De Angelis. "Domenico Pacini, uncredited pioneer of the discovery of cosmic rays". In: *ArXiv e-prints* (Mar. 2011). arXiv: [1103.4392](#).
- [11] J. R. Hoerandel. "Early cosmic-ray work published in German". In: *American Institute of Physics Conference Series*. Ed. by J. F. Ormes. Vol. 1516. American Institute of Physics Conference Series. Feb. 2013, pp. 52–60. arXiv: [1212.0706](#).
- [12] Arthur H. Compton. "A Geographic Study of Cosmic Rays". In: *Phys. Rev.* 43 (6 1933), pp. 387–403.
- [13] Nobel Foundation. *Nobel Prize in Physics*. 1936.
- [14] M Blau and H Wambacher. "Disintegration Processes by Cosmic Rays with the Simultaneous Emission of Several Heavy Particles". In: 140 (Jan. 1937), pp. 585–585.
- [15] W. Bothe and W. Kolhoerster. "Das Wesen der Hoehenstrahlung". In: *Zeitschrift fur Physik* 56 (Nov. 1929), pp. 751–777.

- [16] G. W. Clark, J. Earl, W. L. Kraushaar, et al. “Cosmic-Ray Air Showers at Sea Level”. In: *Phys. Rev.* 122 (2 1961), pp. 637–654.
- [17] K. A. Olive et al. “Review of Particle Physics”. In: *Chin. Phys.* C38 (2014), p. 090001.
- [18] M. Honda, M. S. Athar, T. Kajita, K. Kasahara, and S. Midorikawa. “Atmospheric neutrino flux calculation using the NRLMSISE-00 atmospheric model”. In: *Phys. Rev. D* 92.2, 023004 (July 2015), p. 023004. arXiv: 1502.03916 [astro-ph.HE].
- [19] Wikimedia Commons. *File:Standard Model of Elementary Particles.svg* — *Wikimedia Commons, the free media repository*. [Online; accessed 23-February-2018]. 2017.
- [20] J. A. Formaggio and G. P. Zeller. “From eV to EeV: Neutrino cross sections across energy scales”. In: *Reviews of Modern Physics* 84 (July 2012), pp. 1307–1341. arXiv: 1305.7513 [hep-ex].
- [21] D. Chirkin and W. Rhode. “Propagating leptons through matter with Muon Monte Carlo (MMC)”. In: *ArXiv High Energy Physics - Phenomenology e-prints* (July 2004). eprint: hep-ph/0407075.
- [22] H. Pessard. “The Opera Experiment”. In: *High Energy Physics, ICHEP 2004*. Ed. by H. Chen, D. Du, W. Li, and C. Lu. Apr. 2005, pp. 299–303. eprint: hep-ex/0504033.
- [23] Minos Collaboration, D. G. Michael, P. Adamson, et al. “The magnetized steel and scintillator calorimeters of the MINOS experiment”. In: *Nuclear Instruments and Methods in Physics Research A* 596 (Nov. 2008), pp. 190–228. arXiv: 0805.3170 [physics.ins-det].
- [24] S. Mufson, B. Baugh, C. Bower, et al. “Liquid scintillator production for the NOvA experiment”. In: *Nuclear Instruments and Methods in Physics Research A* 799 (Nov. 2015), pp. 1–9. arXiv: 1504.04035 [physics.ins-det].
- [25] L. Aliaga and et al. “Design, calibration, and performance of the MINERvA detector”. In: *Nuclear Instruments and Methods in Physics Research A* 743 (Apr. 2014), pp. 130–159. arXiv: 1305.5199 [physics.ins-det].
- [26] Y. Kudenko and T2K Collaboration. “The near neutrino detector for the T2K experiment”. In: *Nuclear Instruments and Methods in Physics Research A* 598 (Jan. 2009), pp. 289–295. arXiv: 0805.0411 [physics.ins-det].
- [27] M. Antonello, B. Baibussinov, V. Bellini, et al. “ICARUS at FNAL”. In: *ArXiv e-prints* (Dec. 2013). arXiv: 1312.7252 [physics.ins-det].
- [28] P. A. Čerenkov. “Visible Radiation Produced by Electrons Moving in a Medium with Velocities Exceeding that of Light”. In: *Physical Review* 52 (Aug. 1937), pp. 378–379.
- [29] P. A. Cherenkov. “Visible luminescence of pure liquids under the influence of - radiation”. In: *Dokl. Akad. Nauk SSSR* 2.8 (1934). [Usp. Fiz. Nauk93,no.2,385(1967)], pp. 451–454.
- [30] I. M. Frank and I. E. Tamm. “Coherent visible radiation of fast electrons passing through matter”. In: *Compt. Rend. Acad. Sci. URSS* 14.3 (1937). [Usp. Fiz. Nauk93,no.2,388(1967)], pp. 109–114.
- [31] D.J. Griffiths. *Introduction to Electrodynamics*. Ed. by Pearson Education Limited. Fourth. 2013.
- [32] S. Tavernier. *Experimental Techniques in Nuclear and Particle Physics*. Ed. by Springer-Verlag. 2010.

- [33] K.A. Olive and Particle Data Group. “Review of Particle Physics”. In: *Chinese Physics C* 38.9 (2014), p. 090001.
- [34] B. Aharmim, S. N. Ahmed, A. E. Anthony, et al. “Combined analysis of all three phases of solar neutrino data from the Sudbury Neutrino Observatory”. In: *Phys. Rev. C* 88.2, 025501 (Aug. 2013), p. 025501. arXiv: 1109.0763 [nucl-ex].
- [35] C. W. Walter. “The Super-Kamiokande Experiment”. In: *Neutrino Oscillations: Present Status and Future Plans*. Ed. by J. A. Thomas and P. L. Vahle. World Scientific Publishing Co, 2008, pp. 19–43.
- [36] F. Montanet. “Design and expected performance of the ANTARES neutrino telescope”. In: *Nuclear Physics B Proceedings Supplements* 87 (June 2000), pp. 436–438. eprint: astro-ph/0001380.
- [37] M. G. Aartsen, M. Ackermann, J. Adams, et al. “The IceCube Neutrino Observatory: instrumentation and online systems”. In: *Journal of Instrumentation* 12 (Mar. 2017), P03012. arXiv: 1612.05093 [astro-ph.IM].
- [38] B. Pontecorvo. “Neutrino Experiments and the Problem of Conservation of Leptonic Charge”. In: *Sov. Phys. JETP* 26 (1968). [Zh. Eksp. Teor. Fiz. 53, 1717(1967)], pp. 984–988.
- [39] Z. Maki, M. Nakagawa, and S. Sakata. “Remarks on the Unified Model of Elementary Particles”. In: *Progress of Theoretical Physics* 28 (Nov. 1962), pp. 870–880.
- [40] C. Giganti, S. Lavignac, and M. Zito. “Neutrino oscillations: The rise of the PMNS paradigm”. In: *Progress in Particle and Nuclear Physics* 98 (Jan. 2018), pp. 1–54. arXiv: 1710.00715 [hep-ex].
- [41] S. T. Petcov. “The Nature of Massive Neutrinos”. In: *Adv. High Energy Phys.* 2013 (2013), p. 852987. arXiv: 1303.5819 [hep-ph].
- [42] E. K. Akhmedov and A. Y. Smirnov. “Paradoxes of neutrino oscillations”. In: *Physics of Atomic Nuclei* 72 (Aug. 2009), pp. 1363–1381. arXiv: 0905.1903 [hep-ph].
- [43] A. Y. Smirnov. “The MSW Effect and Matter Effects in Neutrino Oscillations”. In: *Physica Scripta Volume T* 121 (Jan. 2005), pp. 57–64. eprint: hep-ph/0412391.
- [44] S. M. Bilenky. “Neutrino oscillations: brief history and present status”. In: *ArXiv e-prints* (Aug. 2014). arXiv: 1408.2864 [hep-ph].
- [45] V. Barger, K. Whisnant, S. Pakvasa, and R. J. N. Phillips. “Matter effects on three-neutrino oscillations”. In: *Phys. Rev. D* 22 (11 1980), pp. 2718–2726.
- [46] Super-Kamiokande Collaboration. *Prob3++*. 2012.
- [47] Adam M. Dziewonski and Don L. Anderson. “Preliminary reference Earth model”. In: *Physics of the Earth and Planetary Interiors* 25.4 (1981), pp. 297 –356.
- [48] John N. Bahcall. “Solar Neutrinos. I. Theoretical”. In: *Phys. Rev. Lett.* 12 (11 1964), pp. 300–302.
- [49] Raymond Davis. “Solar Neutrinos. II. Experimental”. In: *Phys. Rev. Lett.* 12 (11 1964), pp. 303–305.
- [50] Bruce T. Cleveland, Timothy Daily, Jr. Raymond Davis, et al. “Measurement of the Solar Electron Neutrino Flux with the Homestake Chlorine Detector”. In: *The Astrophysical Journal* 496.1 (1998), p. 505.

- [51] J. N. Abdurashitov, V. N. Gavrin, V. V. Gorbachev, et al. “Measurement of the solar neutrino capture rate with gallium metal. III. Results for the 2002-2007 data-taking period”. In: *Phys. Rev. C* 80.1, 015807 (July 2009), p. 015807. arXiv: 0901.2200 [[nucl-ex](#)].
- [52] W. Hampel, J. Handt, G. Heusser, et al. “GALLEX solar neutrino observations: results for GALLEX IV”. In: *Physics Letters B* 447.1 (1999), pp. 127 –133.
- [53] M. Altmann, M. Balata, P. Belli, et al. “Complete results for five years of GNO solar neutrino observations”. In: *Physics Letters B* 616.3 (2005), pp. 174 –190.
- [54] Herbert H. Chen. “Direct Approach to Resolve the Solar-Neutrino Problem”. In: *Phys. Rev. Lett.* 55 (14 1985), pp. 1534–1536.
- [55] Nobel Foundation. *Nobel Prize in Physics*. 2015.
- [56] Y. Fukuda, T. Hayakawa, E. Ichihara, et al. “Evidence for Oscillation of Atmospheric Neutrinos”. In: *Phys. Rev. Lett.* 81 (8 1998), pp. 1562–1567.
- [57] J. Bergström, M. C. Gonzalez-Garcia, M. Maltoni, and T. Schwetz. “Bayesian global analysis of neutrino oscillation data”. In: *Journal of High Energy Physics* 9, 200 (Sept. 2015), p. 200. arXiv: 1507.04366 [[hep-ph](#)].
- [58] I. Esteban, M. C. Gonzalez-Garcia, M. Maltoni, I. Martinez-Soler, and T. Schwetz.
- [59] S. Gariazzo, C. Giunti, M. Laveder, Y. F. Li, and E. M. Zavanin. “Light sterile neutrinos”. In: *Journal of Physics G Nuclear Physics* 43.3, 033001 (Mar. 2015), p. 033001. arXiv: 1507.08204 [[hep-ph](#)].
- [60] J. M. Conrad, C. M. Ignarra, G. Karagiorgi, M. H. Shaevitz, and J. Spitz. “Sterile Neutrino Fits to Short Baseline Neutrino Oscillation Measurements”. In: *ArXiv e-prints* (July 2012). arXiv: 1207.4765 [[hep-ex](#)].
- [61] S. Gariazzo, C. Giunti, M. Laveder, and Y. F. Li. “Updated global 3+1 analysis of short-baseline neutrino oscillations”. In: *Journal of High Energy Physics* 6, 135 (June 2017), p. 135. arXiv: 1703.00860 [[hep-ph](#)].
- [62] P. Adamson, D. J. Auty, D. S. Ayres, et al. “Active to Sterile Neutrino Mixing Limits from Neutral-Current Interactions in MINOS”. In: *Physical Review Letters* 107.1, 011802 (July 2011), p. 011802. arXiv: 1104.3922 [[hep-ex](#)].
- [63] P. Adamson, I. Anghel, A. Aurisano, et al. “Search for Sterile Neutrinos Mixing with Muon Neutrinos in MINOS”. In: *Physical Review Letters* 117.15, 151803 (Oct. 2016), p. 151803. arXiv: 1607.01176 [[hep-ex](#)].
- [64] P. Adamson, L. Aliaga, D. Ambrose, et al. “Search for active-sterile neutrino mixing using neutral-current interactions in NOvA”. In: *Phys. Rev. D* 96.7, 072006 (Oct. 2017), p. 072006. arXiv: 1706.04592 [[hep-ex](#)].
- [65] K. Abe, Y. Haga, Y. Hayato, et al. “Limits on sterile neutrino mixing using atmospheric neutrinos in Super-Kamiokande”. In: *Phys. Rev. D* 91 (5 2015), p. 052019.
- [66] IceCube Collaboration, M. G. Aartsen, M. Ackermann, et al. “Search for sterile neutrino mixing using three years of IceCube DeepCore data”. In: *ArXiv e-prints* (Feb. 2017). arXiv: 1702.05160 [[hep-ex](#)].
- [67] M. G. Aartsen, K. Abraham, M. Ackermann, et al. “Searches for Sterile Neutrinos with the IceCube Detector”. In: *Physical Review Letters* 117.7, 071801 (Aug. 2016), p. 071801. arXiv: 1605.01990 [[hep-ex](#)].

- [68] Stephen Parke and Mark Ross-Lonergan. “Unitarity and the three flavor neutrino mixing matrix”. In: *Phys. Rev. D* 93 (11 2016), p. 113009.
- [69] M. G. Aartsen, M. Ackermann, J. Adams, et al. “Calibration and characterization of the IceCube photomultiplier tube”. In: *Nuclear Instruments and Methods in Physics Research Section A: Accelerators, Spectrometers, Detectors and Associated Equipment* 618.1 (2010), pp. 139 –152.
- [70] Hammamatsu Photonics. *PHOTOMULTIPLIER TUBE DATA SHEET R7081-02 for ICECUBE Experiment*. 2003.
- [71] R. Abbasi, Y. Abdou, T. Abu-Zayyad, et al. “The design and performance of IceCube DeepCore”. In: *Astroparticle Physics* 35 (May 2012), pp. 615–624. arXiv: 1109.6096 [astro-ph.IM].
- [72] M. G. Aartsen, R. Abbasi, Y. Abdou, et al. “Measurement of South Pole ice transparency with the IceCube LED calibration system”. In: *Nuclear Instruments and Methods in Physics Research A* 711 (May 2013), pp. 73–89. arXiv: 1301.5361 [astro-ph.IM].
- [73] The HAWC Collaboration and The IceCube Collaboration. “Combined Analysis of Cosmic-Ray Anisotropy with IceCube and HAWC”. In: *ArXiv e-prints* (Aug. 2017). arXiv: 1708.03005 [astro-ph.HE].
- [74] M. G. Aartsen, G. C. Hill, A. Kyriacou, et al. “Measurement of the multi-TeV neutrino interaction cross-section with IceCube using Earth absorption”. In: *Nature* 551 (Nov. 2017), pp. 596–600. arXiv: 1711.08119 [hep-ex].
- [75] M. G. Aartsen, K. Abraham, M. Ackermann, et al. “Observation and Characterization of a Cosmic Muon Neutrino Flux from the Northern Hemisphere Using Six Years of IceCube Data”. In: *Ap.J.* 833, 3 (Dec. 2016), p. 3. arXiv: 1607.08006 [astro-ph.HE].
- [76] IceCube Collaboration. “Evidence for High-Energy Extraterrestrial Neutrinos at the IceCube Detector”. In: *Science* 342, 1242856 (Nov. 2013), p. 1242856. arXiv: 1311.5238 [astro-ph.HE].
- [77] S. Euler. “Observations of Oscillations of Atmospheric Neutrinos with the IceCube Neutrino Observatory”. Ph.D. Rheinisch-Westfälische Technische Hochschule (RWTH), 2013.
- [78] M. G. Aartsen, R. Abbasi, Y. Abdou, et al. “Measurement of Atmospheric Neutrino Oscillations with IceCube”. In: *Physical Review Letters* 111.8, 081801 (Aug. 2013), p. 081801. arXiv: 1305.3909 [hep-ex].
- [79] IceCube Collaboration, M. G. Aartsen, M. Ackermann, et al. “Determining neutrino oscillation parameters from atmospheric muon neutrino disappearance with three years of IceCube DeepCore data”. In: *ArXiv e-prints* (Oct. 2014). arXiv: 1410.7227 [hep-ex].
- [80] IceCube Collaboration, M. G. Aartsen, M. Ackermann, et al. “Measurement of Atmospheric Neutrino Oscillations at 6-56 GeV with IceCube DeepCore”. In: *ArXiv e-prints* (July 2017). arXiv: 1707.07081 [hep-ex].
- [81] M. G. Aartsen, M. Ackermann, J. Adams, et al. “Search for annihilating dark matter in the Sun with 3 years of IceCube data”. In: *European Physical Journal C* 77, 146 (Mar. 2017), p. 146. arXiv: 1612.05949 [astro-ph.HE].

- [82] M. G. Aartsen, K. Abraham, M. Ackermann, et al. “All-flavour search for neutrinos from dark matter annihilations in the Milky Way with IceCube/DeepCore”. In: *European Physical Journal C* 76, 531 (Oct. 2016), p. 531. arXiv: 1606.00209 [astro-ph.HE].
- [83] N. E. Bramall, R. C. Bay, K. Woschnagg, R. A. Rohde, and P. B. Price. “A deep high-resolution optical log of dust, ash, and stratigraphy in South Pole glacial ice”. In: *Geophys. Res. Lett.* 32, L21815 (Nov. 2005), p. L21815.
- [84] M. Ackermann, J. Ahrens, X. Bai, et al. “Optical properties of deep glacial ice at the South Pole”. In: *Journal of Geophysical Research (Atmospheres)* 111, D13203 (July 2006), p. D13203.
- [85] IceCube Collaboration. *IceCube Dust Map*. 2011. URL: <http://icecube.berkeley.edu/~bay/dustmap/>.
- [86] IceCube Collaboration, M. G. Aartsen, R. Abbasi, et al. “The IceCube Neutrino Observatory Part VI: Ice Properties, Reconstruction and Future Developments”. In: *ArXiv e-prints* (Sept. 2013). arXiv: 1309.7010 [astro-ph.HE].
- [87] M. Rongen. “Measuring the optical properties of IceCube drill holes”. In: *European Physical Journal Web of Conferences*. Vol. 116. European Physical Journal Web of Conferences. Apr. 2016, p. 06011.
- [88] Eric Jones, Travis Oliphant, Pearu Peterson, et al. *SciPy: Open source scientific tools for Python*. [Online; accessed <today>]. 2001–.
- [89] S. S. Wilks. “The Large-Sample Distribution of the Likelihood Ratio for Testing Composite Hypotheses”. In: *Ann. Math. Statist.* 9.1 (Mar. 1938), pp. 60–62.
- [90] G. J. Feldman and R. D. Cousins. “Unified approach to the classical statistical analysis of small signals”. In: *Phys. Rev. D* 57 (Apr. 1998), pp. 3873–3889. eprint: [physics/9711021](https://arxiv.org/abs/physics/9711021).

## Notes